# Organization principles of thalamocortical input onto deep-layer inhibitory neurons of the barrel cortex

Doctoral thesis

to obtain a doctorate (PhD)

from the Faculty of Medicine

of the University of Bonn

**Luis Fernando Messore**

from Buenos Aires, Argentina

2024

Written with authorization of

the Faculty of Medicine of the University of Bonn

First reviewer: Prof. Dr. Marcel Oberlaender

Second reviewer: Prof. Dr. Heinz Beck

Day of oral examination: 23.02.2024

From the Max Planck Institute for Neurobiology of Behavior

Director: Prof. Dr. Jason Kerr

# Contents

## List of abbreviations

| | |
|---|---|
| (-/-) | Double negative |
| 5-HT3 | Serotonin receptor |
| AAV | Adeno-Associated Virus |
| AP | Action potential |
| BC | Barrel Cortex |
| CTB | Cholera Toxin subunit B |
| EF-1α | Elongation Factor 1 Alpha |
| EGFP | E-coli derivated Green-Fluorescent protein |
| EPSP | Excitatory postsynaptic potential |
| Exc. | Excitatory neurons |
| GABA | Gamma-Aminobutyric acid |
| GAD | Glutamate Decarboxylase |
| GFP | Green Fluorescent protein |
| INs | Inhibitory neurons |
| IPSP | Inhibitory postsynaptic potential |
| KS-Test | Kolmogorov–Smirnov test |
| L1 | Layer 1 |
| L2/3 | Layer 2/3 |
| L4Ins | Layer 4 Inhibitory neurons |
| L4SS | Layer 4 Spiny-Stellate neurons |
| L4 | Layer 4 |
| L5Ins | Layer 5 Inhibitory neurons |
| L5PTs | Layer 5 Pyramidal tract neurons |
| L5ST | Layer 5 Slender tufted neurons |
| L5 | Layer 5 |
| L6CC | Layer 6 Corticocortical neurons |
| L6 | Layer 6 |
| LFP | Local field potential |
| M1 | Primary motor cortex |

| | |
|---|---|
| NaCl | Sodium Chloride |
| NeuN | Hexaribonucleotide Binding Protein-3 |
| NGS | Normal Goat Serum |
| NRR | Normal Rat Ringer solution |
| PB | Phosphate Buffer |
| PFA | Paraformaldehyde |
| POm | Thalamic Posteromedial nucleus |
| PV | Parvalbumin |
| PW | Principal Whisker |
| rAAV | Recombinant Adeno-Associated Virus |
| RFP | Red Fluorescent protein |
| ROI | Region of Interest |
| S1 | Primary somatosensory cortex |
| S2 | Secondary somatosensory cortex |
| SST | Somatostatin |
| SW | Surrounding whisker |
| TC | Thalamocortical |
| TX | Triton-X |
| VIP | Vasoactive Intestinal peptide |
| VPm | Thalamic Ventral Posteromedial nucleus |
| VS1 | Barrel cortex |
| WM | White Matter |

# 1. Introduction

## 1.1 Thalamocortical pathway for sensory information

Thalamus functions as the main route by which incoming sensory information reaches the cerebral cortex. Thalamic nuclei will receive input from the sensory receptors in the periphery and relay it to different areas in the cortex. As an example, visual input will flow from the receptors in the retina, to the lateral geniculate nucleus (LGN), and finally to the visual cortex (V1). This organization of sensory pathways, from the periphery to the cortex, can also be seen for the auditory, tactile, and other sources of sensory information (Boivie & Perl, 1975; Mountcastle, 1980; Brodal, 1981; Heimer, 1983).

A characteristic of these sensory systems is that axons from primary thalamic nuclei congregate more densely in layer 4, which is therefore considered the primary input layer of the cortex. Once there, sensory signals will propagate from layer 4 to layer 2/3 and then to layer 5 creating the canonical pathway for sensory information (Douglas et al., 2004; Gilbert et al., 1979) (figure 1). This pathway has been observed not only across sensory modalities but also across species, being a general organization of sensory information (Okamoto et al., 2001).

In this thesis, I will use the vibrissal system of the rat as a model of thalamocortical input to the cortex in sensory processing (figure 2). Each whisker deflection activates the sensory receptors in the hair follicle. These are in turn innervated by a peripheral axon from the trigeminal nerve. The information will flow from the trigeminal nerves through relay stations in the brainstem to project to different nuclei in the thalamus (Deschênes et al, 2005). Finally, the cortex will receive most of the thalamocortical (TC) projections from two thalamic nuclei, the ventral posteromedial nucleus (VPm) and the posteromedial complex (POm) (Landisman et al, 2007).

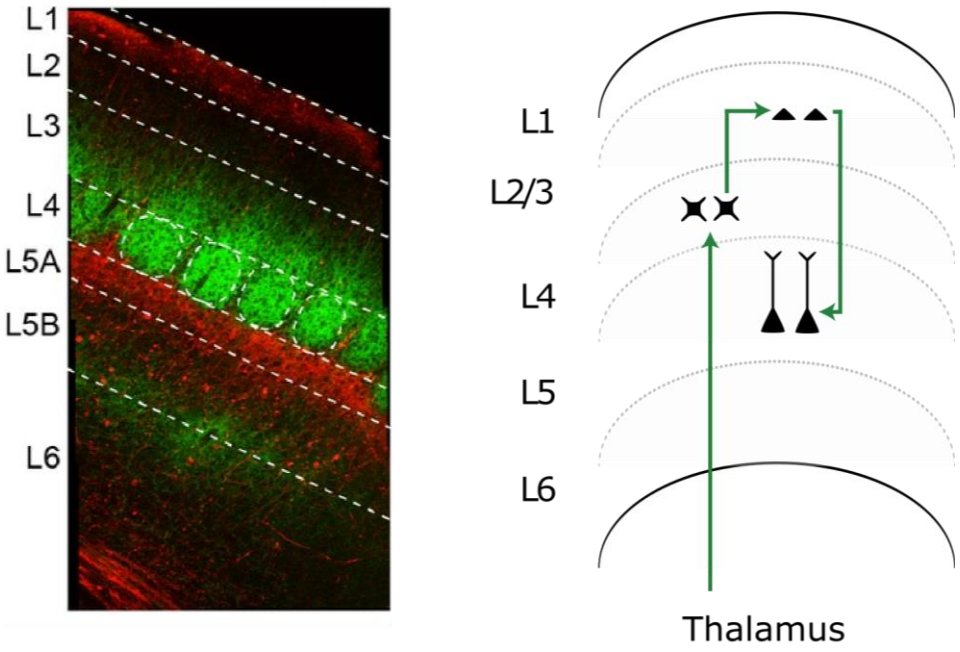


Fig .1 Canonical pathway for sensory information

Double injection of anterograde tracers in the VPm and POm nuclei of the thalamus which project to different layers in the barrel cortex. Thalamic axons from POm (red) were mostly found in the upper part of L5 and L1 of the barrel cortex. Axons from VPm (green) are prominent in L4, with the characteristic barrel shaped expression. Figure adapted from Sermet et al., 2019. Right panel shows the canonical pathway of sensory information. Sensory input will travel from the thalamus to layer 4, then layer 2/3, and finally layer 5, where axons project to postsynaptic targets outside the cortex.

These nuclei will carry distinct information to this cortex, where the VPm will carry information originating from individual whisker follicles and ascend to terminate primarily in the somatotopically aligned column in the barrel cortex (vS1) (Diamond et al., 2008; Fox, 2008). Meanwhile, the POm receives more diffuse sensory projections from the brainstem instead of single whisker information. POm neurons will send their projections into the secondary somatosensory cortex (S2), the primary motor cortex (M1), and layers 1 and 5 of the barrel cortex (figure 1).


Fig. 2: Rat vibrissal system

(A) Schematic representation of a signal evoked by the deflection of a facial whisker which travels through the axons of the trigeminal ganglion (1) to relay in the nuclei of the brainstem (2) and then to the thalamic nuclei (3) where the information is finally sent to the barrel cortex. (B) Somatotopic arrangement of the vibrissal system at the whisker pad in the rat's snout, and in the layer 4 barrels in the somatosensory cortex. The barrels and whiskers are arranged into rows (A to E) and in arcs (1 - 7), the specific number depending on the row. The highlighted whisker-barrel pair corresponds to C2. Figure adapted from Petersen et al., 2019.

All cortical layers of the barrel cortex receive thalamic input from either the VPM or POm neurons (Feldmeyer, 2012). As mentioned above, the highest density of thalamocortical axons can be found in layer 4, thus regarded as the major input layer of the barrel cortex (Bernardo & Woolsey, 1987; Jensen et al., 1987; Chmielowska et al., 1989; Senft & Woolsey, 1991; Pierret et al., 2000; Wimmer et al., 2010; Oberlaender et al., 2011b). Here, a cell-type specific distribution of thalamocortical input has been described for different areas of the cortex (Nishiyama et al., 2019; Sermet et al., 2019).

In layer 4, both excitatory and inhibitory neurons are extensively innervated by the thalamus (figure 3). It has been reported that although there are clear layer-specific differences in synaptic inputs, within each layer there were typically some excitatory neurons that received much larger than average thalamic input (Sermet et al., 2019).

Similarly, inhibitory neurons also showed cell-type specific thalamic innervation. In this case, this translates to a sharp, early evoked response to thalamic input which precedes even the surrounding excitatory population (Beierlein et al., 2003; Audette et al., 2018; Willems et al., 2019).

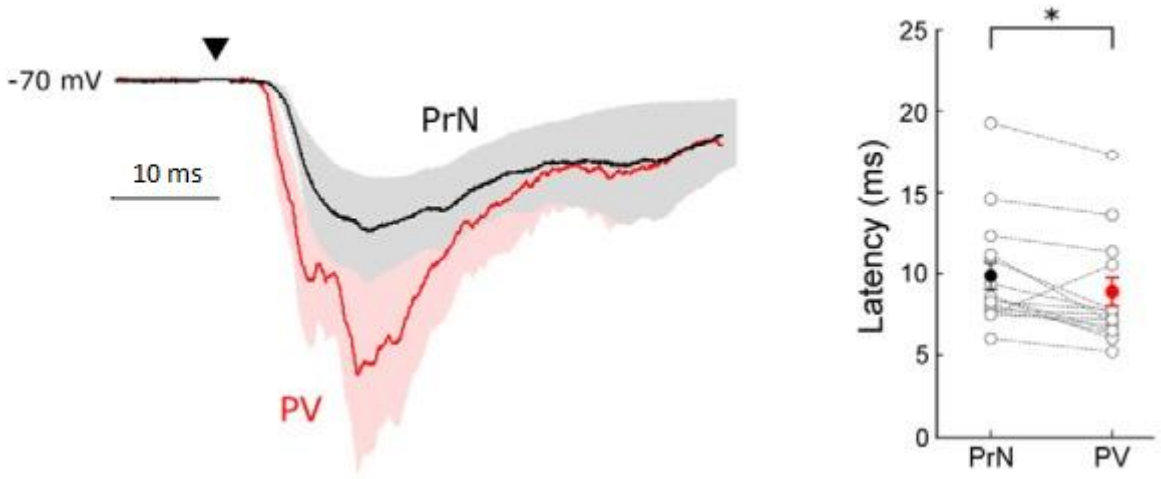


Fig. 3: Excitatory and inhibitory activation in layer 4.

Example of excitatory (black) and inhibitory (red) neuron responses after the application of a postsynaptic 200 pA current. Latency of response shows that the inhibitory neurons respond earlier to the same stimulus. Figure adapted from Willems et al., 2019.

## 1.2 Thalamocortical circuits in the deep layers

Although the canonical pathway is able to explain the activation of layer 4 neurons after the thalamic activation, it has become increasingly clear that neuronal responses from layer 5 do not fit with the signal flow of the canonical pathway. It has been shown that responses from layer 5 pyramidal tract neurons (L5PTs), respond with a latency similar to those excitatory neurons in layer 4 (De Kock et al., 2007; Egger et al., 2020).

Given their fast onset, it seems that these neurons do not rely exclusively on the canonical pathway. Moreover, the inactivation of layer 4 does not abolish the response of these neurons and it was hence suggested that L5PTs are driven directly by thalamus (Constantinople et al., 2013).

However, recent evidence has shown that this is not the case. Instead, L5PTs are indirectly driven by thalamocortical input, through the activation of layer 6 corticocortical neurons (L6CC) (Egger et al., 2020). These neurons cluster around the second innervation peak of primary thalamocortical input coming from the VPm at the layer 5/6 border.

The population of L6CC neurons exhibits a fast and reliable response to the stimulus presentation. Moreover, their response precedes all other excitatory subtypes in the barrel cortex (Egger et al., 2020). Although the deep layers are less densely innervated than the primary peak in layer 4, the thalamocortical input converges similarly strong to excitatory neurons in layer 4 (L4SPs) and in layer 6 (L6CC) (Constantinople et al., 2013). In fact, this activation follows a bistratified system, where the same VPm axons targeting layer 4, will drive the L6CC population (Bruno et al., 2006; Frangeul et al., 2014; Egger et al., 2020).

Nevertheless, contrary to neurons in layer 4, L6CC neurons do not project vertically to the upper layers, but in turn do it horizontally within layer 5 and were shown to be necessary to drive fast sensory-evoked responses in this layer (Oberlaender et al., 2012; Narayanan et al., 2015; Narayanan et al., 2017) (figure 4). The new evidence provided by these studies, brings a new understanding of the thalamocortical circuits in the barrel cortex, adding other layers of complexity to the canonical pathway described by Gilbert in 1979 (Gilbert & Wiesel, 1979).

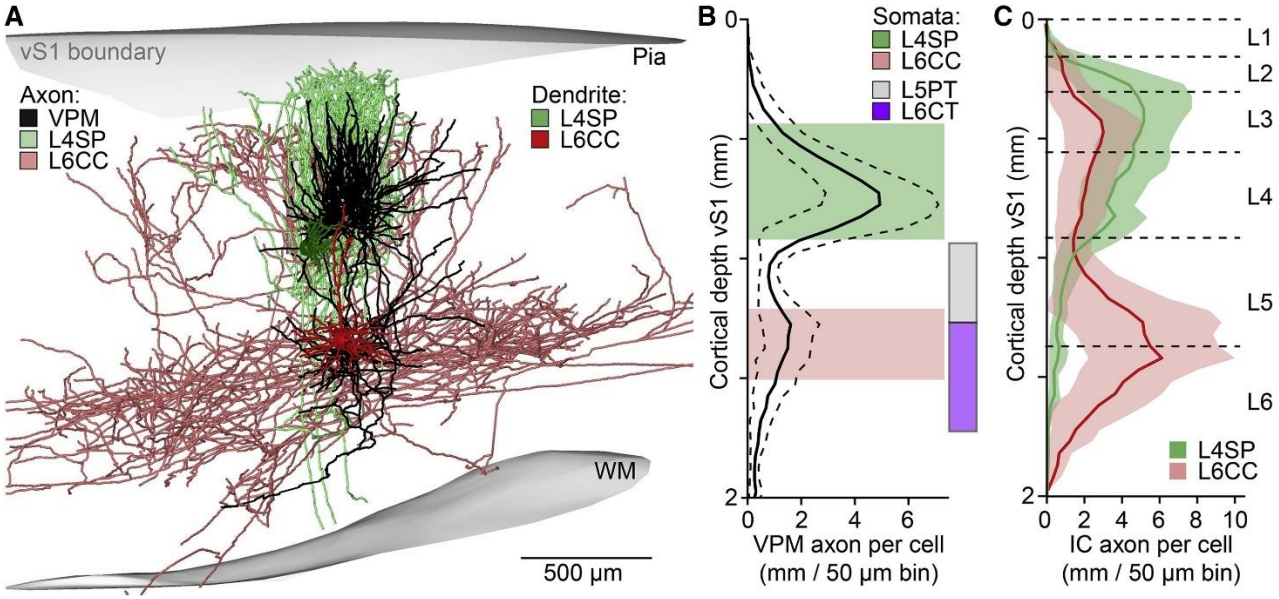


Fig. 4: Thalamocortical input and axo-dendritic projections of L6CC

(A) Example of the axo-dendritic arborization of L4SP (green) and L6CC neuron (red) in the barrel cortex. In black the reconstruction of VPm axon. (B) Depth distribution of the VPm axon showing the two innervation peaks in layers 4 and 5/6 border. (C) Intracortical axon length across depth and between L4SP (green) and L6CC (red). Intracortical axon projections from L6CC neurons cluster in the L5/6 border. Figure obtained from Egger et al., 2020.

Thalamocortical projections will target directly both excitatory and inhibitory neurons. I have shown this in the previous section for both neuron types in layer 4. Considering the new evidence for direct thalamic activation of excitatory neurons in the deep layers, an investigation of the role of direct thalamocortical input onto the inhibitory population on the deep layers is required, as also is the evaluation of the role of the deep layer inhibitory neurons in modulating the responses of L5PTs.

## 1.3 Inhibitory circuits in the barrel cortex

Similar to what was reported for the excitatory neurons, the connectivity, response to the thalamocortical activation, and response patterns of inhibitory neurons differ between those in layer 4 and those in the deeper layers. For example, thalamocortical inputs in layer 4 preferentially synapse onto some inhibitory neurons as compared with others (Beierlein et al., 2003; Xu et al., 2013) (figure 5). Meanwhile, intracortical axons in the deep layers show a preference for targeting inhibitory neurons in general over excitatory ones (McGuire et al., 1984; Bortone et al., 2014).

Feedforward inhibition (FF), mediated by the direct thalamocortical input onto the inhibitory neurons, also shows differences between layer 4 and layers 5 and 6. The best studied FF inhibitory circuit in the cortex is one mediated by the recruitment of parvalbumin (PV) positive neurons by the thalamocortical afferents in layer 4 (Simons & Cavell, 1989; Miller et al., 2001; Tremblay et al., 2016).

This fast spiking PV neurons will target excitatory neurons in layer 4. The temporal difference between the disynaptic feedforward inhibition of L4 neurons lags behind their monosynaptic thalamocortical excitation. This creates a window of 1-2 ms (Pinto et al., 2000; Alonso & Swadlow, 2005) for excitatory neurons to summate afferent inputs for sensory signal transduction (Wehr & Zador, 2003; Gabernet et al., 2005; Wilent & Contreras, 2005).

Other circuit configurations will recruit mostly distinct inhibitory neurons. In the rat's barrel cortex, this inhibitory population can be divided into three non-overlapping families of molecular identities. Roughly all inhibitory neurons fall into one of the molecular identity groups, the parvalbumin positive neurons, somatostatin (SST) positive neurons, and serotoninergic (5-HT3aR) group, out of which the vasointestinal peptide (VIP) positive neurons represent the big majority.

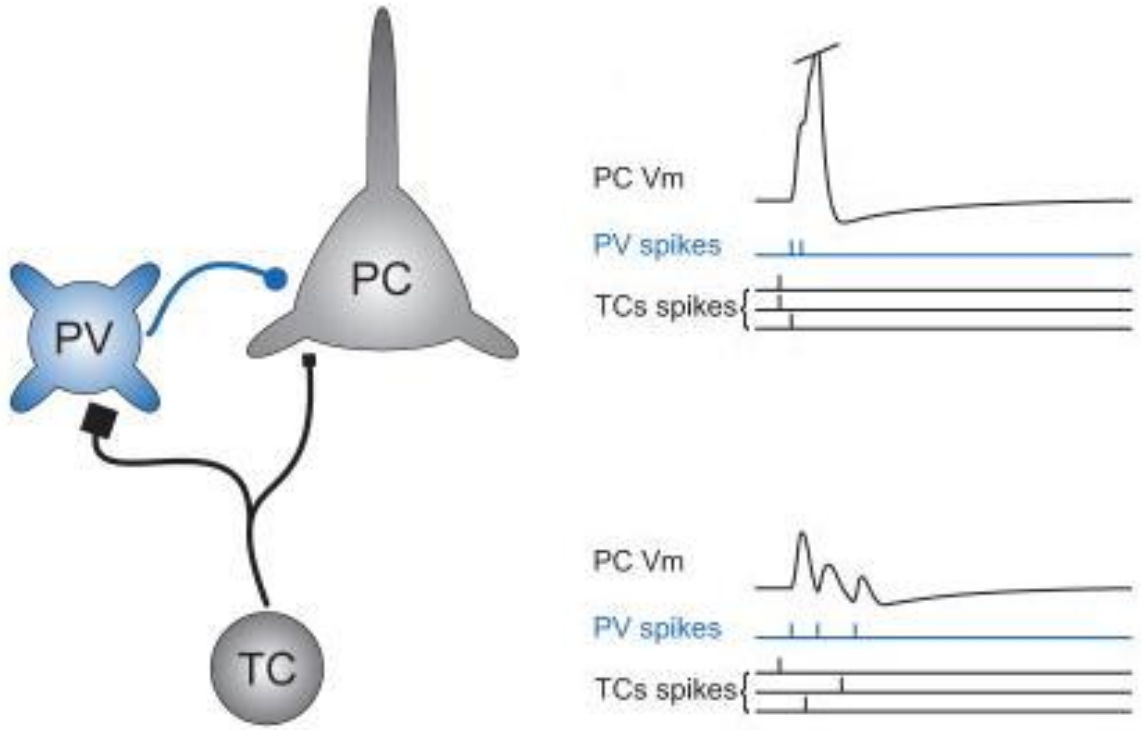


Fig. 5: Feedforward inhibition in layer 4

Schematics of feedforward inhibitory circuits in layer 4. TC represents the thalamocortical input simultaneously activating PV positive inhibitory neurons (blue) and layer 4 excitatory neurons (PC, in gray). The time differences between the direct TC – PC activation and the disynaptic TC – PV – PC creates this window of opportunity for sensory transduction. Right panel shows an example circuit after the synchronous (top) or asynchronous (bottom) TC input. Figure adapted from Tremblay et al. 2016.

In contrast to the FF inhibitory circuits, where the main source of excitation originates from the thalamocortical afferents, in feedback (FB) inhibitory circuits, the source of excitation is locally generated and interneurons synapse back to the local excitatory population (Tremblay et al., 2016). All inhibitory molecular identities seem to be recruited to some capacity in the FB inhibitory circuits in layer 4 (Fino & Yuste, 2011). PV positive neurons that are not involved in FF inhibition are recruited (Buzsaki & Wang, 2012), but in this case, the big majority of inhibitory neurons are part of the somatostatin family (Silberberg, 2008; Adesnik et al., 2012).

In the deep layers of the barrel cortex, the inhibitory circuit motifs, and which populations take part in each configuration seem less clear. The description of L5 PV fast spiking cells fits perfectly with the FF inhibitory circuit, similar to what is described for layer 4 (Hu et al., 2014). However, non-fast spiking PV positive neurons have also been described in layer 5 (Silberberg, 2008), taking part in polysynaptic inhibitory circuits.

A similar heterogeneity of responses can be seen for somatostatin neurons. The majority of this group consists of non-fast spiking Martinotti SST positive neurons, which show responses consistent with indirect thalamocortical activation (Kawaguchi et al., 1997; Ma et al., 2006). Nevertheless, non-Martinotti SST positive neurons show regular or even burst spiking discharge patterns, resembling the fast spiking PV positive neurons (Fanselow et al., 2008; Xu et al., 2013).

Therefore, a systematic assessment of which of these inhibitory neurons in layer 5/6 receive direct thalamocortical input, in which neurons this thalamic activation is sufficient to elicit a response, and what kind of relationship exists between these responses, and the cellular properties of each neuron, would help us understand the organization of FF inhibitory circuits in the deep layers of the barrel cortex.

Here in this thesis, I will provide new evidence on the role of thalamocortical input on the inhibitory population in the deeper layers of the barrel cortex. I systematically investigated how the thalamus targets and activates morphologically identified inhibitory neurons in layers 4 and 5. I address this by examining how these neurons respond both to a direct optogenetic stimulation of the thalamocortical synapses and to a sensory-evoked multi-whisker stimulus. After the recordings are completed, I label the recorded neurons for a post hoc morphological reconstruction and characterize their cellular properties. I also explore the density and number of putative thalamocortical synapses from the VPm onto the dendrites of each of the reconstructed neurons. Finally, I quantify the degree and density of direct thalamocortical input on the inhibitory population by a trans-synaptic viral injection into the VPm nucleus and the barrel cortex. I explore the difference in the number and density of thalamocortical innervated neurons according to their molecular identity and soma depth.

I find that inhibitory neurons in the deep layers exhibit either a reliable fast evoked response that precedes the surrounding excitatory neurons or a delayed response that succeeds the excitatory activation by a time consistent with a monosynaptic jump (Miles & Wong, 1986; Doyle & Andresen, 2001). I report that the composition of these circuit configurations seems to be more heterogeneous than those described for layer 4. In support of that statement, I find that those neurons preceding the excitatory population can have distinct morphologies, molecular identities, response patterns, and cortical depth. The same heterogeneity can be found in those neurons that exhibit a delayed response to the stimulus presentation. I conclude that in the deep layers of the barrel cortex, the thalamus recruits a highly heterogeneous population for feedforward inhibitory circuits, but also spares an equally heterogeneous population.

# 2. Methods

All experimental procedures were carried out in accordance with the animal welfare guidelines of the Max Planck Society after evaluation by the local German authorities. Young adult (P28–35) male Wistar rats, provided by Charles River Laboratories, were housed in a vivarium with standard day/night cycles and controlled temperature and airflow, in a cage for no more than a week before starting the experimental procedure and no more than 2 animals per cage.

## 2.1 Recording and labeling of inhibitory neurons in vS1

The recorded and labeled neurons were obtained from a total of 76 different rats. 25 rats were used only for multi-whisker stimulation and 51 were injected with the rAAV virus for both multi-whisker stimulation and optogenetic manipulation. The injections were performed by Jason Mike Guest (Max Planck Institute for Neurobiology of Behavior - caesar). In those animals, the recording and labeling of the excitatory population was used for another study (Bast & Guest et al., 2023). The inhibitory population from both injected and non-injected animals was analyzed in this thesis.

### 2.1.1 AAV injection in thalamic nuclei

Animals were injected with buprenorphine (0.1 ml/100g Intraperitoneal) at least 30 minutes prior to surgery, the animals were then anesthetized with Isofluorane-$O_2$ gas. Animals were placed in a stereotaxic frame (Kopf Instruments, model 1900) and the surgical area was sterilized. In order to expose the skull, a midline incision of around 5 cm starting from the base of the neck in the rostral direction was done and the fascia retracted. Both bregma and lambda became visible and were marked with a surgical pen.

The thalamic nuclei to be injected (VPm and POm) have been thoroughly investigated and their coordinates (in mm) have been previously published (Wimmer et al., 2010).

- VPm: 3.25 from the midline, 2.9 posterior from bregma, and 5.05 deep from pia.
- POm: 2.10 lateral from midline, 3.25 posterior to bregma, and 5.2 deep from the pia.

The antero-posterior and latero-lateral coordinates were marked with a surgical pen and a circular craniotomy of 0.5 cm was performed using a dental drill (Osada, model EXL-M40) over the injection sites. Prior to the injection of the tracers, the head of the rat was leveled with a 1 µm precision, as to maintain the pipette perpendicular to the pia surface, using an electronic leveling device (eLeVeLeR; Sigmann Elektronics, Hüffenhardt, Germany) mounted in the Kopf stereotaxic frame.

Glass injection capillaries were made from borosilicate glass (Hilgenberg, 1403574) using a pipette puller (Sutter Instruments, Model P100) with previously established custom settings for the pipettes to have a 1 µm tip and a shaft length of at least 6 mm as described in previous studies (Narayanan et al., 2014).

To control for the stereotaxic coordinates of the aforementioned thalamic nuclei and the injection protocols, a dual injection of cholera toxin subunit B (CTB) conjugated with a fluorophore was performed into the VPm and POm nuclei. A custom-made injection device for the Kopf stereotaxic frame was used to pressure inject 50–200 nL of CTB-488 and CTB-647 (Molecular probes, 1 mg/ml in PBS) in the VPm and POm nuclei respectively (Willis et al., 2001). Animals injected with CTB underwent a 5-7 day incubation period before being transcardially perfused.

In the barrel cortex, the layer-specific distribution shows the concentration of VPm projections in layer 4 and layer 6, with some faint labeling of the other layers with the exception of layer 1 (Wimmer et al., 2010). On the other hand, the classical distribution of the POm inputs falls mainly in layer 1 and layer 5 (Viaene et al., 2011). Both are shown in figure 6.

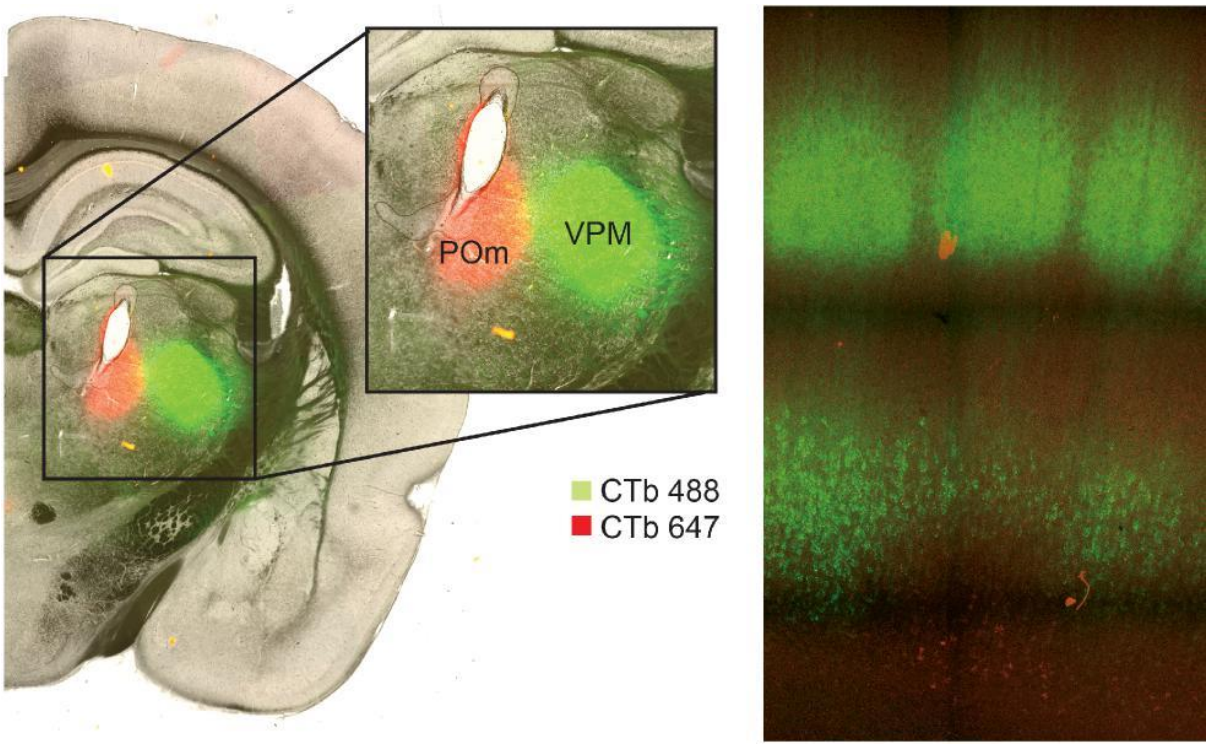


Fig 6: Thalamocortical projections on the barrel cortex

An example image of a double-injected experiment with CTB conjugated with AlexaFluor-488 into the VPm nucleus and AlexaFluor-647 into the POm. The nuclei were identified by using the Paxinos atlas as an anatomical reference (Paxinos & Watson, 2007). On the right panel, the projection distribution of both CTB injections into the barrel cortex, with the characteristic L4 and L6 distribution of the VPm injection can be seen in green.

The same procedure was used to inject 50–200 nL of rAAV-2/1-CAG-hChR2(H134R)-Syn-mCherry (titer $1x10^{12}$ gc/ml) provided by Martin Schwarz (University of Bonn) into the VPm of the left hemisphere (Rothermel et al., 2013). Animals injected with rAAV underwent a 16-21 day incubation period before being re-anesthetized for in vivo electrophysiological recording experiments (figure 7).

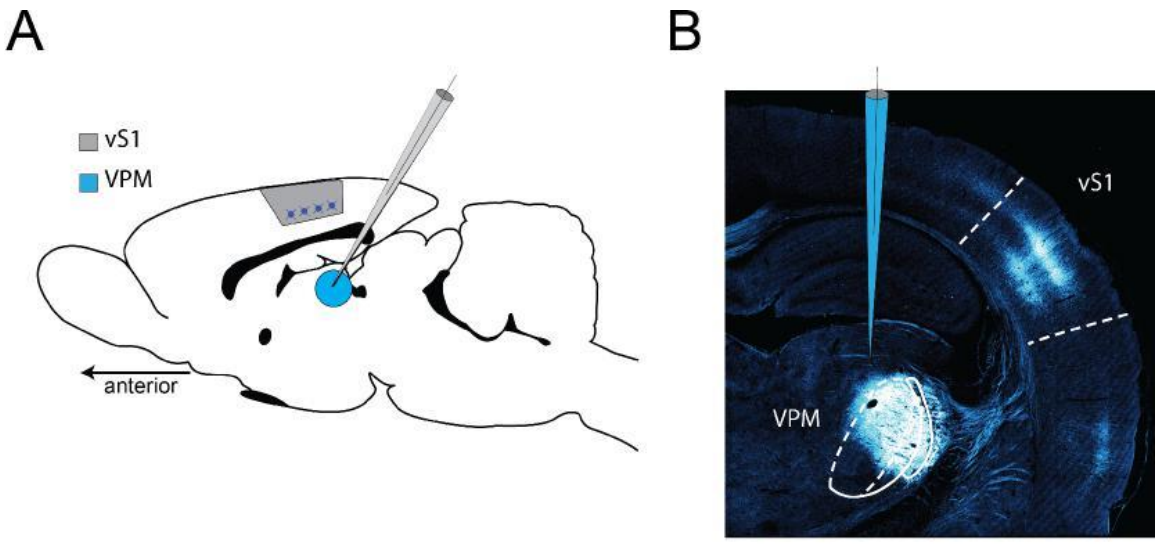


Fig 7: Viral tracer injections in thalamic nuclei

(A) Schematic of a virus injection experiment into VPm. (B) Example image of a VPm-injected animal. High labeling in the injection site with the typical distribution of VPm axon projections in the barrel cortex, with a double band distribution in layers 4 and 6.

### 2.1.2 In vivo cell-attached recordings

In vivo cell-attached recordings were done using a modified version of the juxtacellular recording and labeling technique developed by Pinault (Pinault, 1996), as described in previous works from our group (Narayanan et al., 2014). Animals were anesthetized using a 1.8 g/kg dose of urethane (Sigma Aldrich, 51796) by intraperitoneal injection.

An evaluation of the pinching reflex was used as an assessment of the depth of the anesthesia. The eyelid reflex was checked, and the eyes were protected using a hydration ointment. The temperature was maintained between 36.0 ˚C and 37.0 ˚C. by a heating pad throughout the duration of the experiment.

The skull was exposed, and an area of interest was marked with a surgical pen, 2.1 mm posterior and 5.5 mm lateral respect to the bregma on the left hemisphere. This area corresponds to the area above the barrel cortex where the recordings are going to take place. A craniotomy of 2 mm x 2 mm was done using a dental drill was done.

A crown was created with dental cement around the exposed skull area, making sure that the craniotomy is still exposed and can still be accessed with the glass pipette. This created a bath that was filled with 0.9% NaCl, both to protect the exposed area from the air and to stabilize the recording. The settings of the pipette puller were customized in a way to ensure a pipette tip of 1 µm, which roughly corresponds to a pipette resistance of 3-5 MΩ. The pipettes were loaded with normal rat ringer supplemented with 2% biocytin (Sigma Aldrich, 576-19-2).

The electrode holder is set to a 34° angle to the sagittal plane to target specifically the middle of the barrel cortex (D2 column) (Narayanan et al., 2015). The pipette was slowly advanced until a sudden increase in the resistance, which meant that the pipette contacted the dura mater. That position is set as the zero value, in order to have an assessment of the recording depth. Once inside the brain tissue, the pipette was brought down with 1 µm steps while applying positive current as square pulses (1 nA, 200 ms on/off) to locate single neurons, which were indicated by an increase in electrode resistance.

The pipette was then slowly moved closer to the cell until a positive action potential of circa 2 mV was seen. Waveforms were recorded using an amplifier (npi electronic GmbH, ELC-01X) and digitized using a data acquisition board (CED power1401, Cambridge Electronic Design, Cambridge, UK). Then the pipette was advanced until the resistance was 25-35 MΩ and spikes had an amplitude of 3-8 mV to obtain optimal conditions of juxtasomal filling (figure 8).

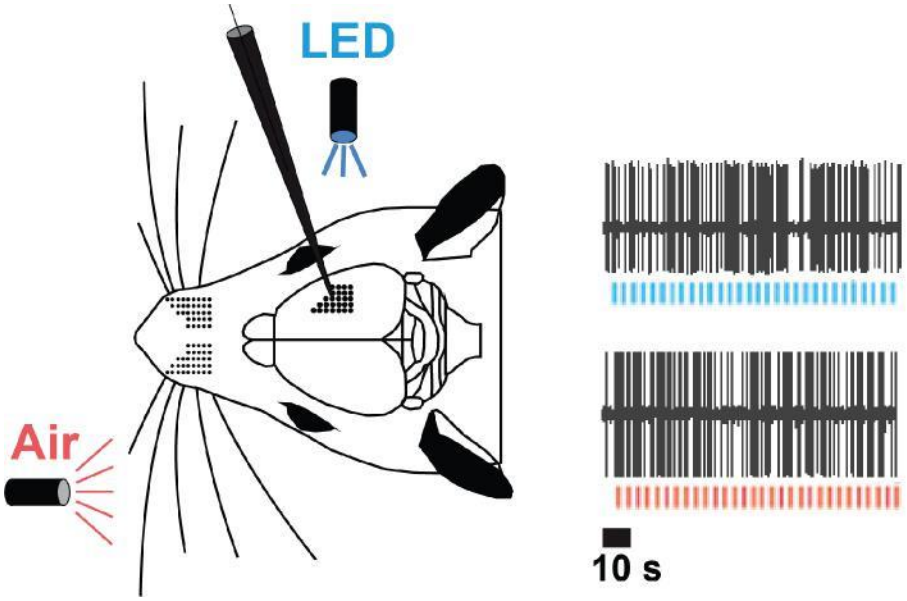


Fig 8: Schematics of the experiment and injections

Schematic of in vivo optogenetic/passive multi-whisker recording experiment. Rats were first injected with rAAV-expressing channelrhodopsin into the VPm to selectively label primary thalamocortical synapses in the barrel cortex. After a 16 – 21 day survival period, rats were re-anesthetized and post-synaptic neuronal responses to an airpuff multi-whisker stimulation and photostimulation of TC synapse were recorded.

For all encountered neurons, both ongoing activity and their sensory-evoked response were recorded. The sensory-evoked stimulus chosen was a multi-whisker deflection, which was repeated 30 times. The stimuli consisted of a 700 ms airpuff repeated at constant intervals of 2500 ms.

The stimuli were delivered by a custom-made plastic tube with a 1 mm opening, placed 8-10 cm from the whisker pad, which deflected all whiskers along the caudal axis. After all recording sessions were done, the biocytin filling was performed. This technique is based on previous works from the group (Narayanan et al., 2014), in this case, a low-intensity square positive current (~10 nA, 200 ms on/off cycle) was applied continuously while gradually increasing the intensity in 0.1 nA steps.

Following the presentation of the multi-whisker stimulus, I optogenetically activated the channelrhodopsin expressing primary thalamus (VPm) synaptic terminals by applying 10 ms light pulses, which were then repeated 30 times.

An optical fiber 400 µm diameter wide (ThorLabs, RJPSF2) coupled with a 470 nm wavelength LED (ThorLabs, M470F3) and powered by an LED driver (ThorLabs, DC2200) was used in order to deliver the pulses at constant intervals of 2500 ms.

All electrophysiological recordings were obtained with Spike-2 software (CED, Cambridge). The window settings, channel selection, and stimulus delivery were controlled by a custom written Matlab routines provided by Robert Egger (Max Planck Institute for Biological Cybernetics) and Daniel Udvary (Max Planck Institute for Neurobiology of Behavior - caesar).

While monitoring the waveform shape and frequency, the opening of the membrane was indicated by the sudden widening of the waveform, the disappearance of hyperpolarization, and the increase in frequency. This signifies the start of the filling session, which for proper labeling of the cell morphology, lasted between 5-10 minutes. Once finished, the current is shut off and the neuron is left to recover for 1-2 hours to achieve a proper diffusion of the biocytin.

From the wavelength recording, based on the shape and amplitude of the signal, neuronal action potentials were automatically detected with a custom-made Python script. The obtained dataset contains the timestamp of both each occurrence of the applied stimuli and all the action potentials detected.

It is important to point out that there is a delay between the timestamp of the stimulus generator and the deflection of the whisker in the animal’s snout. To more specifically assess the exact moment in which the information from the multi-whisker stimulus reaches the cortex, the timestamp for the stimulus presentation is corrected using the local field potential (LFP). The first deflection of this voltage drop corresponds to the onset of the thalamocortical evoked depolarization. Using the time of the first deflection of the LFP will correct all the external factors that could influence the stimulus timestamp, and therefore provide a more accurate reading of the electrophysiological response.

As a verification step, the first deflection of the LFP was calculated both on the original voltage trace and on its first derivative. On the former, the time of deflection was established as the point where the sharp depolarization began. On the latter, the time selected was evidenced as a sudden shift to a negative value, which corresponds to the negative slope of the original response (figure 9). Moreover, the LFP was also used as a verification step on the pipette position and virus expression. Since the LFP records the local activity, a strong depolarization after a multi-whisker stimulus was evidence of the positioning of the recording pipette in the barrel cortex. The same principle applies to the AAV injection. The correct injection of the virus and overall expression will be evidenced by a sharp LFP response after the light stimulus. The lack of response was taken as proof of unsuccessful viral expression.

The information on the stimuli and the action potentials was used to extract several features from these recordings, using custom-made Python scripts. The feature extraction was consistent between all neurons, all stimulus types, and all recording trials. The complete feature selection used for analysis is shown in table S1.

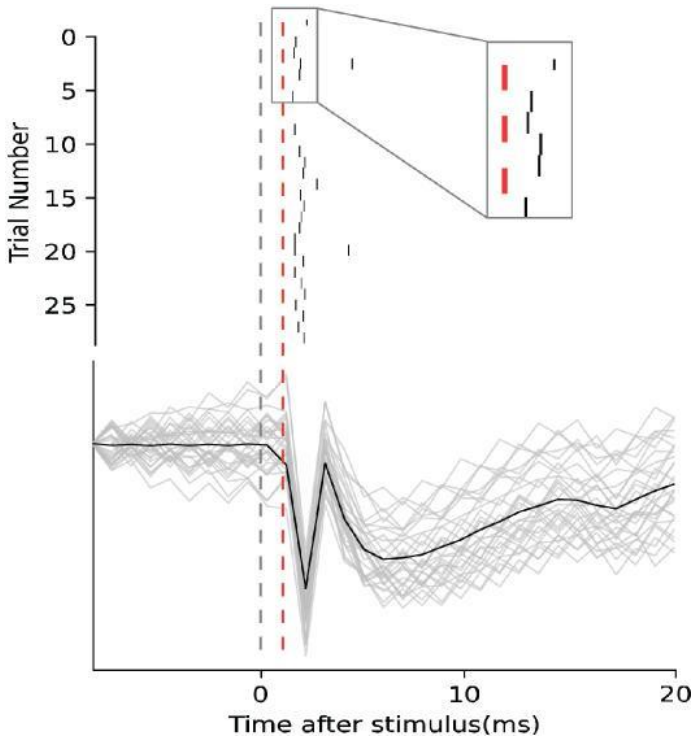


Fig 9: Latency determination & LFP correction

Example of LFP correction for the quantification of the latency of response. The first deflection on the LFP waveform corresponds to the thalamocortical onset and beginning of thalamic-induced activity in the cortex. The time between this LFP onset and the first evoked action potential corresponds to the latency of response.

### 2.1.3 Histology

Animals while still anesthetized were transcardially perfused with 0.9% saline (Sigma Aldrich, 746398) followed by approximately 50-100 ml 4% paraformaldehyde (Sigma Aldrich, 158127) solution in 100 mM PB (pH=7.2) until stiff to physical examination (Gage et al., 2012). Brains were removed and post-fixed with 4% PFA for 24 hours, transferred to 0.05 M phosphate buffer (PB), and stored at 4˚C. The left and right hemispheres were then separated by making a precise cut down the midline using a single-edged razor blade.

Once separated, one hemisphere was glued using cyanoacrylic glue onto a custom-built aluminum cutting block down on the medial side of the tissue so that the midline was facing away from the cutting blade with the brain surface facing upward towards the cutting blade. The custom aluminum block was then placed into the custom-built buffer chamber and raised at a 45˚C angle. This cutting angle is used so the slicing is done tangentially to the D2 column of the barrel cortex and therefore perpendicular to the cortical columns for better visualization (Finnerty et al., 1999). 50 µm thick sections were cut using a vibrating microtome (Leica, VT1200) ranging from the pial surface to the white matter which corresponds to 48 sections (figure 10).

The individual slices were placed in a 24-well tissue culture plates (1 slice per well) filled with 0.1 M PB in the order they were sliced and stored at 4˚C preserving that exact order until the immunohistochemical staining procedure.

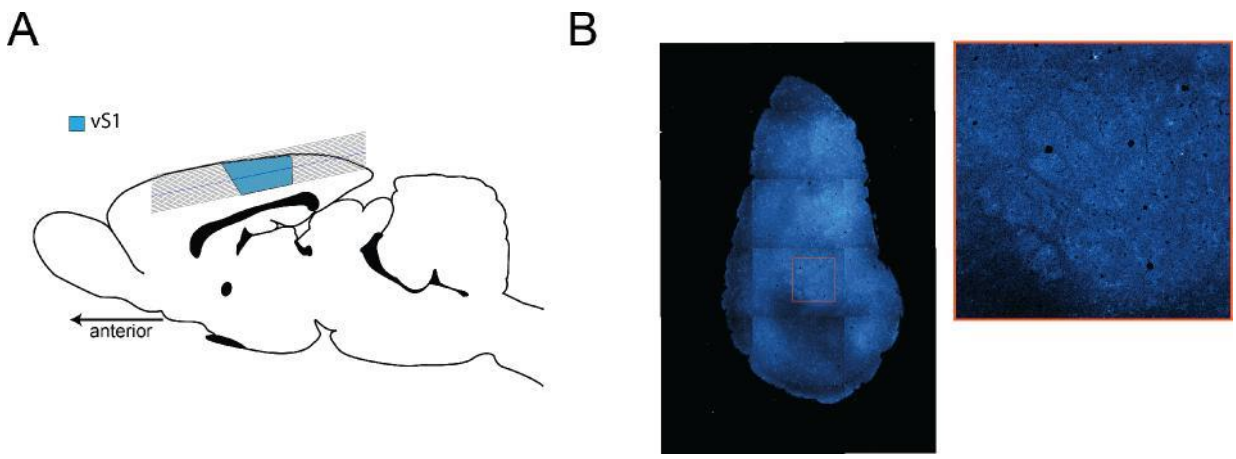


Fig 10: Tissue slicing and barrel identification.

(A) Diagram of slicing in the barrel cortex, 50 µm thick sections were cut tangentially to the barrel cortex. This procedure was done for morphological reconstruction and barrel identification. (B) An example image of a tangential slice of the brain, centered in the D2 column. A zoom-in image of the barrels shows the distribution and shape of each column. Barrel identification will be used for the alignment of the contours and posterior registration of neuronal morphology.

All brain slices were washed 5 times in 0.1 M PB solution and then treated with Streptavidin-AlexaFluor 488 conjugate (Molecular Probes, S11223) diluted (5 mg/ml) in 0.1 M PB with 0.3% Triton, 400 µL per well, for 2-3 hours at room temperature protected from light in a shaker at 30 rpm. The slices are then re-washed in 0.1 M PB five times and kept protected from the light at 4 ˚C in PB 0.1 M for future labeling.

After the biocytin labeling, all brain slices were permeabilized and blocked in 4% normal goat serum (NGS) (Jackson ImmunoResearch Laboratories, 005-000-121) in 0.1 M PB containing 0.5% TritonX-100 (TX) (Sigma Aldrich, 9002-93-1), 400 µL per well, for 2-3 hours at room temperature protected from light in a shaker at 30 rpm. The tissue was incubated with the primary antibodies in a 1:500 concentration in 0.1 M PB containing 1% NGS, 400 µL per well for 48-72 hs at 4 ˚C. The primary antibodies used were:

- Mouse IgG1 Anti-PV (Millipore, MABN1191)
- Rabbit IgG Anti-SST (Invitrogen, PA5-87185)

After the incubation time, the slices were washed five times in 0.1 M PB solution and incubated with the secondary antibody in a 1:500 concentration in 0.1 M PB containing 1% NGS, 400 µL per well for 2-3 hours at room temperature protected from light in a shaker at 30 rpm. The secondary antibody is conjugated with a fluorophore, in this case, the secondary antibody used was:

- Goat - IgG1 Anti-Mouse - AlexaFluor-647 (Invitrogen, A21240)
- Goat - IgG Anti-Rabbit - AlexaFluor-405 (Invitrogen, A31556)

The slices were then washed 5 times in 0.1 M PB solution and embedded with slowfade gold (Invitrogen, S36936) anti-fade protectant mounting medium on glass microscope slides and enclosed with a glass coverslip. The edges of the coverslips were then sealed with clear nail polish to prevent any leakage of the mounting medium and were stored at 4 ◦C.

### 2.1.4 Image acquisition

A fluorescence wide-field microscope (Olympus, BX51) equipped with a motorized 3-axis stage was used. The microscope was controlled using an image acquisition software (Objective Imaging Ltd, Surveyor).

The 48 sliced tissue sections were imaged. Wide-field, single z-plane images of the entire tissue section were taken, using a 4x dry objective at a resolution of 2.30 µm x 2.30 µm per pixel. A GFP filter cube was used to enhance the contrast between the tissue and the background, to be able to contour the pia, white matter, and barrels for the purpose of neuron morphology registration.

After the 4x images were obtained, the slices were imaged with a confocal laser scanning system for the purposes of morphological reconstructions and molecular labeling (Leica Microsystems, Leica Application Suite Advanced Fluorescence SP5) equipped with glycerol/oil immersion objectives (HC PL APO 10X 0.01 N.A., HC PL APO 20X 0.7 N.A., and HCX PL APO 63X1.3 N.A), a tandem scanning system (Resonance Scanner), spectral detectors with hybrid technology (GaAsP photocathode) and mosaic scanning software (Matrix Screener, beta version provided by Frank Sieckmann, Leica Microsystems) and a fluorescence wide-field microscope (BX51, Olympus).

A 700 µm x 700 µm area centered in the soma location of the labeled neuron was taken. In the case where the neuron projections expanded outside this 700 µm area, either a new image with a bigger size was taken, or another image following the aforementioned projections was taken (figure 11).

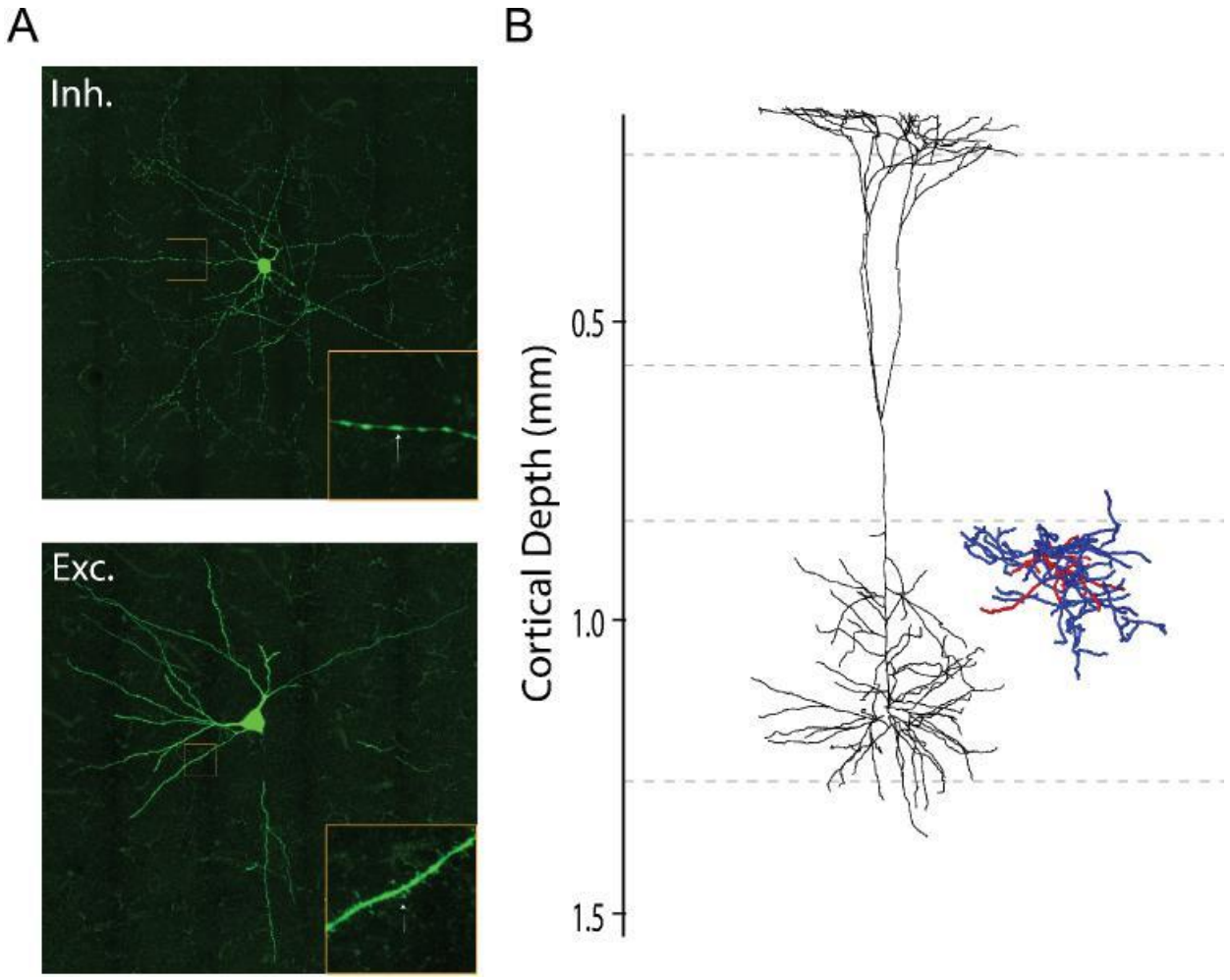


Fig 11: Anatomical reconstruction of labeled neurons

(A) Example of a 700 µm x 700 µm image used for morphological reconstruction. Neurons are identified as inhibitory or excitatory based on certain morphological characteristics (Yen et al., 1985). Example of inhibitory neurons in barrel cortex. Identification was based on their round shape soma, mostly local projections and dendritic swellings (A zoom-in area shows the characteristics beaded dendrites). The bottom image is an example of an L5PT neuron; dendrites of these neurons are characterized by the presence of spines, and project up to the superficial layers. (B) Full morphological reconstructions of the example neurons. In black, dendritic tree of the excitatory L5PT neurons. On blue and red, axonal and dendritic projections of the inhibitory neuron. Both are in layer 5 of the barrel cortex.

With the purpose of 3D reconstruction of axon and dendrites morphologies, 3D single channel image stacks of the whole thickness of the slice, which again corresponds to approximately 50 µm, were taken using the 63X immersion oil objective with 2.5 digital zoom, 8X line average, 8 kHz scanning speed, which provided a resolution of 0.092 x 0.092 µm per pixel. For these experiments, the targeted neuron was labeled with Streptavidin conjugated with AlexaFluor-488, while the rAAV injection, which in this area labeled the VPm projections, contained mCherry (excitation: 587 nm, emission detection range: 550-650 nm), but was enhanced with AlexaFluor-647.

The following excitation/emission settings were used:

- AlexaFluor-488 (excitation: 488 nm (Argon-laser); emission detection range: 495-550 nm)
- AlexaFluor-647 (excitation: 633 nm (HeNe-laser); emission detection range: 650-785 nm)

A super-resolution enhanced laser scanning system (Leica Application Suite Advanced Lightening Fluorescence SP8; Leica Microsystems) equipped with glycerol/oil immersion objectives (HC PL APO 10x 0.4 N.A., HC PL APO 20x 0.7 N.A., and HCX PL APO 63x 1.3 N.A.), a tandem scanning system (Resonance Scanner: 8kHz scanning speed), spectral detectors with hybrid technology (GaAsP photocathode; 8x line average), was used for the molecular marker labeling of the cell body of the biocytin labeled neurons from the in vivo recording experiments.

Each neuron was labeled with two antibodies against parvalbumin and somatostatin, conjugated with AlexaFluor-647 and AlexaFluor-405 respectively, because of the biocytin label, the soma was also stained with AlexaFluor-488.

For this purpose, the laser settings used were:

- AlexaFluor-405 (excitation: 405 nm (UV-diode laser); emission detection range: 410-455nm)
- AlexaFluor-488 (excitation: 488 nm (Argon laser); emission detection range: (495-550 nm)
- AlexaFluor-647 (excitation: 647 nm (White Light laser); emission detection range: 650-785 nm)

Sequential triple-channel image stacks of a 700 µm x 700 µm area with 0.5 µm step size in the z direction, centered in the soma location of the labeled neuron were taken using the 40X immersion objective which provided a resolution of 0.161 x 0.161 µm per pixel as determined by the default settings of the lightening suite software.

### 2.1.5 Determination of putative synapses in AAV injected neurons

The rAAV injected into the VPm expressed channelrhodopsin the thalamocortical terminals which allows for optogenetic stimulation, and also contained a fluorescent protein (mCherry) for anatomical visualization. As mentioned before, an area of 700 µm x 700 µm x 50 µm, was taken using the 63X objective.

In this 3D stack, we could use the overlap between the rAAV signal and the dendrites of the neuron as a maximum bound of possible synapses (Egger et al., 2020). In these neurons, the overlap between the swellings of the dendrites and the boutons of the axons of VPm neurons was used as the landmark for the putative synapse quantification. An overlap was marked as a putative synapse if the axon boutons were found at a distance of no more than 1 µm from the swellings of the target dendrite (figure 12).

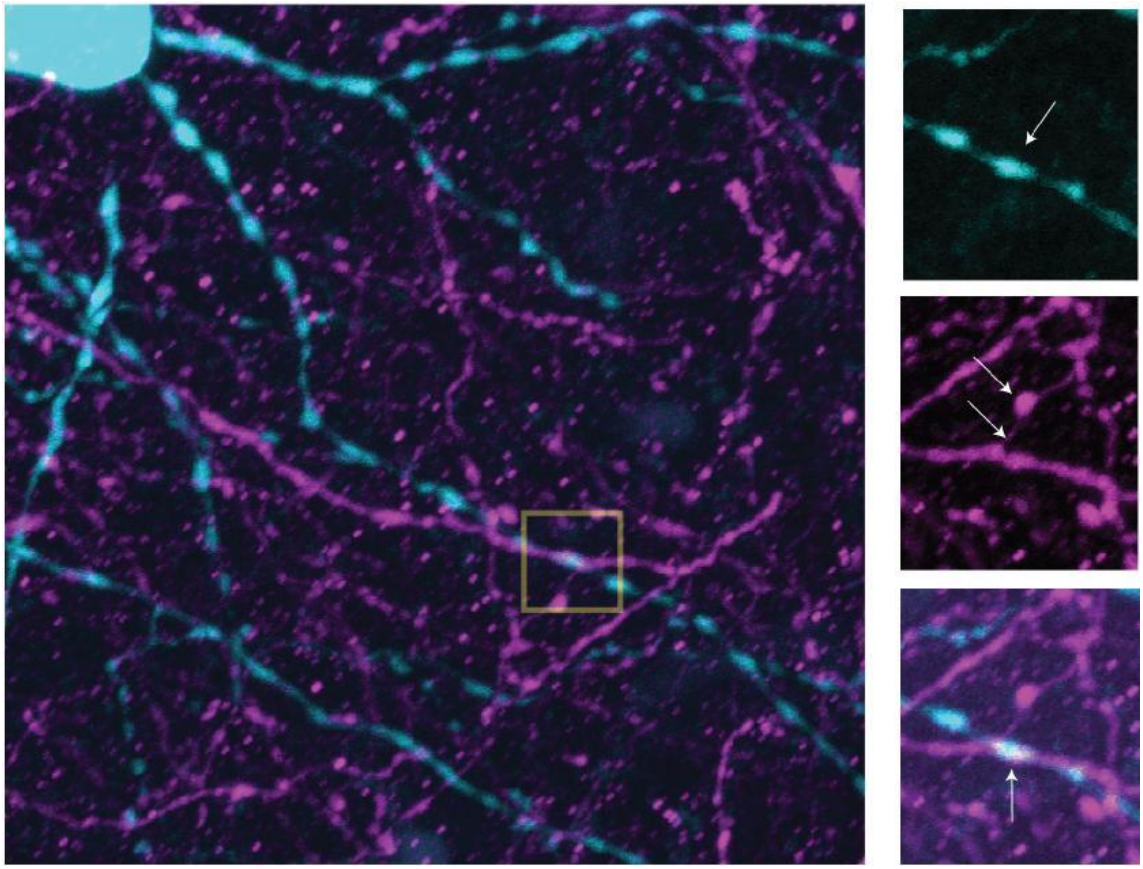

Fig 12: Quantification of putative synapses

Determination of putative synapses for in-vivo recorded neurons. Cyan and magenta show the biocytin and AAV labelings respectively. The overlap between a dendritic swelling in the biocytin channel and an axonal bouton in the AAV channel was quantified in a 3D stack. Putative synapse was considered when the distance between both landmarks was less than 1 µm in all three axes.

Several dendrites were analyzed for each neuron. Dendrites were selected according to their length (~ 100 µm). The number of swellings was kept as consistent as possible between samples (average of 23.61 ± 8.10 (n = 23)). These results were compared across animals to assess the correlation between axon and dendrite overlap with the electrophysiological response.

### 2.1.6 Morphological reconstruction of biocytin labeled neurons.

Morphological reconstruction of biocytin labeled neurons from in vivo electrophysiological recording experiments was based on a previously described method for semiautomatic reconstruction of neuron morphology (Oberlaender et al., 2007).

The 3D image stack was deconvolved using linear Tikhonov-Miller algorithm and theoretically computed the point spread function of the confocal microscope (Oberlaender et al., 2009) using Huygens software (SVI, the Netherlands). Using a custom-designed software, neuronal structures were automatically detected. In order to assess the quality of automatic detection and proof edit the tracing results, an adaptation of the Amira software (ThermoFischer) was used based on previous work (Dercksen et al, 2014). 3D dendrite and axon morphologies were merged, aligned, and spliced together using the aforementioned software in order to recover the full morphology of the labeled neuron.

Making use of the 4x images of the whole slice obtained from the wide-field microscopy, the pia surface, white matter tract, and layer 4 barrels from the barrel cortex were drawn manually to obtain anatomical references for the anatomical registration of the reconstructed morphologies on a standardized 3D reference frame of the barrel cortex (Egger et al., 2012) for further morphological analysis.

### 2.1.7 Quantification of molecular-labeled somata

The image stack provided by the super-resolution confocal laser microscope was merged using the default “Leica mosaic system” provided within the lighting software. The mosaics were then aligned and compared in each image channel (i.e. AlexaFluor-405, AlexaFluor-488, AlexaFluor-647) separately.

Double-labeled neurons were determined as those that were marked in the AlexaFluor-488 channel (corresponding to the biocytin labeling) and one of the other channels (figure 13). As a validation step, in order to quantify a neuron as either positive or negative, a necessary requirement was that there was at least one other positive labeled neuron in the image taken, to make sure that the staining was successfully done.

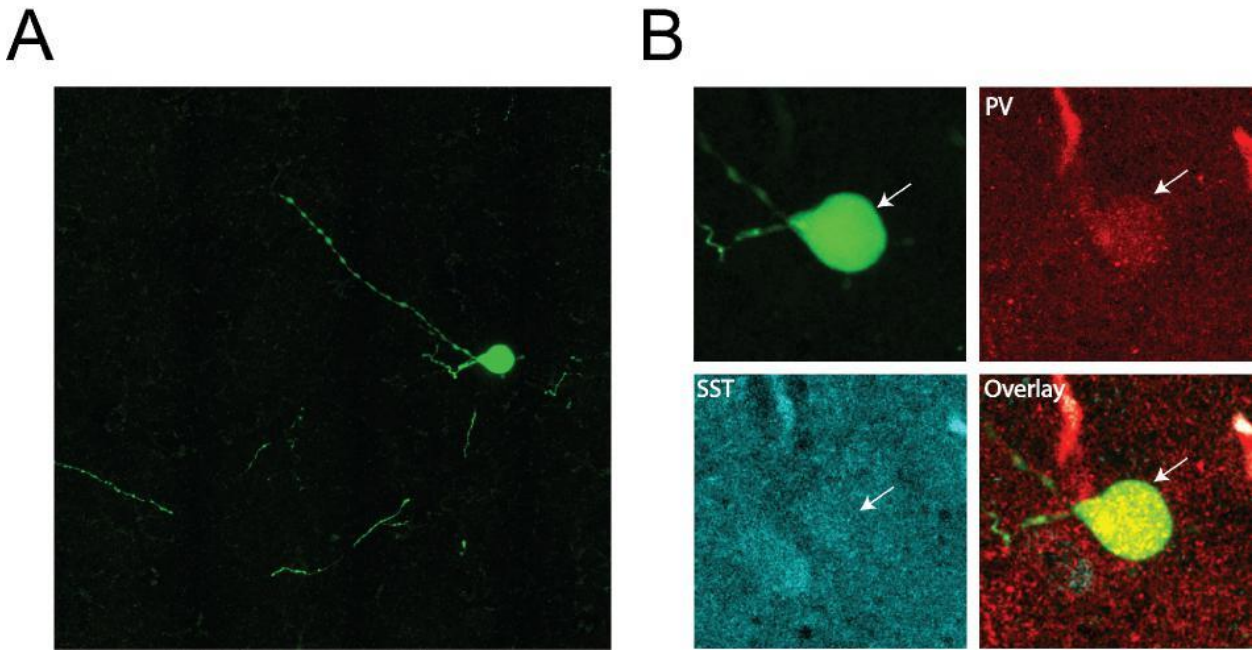


Fig 13: Molecular identity determination of labeled inhibitory neurons.

Immunohistochemical staining on morphologically identified inhibitory neurons. (A) Example of a biocytin labeled L5 inhibitory neuron, with characteristic beaded dendrites and round-shaped soma. (B) Zoom-in on the soma and staining against the aforementioned molecular markers. In red, antibodies against parvalbumin conjugated with AlexaFluor-647. In cyan, antibodies against somatostatin were conjugated with AlexaFluor-405. The overlay shows positive staining for PV for this example.

## 2.2 Primary thalamocortical innervation onto the inhibitory neuron population

In order to complement the study of individual inhibitory neurons, trans-synaptic tracer injections were used for the anatomical assessment of thalamocortical input from the primary thalamus in the inhibitory population of the barrel cortex. To this end, I adapted a trans-synaptic viral injection method (Zingg et al., 2014, 2017) for the quantification of the neurons in the barrel cortex, which are monosynaptically connected to the VPm nucleus in the thalamus.

### 2.2.1 Trans-synaptic neuronal tracer injection

Neuronal tracer injections were done in a similar fashion as explained in the section above. The same glass injection capillaries and injection devices as for the monosynaptic tracer injections were used. The injections, in this case, consisted of a mix of the AAV1-modified viral tracer pEEN-AAV1-hSyn-Cre-WPRE-hGH (Addgene, $1.8x10^{13}$ gc/ml) and AAV2-hSyn-DIO-mCherry (Addgene, $4.0x10^{12}$ vg/ml) in the VPm nucleus, and an AAV2-hSyn-DIO-EGFP (Addgene, $3.0x10^{12}$ vg/ml) injection in the barrel cortex, both of the left hemisphere.

The coordinates to target layer 5 of the barrel cortex were modified from (Vijayan et al., 2010).

- BC: 5.5 from the midline, 2.75 posterior from bregma, and 1.8 mm deep from pia.

A schematic of the experimental procedure can be seen in figure 14. The addition of AAV2-DIO conjugate in the barrel cortex of the animal allows the AAV1 injected in the thalamic nuclei to jump a synapse and replicate in the post-synaptic neurons. Given the conjugation of the second virus with a fluorophore, the neurons that possess a monosynaptic connection with the thalamic nuclei will be fluorescently labeled. Animals injected with trans-synaptic tracers underwent a 21-23 day incubation period before being transcardially perfused.

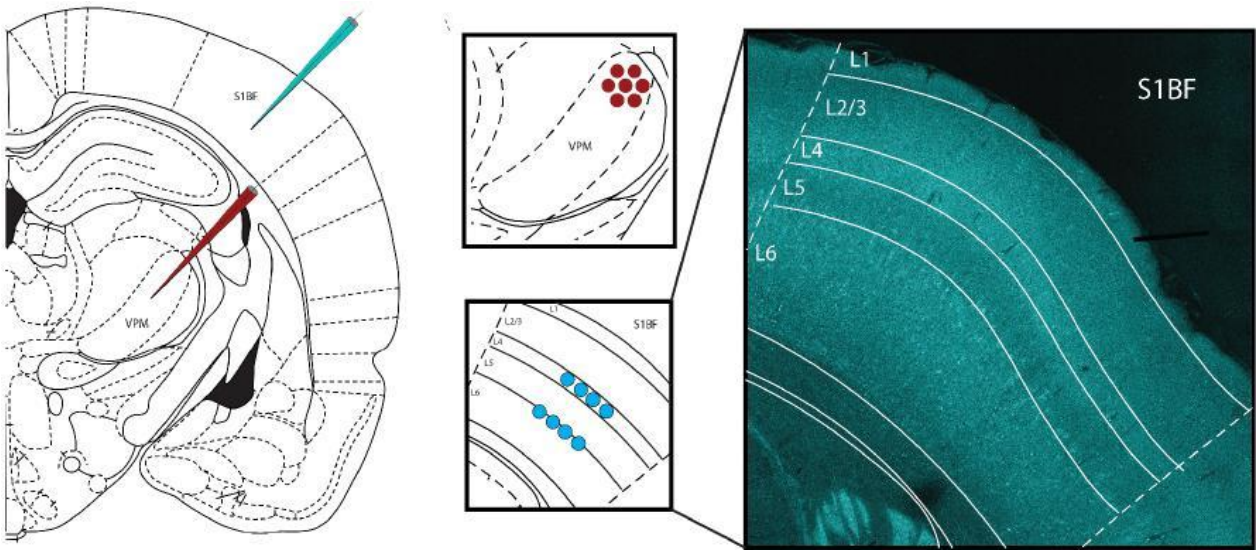


Fig 14: Trans-synaptic viral injections in thalamic nuclei and barrel cortex

Schematic of the injection procedure for a trans-synaptic virus combination. In red, the injection consisted of a mix of the AAV1-modified viral tracer and AAV2-hSyn-DIO-mCherry in the VPm nucleus. The virus will spread through the neuron body of the VPm neurons, labeling them with mCherry (red). In cyan, an AAV2-hSyn-DIO-EGFP injection in the barrel cortex. This conjugation will allow the AAV1 in the thalamic neurons to synaptically jump to those connected neurons in the barrel cortex, labeling them with eGFP (cyan). A successful VPm injection can be assessed by the concentration of labeling in layers 4 and 6, with almost no labeling in other layers.

### 2.2.2 Histology

In the case of the animals injected with trans-synaptic tracers, in order to better assess the projections of the thalamic nuclei, coronal slicing was done around the area of the thalamus and barrel cortex, using the Paxinos atlas (Paxinos & Watson, 2007) as a reference. 50 µm thick sections were cut.

Because the brain tissue tends to be unstable when performing coronal slices, they were previously embedded in a 10% gelatin solution made by dissolving 10 g of gelatin from porcine (Sigma Aldrich G2500-500) in 50°C 100 mM PB. Prior to the embedding, the cerebellum, brainstem, and spine were dissected and removed from the rest of the brain with a single-edged razor blade.

The remaining tissue consists mainly of both brain hemispheres. A square mold was used to shape the gelatin, brain hemispheres were placed upwards, and the gelatin solution was slowly pipetted into the mold chamber. The gelatin embedding is done in stages, letting the molted gelatin solidify before adding more to the chamber until the whole brain is covered, this prevents the brain tissue from floating. The gelatin was left to solidify for 30 minutes at room temperature before cooling the chamber for at least 2 hours at 4°C.

The gelatin blocks were then removed from the chamber making sure not to damage either the gelatin or the tissue and were trimmed into a trapezoid shape, with a larger base and a smaller top, and a small notch on the left side of the gelatin. The trapezoid shape creates a more stable mold for better slicing, and the notch on the left side was used as a marker for the orientation of the slice when imaging.

In these experiments, the injections were conjugated with mCherry (VPm) and eGFP (barrel cortex). On top of these, sections were labeled with antibodies either against NeuN, parvalbumin, or somatostatin. All these labelings were done with a secondary antibody conjugated with AlexaFluor-405.

### 2.2.3 Image acquisition

The same Leica super-resolution confocal system described previously was used for the imaging of these slices. In this case, the laser settings were slightly different than the ones previously described with the exception of the AlexaFluor-405

- AlexaFluor-405 (excitation: 405 nm (UV-diode laser); emission detection range: 410-455nm)
- eGFP (excitation: 488 nm (White light laser); emission detection range: (480-540 nm)
- mCherry (excitation: 561 nm (White light laser); emission detection range: 550-650 nm)

Triple-channel image stacks of a 240 µm x 240 µm area with 1 µm step size in the z direction, centered in the injected column of the barrel cortex were taken using the 10X immersion objective with a 1.7X digital zoom, which provided a resolution of 0.260 x 0.260 µm per pixel.

### 2.2.4 Molecular identification on trans-synaptic labeled neurons

The image stack provided was merged and compared in each image channel (i.e. AlexaFluor-405, eGFP, mCherry) separately. Double-labeled neurons were determined as those that were marked in the eGFP channel (corresponding to the barrel cortex injection) and the AlexaFluor-405 channel corresponding to the molecular marker selected. The NeuN labeling was used to determine the layer borders of the barrel cortex and compare the distribution of AAV2 (eGFP) labeled somata in the barrel cortex.

The layer borders were determined by the density of somata. L1 is characterized by a low somata count. L2/3 gradually increases the number of somata compared to L1, but a sharp increase in soma density marks the L4 border. The density of somata diminishes again in L5 until the L6 border where it increases again. A successful VPm injection of a trans-synaptic virus can be assessed by the concentration of barrel cortex labeling in layers 4 and 6, with almost no labeling in the other areas.

## 2.3 Molecular labeling of inhibitory neurons across vS1

To assess how representative the inhibitory dataset was, I performed a set of control experiments in which I stained and labeled against the non-overlapping markers of the inhibitory population in the rat cortex.

Images were taken and manually quantified using Amira software. Quantification was jointly done with Felipe Yáñez. Specifically, each result was double checked to reduce experimental bias. The data shown here represents the consensus result between both of us. The plots shown in figure 30 and figure 31 were done using custom made scripts written by Felipe Yáñez.

### 2.3.1 Histology

Similar to the procedures before, all brain slices were permeabilized and blocked in 4% normal goat serum (NGS), 400 µL per well, for 2-3 hours at room temperature protected from light in a shaker at 30 rpm.

All the tissue was stained twice, first with antibodies against the particular molecular marker, these being parvalbumin, somatostatin, or vasoactive intestinal peptide, and then against glutamate decarboxylase, being GAD67 a known marker for inhibitory neurons in the central nervous system (Fong et al., 2005). The tissue was incubated with the primary antibodies in a 1:500 concentration in 0.1 M PB containing 1% NGS, 400 µL per well for 48-72 hs at 4 ˚C.

The primary antibodies used were:

- Rabbit IgG Anti-PV (Invitrogen, PA1-933)
- Rabbit IgG Anti-SST (Invitrogen, PA5-87185)
- Rabbit IgG Anti-VIP (Invitrogen, PA5-85616)

The procedure continued exactly as described for the other staining protocols. The secondary antibody is conjugated with a fluorophore used was:

- Goat - IgG Anti-Rabbit - AlexaFluor-647 (Invitrogen, A32733)

At this point, I performed the second round of staining, in order to label GAD67-positive neurons. For this staining, the whole staining protocol is repeated with the difference that tissue is incubated with the primary antibodies in a 1:500 concentration but only for 24 hrs.

The primary and secondary antibodies used were:

- I° Antibody: Mouse- IgG2a Anti-GAD67 (Millipore, Mab5406)
- II° Antibody: Goat - IgG2a Anti-Mouse - AlexaFluor-488 (Invitrogen, A21121)

The slices are kept protected from the light at 4°C in PB for no more than 2 hours before storage.

### 2.3.2 Image acquisition

The same wide-field microscopy procedure mentioned in the previous section was used to generate 4x images of the whole slice for the anatomical references, the pia surface, white matter tract, and layer 4 barrels from barrel cortex using an adaptation of the Amira software (ThermoFischer) (Dercksen et al., 2014). This allowed us to obtain a 3D volume of the barrel cortex of each experiment.

For quantification of molecular labeling in the barrel cortex, each slice was imaged with a dual channel confocal mosaic scan, using the 10X glycerol objective with 1.7 digital zoom, 8X line average, 8 kHz scanning speed, which provided a resolution of 0.868 x 0.868 µm per pixel.

For all experiments, the following excitation/emission settings were used:

- AlexaFluor-488 (excitation: 488 nm (Argon-laser); emission detection range: 495-550 nm)
- AlexaFluor-647 (excitation: 633 nm (HeNe-laser); emission detection range: 650-785 nm)

These images were also used for the section alignment and ROI determination required for the following imaging session. In order to be able to quantify the molecular marker labeling, after the acquisition of optical slices of the whole barrel cortex, a 3 mm X 3 mm area, centered in our previously established region of interest (ROI) was taken.

The whole thickness of the slice, which corresponds to approximately 50 µm, was imaged with a dual channel confocal mosaic scan, using the 20X glycerol objective with 2.0 digital zoom, 8X line average, 8 kHz scanning speed, which provided a resolution of 0.361 x 0.361 µm per pixel.

Each stack was aligned and comprised of ~100 images stacked one over the other. The stacks contained two channels, one corresponding to the AlexaFluor-488 (which in this case labeled GAD-67 positive neurons) and one to the AlexaFluor-647 (Which labeled the molecular marker to analyze, them being either parvalbumin, somatostatin, or vasoactive intestinal peptide).

For the quantification of labeled neurons, a 1 mm x 1 mm area centered in the D2 column was set, and using the Amira in-built function for landmark labeling, each positive neuron in this area was labeled as a landmark. This was repeated for both channels and across slices in order to have the full quantification of every labeled neuron of the previously established area in the 3D barrel cortex, which corresponds to roughly the D2 columns and the surrounding septa (figure 15).

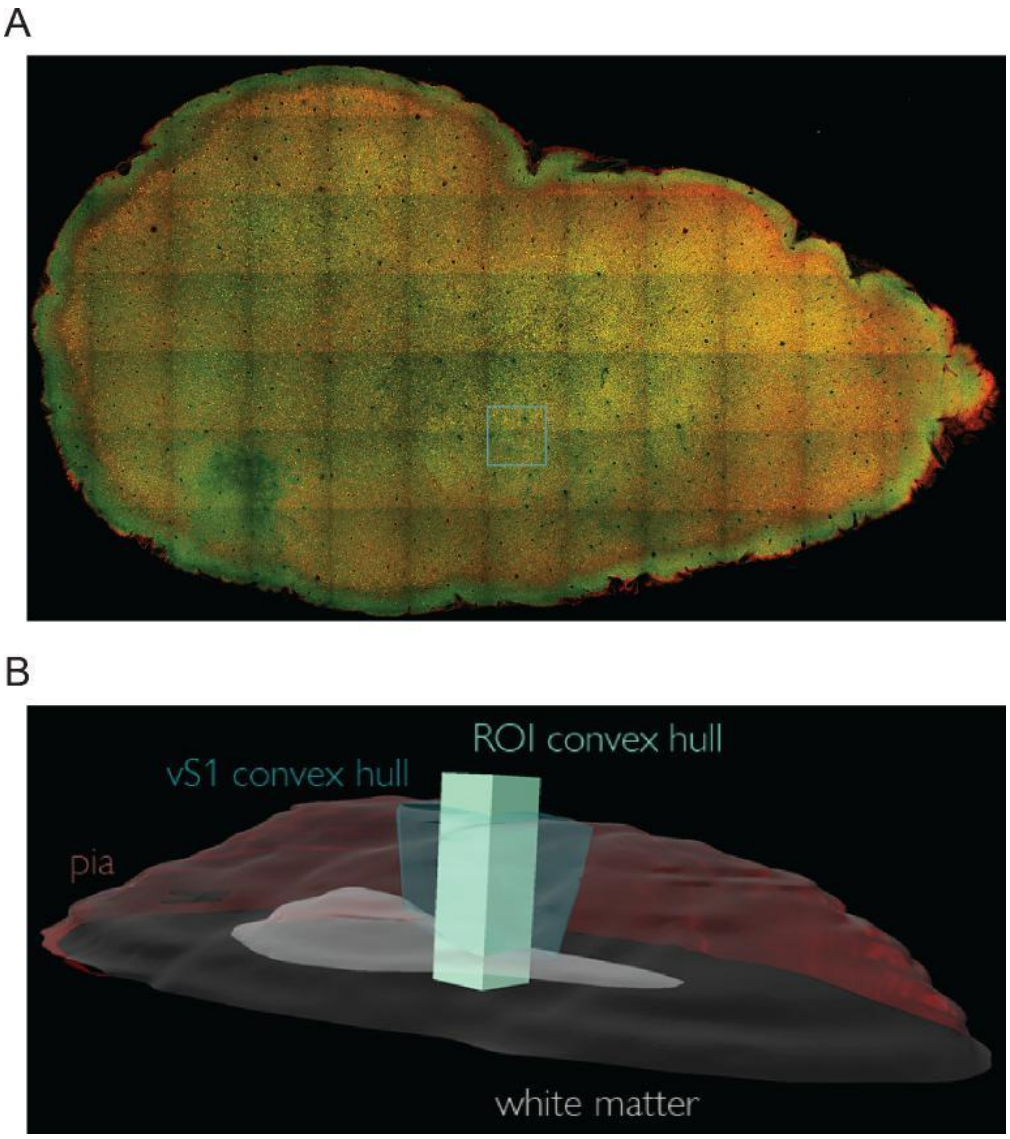


Fig 15: Quantification of molecular identity in a 3D column

(A) Example slice of immunological staining of a whole brain section. In green, GAD-67 staining against all inhibitory interneurons. In red, immunohistochemistry against parvalbumin, one of the main molecular groups of inhibitory neurons in the neocortex. From these sections, an area of 3 mm x 3 mm centered on D2 was used to image the whole barrel cortex and aligned to create a full 3D volume. (B) Schematic representation of a 3D reconstruction of the barrel cortex and D2 column. The alignment of the sections allowed for a reconstruction of the pia and white matter. As mentioned before, two 3D volumes were obtained, in darker blue the barrel cortex, and in lighter blue, the region of interest (ROI) for the complete immunohistochemistry quantification, centered in the D2 column (Schematic provided by Felipe Yáñez).

The resulting dataset for the D2 column contains a distribution of positive cells according to depth. This translates into a GAD-67 positive dataset, an only molecular marker positive dataset, and a double-labeled dataset. Double-labeled neurons were determined as those that were unequivocally positive in both channels and shared the landmark in the same position (figure 16).

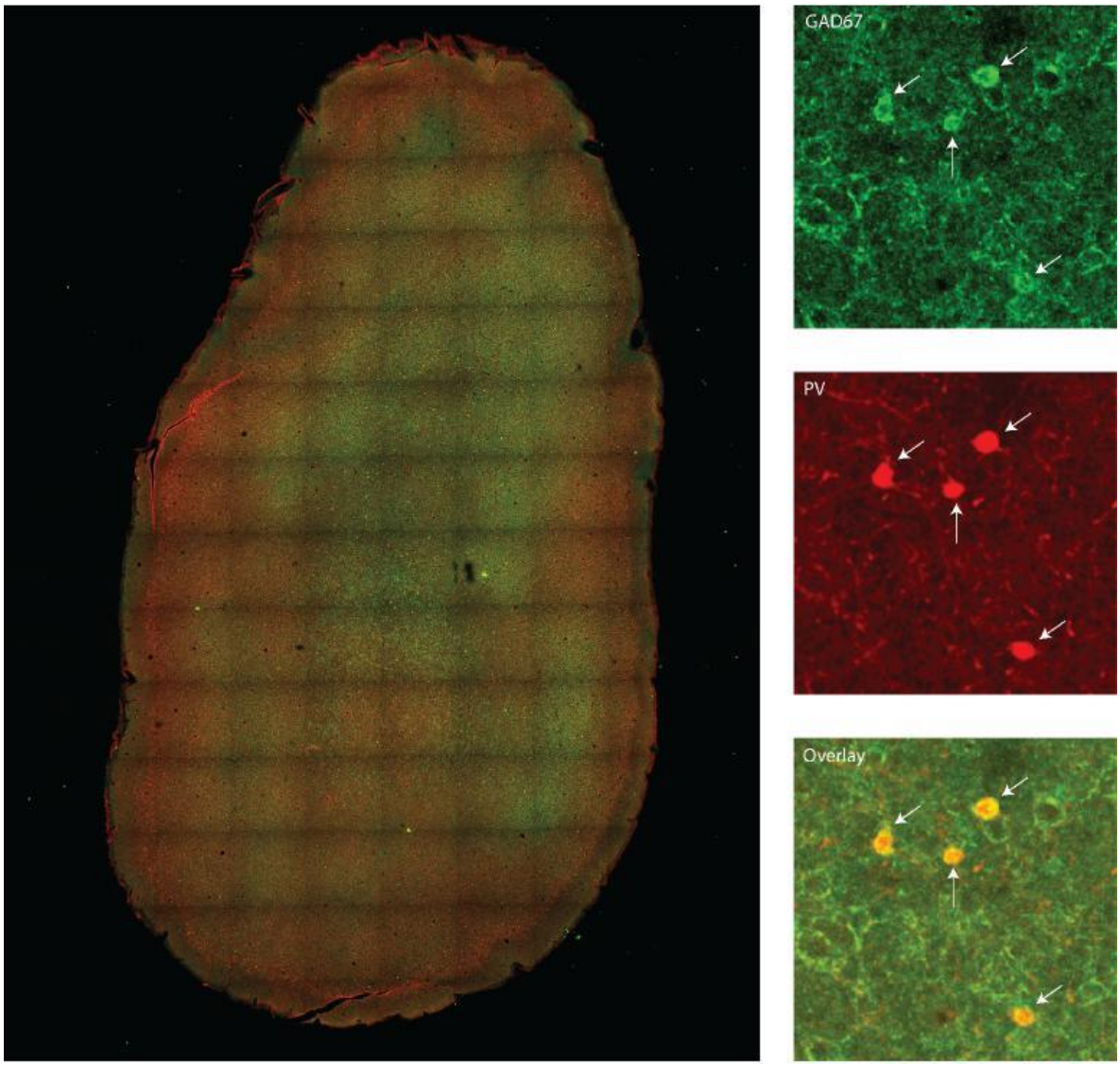


Fig 16: Molecular determination of the inhibitory population in vS1

An example image of complete neocortex labeling. Staining was done against GAD67 for complete inhibitory population labeling, and against parvalbumin. The number of positive cells for each case was counted for a 1 mm x 1 mm area centered in the D2. Numbers were reported as the densities and corresponding fractions of positive neurons.

# 3. Results

## 3.1 Electrophysiological response patterns of inhibitory neurons in vS1

Before the stimulation protocol started, once a neuron was detected and stabilized by adjusting the capacitance and pipette distance, a 90-second recording session was done. There are two reasons to do this. First, the long recording session allowed the neuron to set into a stable distance, which yielded better recordings once the stimulus protocols were started. Second, this recording was used for the calculation of a baseline spontaneous firing frequency. The spontaneous activity of this population was incredibly varied. These inhibitory neurons had an average of 3.30 ± 3.98 Hz spontaneous frequency but ranged from 0.40 Hz in the least active ones to 19.39 Hz in the more active cases.

### 3.1.1 Evoked responses to multi-whisker stimulation

For the airpuff stimulation, there is on average a 26.6 ms delay between the stimulus initiation and the activation of the thalamus. The stimulus time is adjusted with the first deflection of the local field potential (LFP) measured in the neocortex (figure 17).

The sensory evoked action potential responses after the stimulus presentation showed an average frequency of 19.09 ± 14.82 Hz. In 33/33 (100%) cases the overall evoked frequency increased. The average increase was 80.66 ± 17.23%, shown in figure 18. Distribution of the action potentials during the evoked response shows that they are not homogeneous throughout the 700 ms long stimulus, instead, they are in most cases concentrated as a sharp response in the first 50 milliseconds (Towle et al., 1980). This manifests the importance of investigating separately the initial window, which we defined as the onset response. The rest of the evoked response was defined as sustained. Both cases can be seen in figure 18.

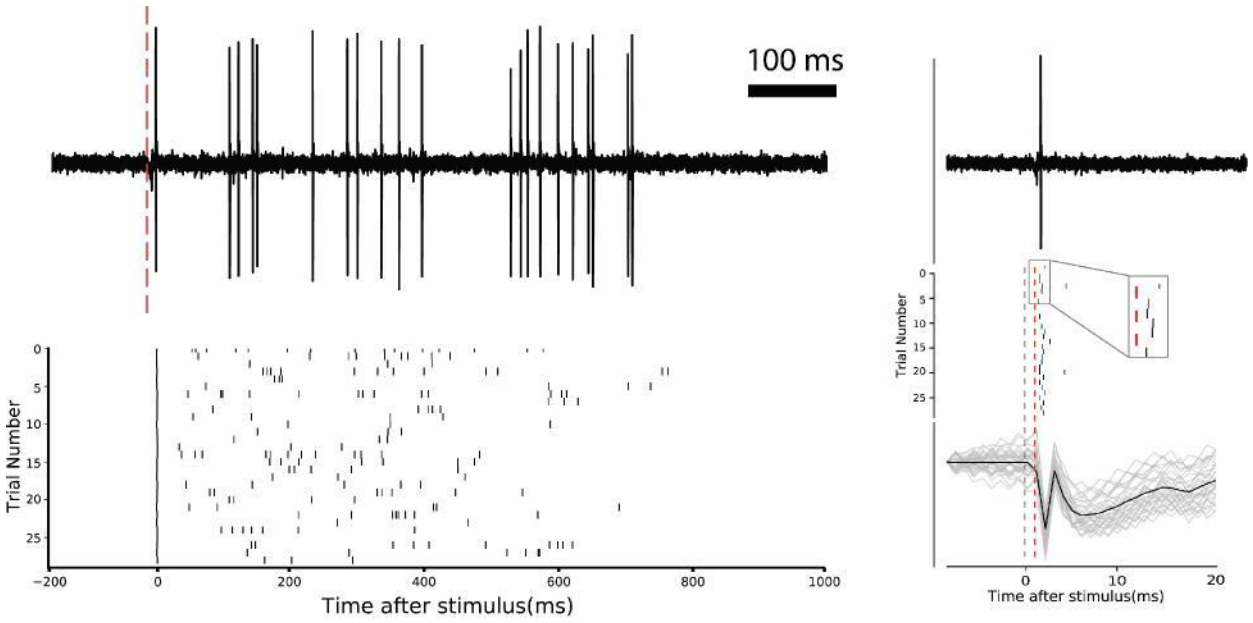


Fig 17: Electrophysiological recording in vS1

Example of an electrophysiological recording of an inhibitory neuron. On top, the raw trace of the recording, the action potentials (AP) can be identified by the sharp depolarization and repolarization. Bottom, the rasterplot of that recording. Each tick corresponds to an AP and each row to a trial, this protocol contains 30 trials. The presentation of the stimulus corresponds to the zero in the time window. Left panel shows a zoom-in on the first AP, both for the trace and rasterplot. The variability in the response can be seen and the stimulus presentation time is corrected to the first deflection of the LFP for latency quantifications.

I explore the possibility that there was a relationship between the strength or shape of the response a neuron had, with their positioning in the depth of the cortex. Of the 33 recorded neurons, 12 were located in layer 4 and 21 in layer 5. Neither their spontaneous activity 4.00 ± 3.72 Hz and 2.90 ± 4.15 Hz respectively (n = 33, two-sided t-test, p = 0.45) showed significant differences between layers. The same result was obtained for their onset responses 23.26 ± 18.81 Hz and 18.17 ± 14.28 Hz respectively (n = 33, two-sided t-test, p = 0.39), or their sustained response 8.59 ± 9.16 Hz and 6.49 ± 8.75 Hz (n = 33, two-sided t-test, p = 0.52).

In all electrophysiological analyses in our protocol, there were no significant differences between L4 and L5 for the inhibitory population. The complete set of electrophysiological features extracted for comparisons was explained in the corresponding methods section and can be seen in table S1.

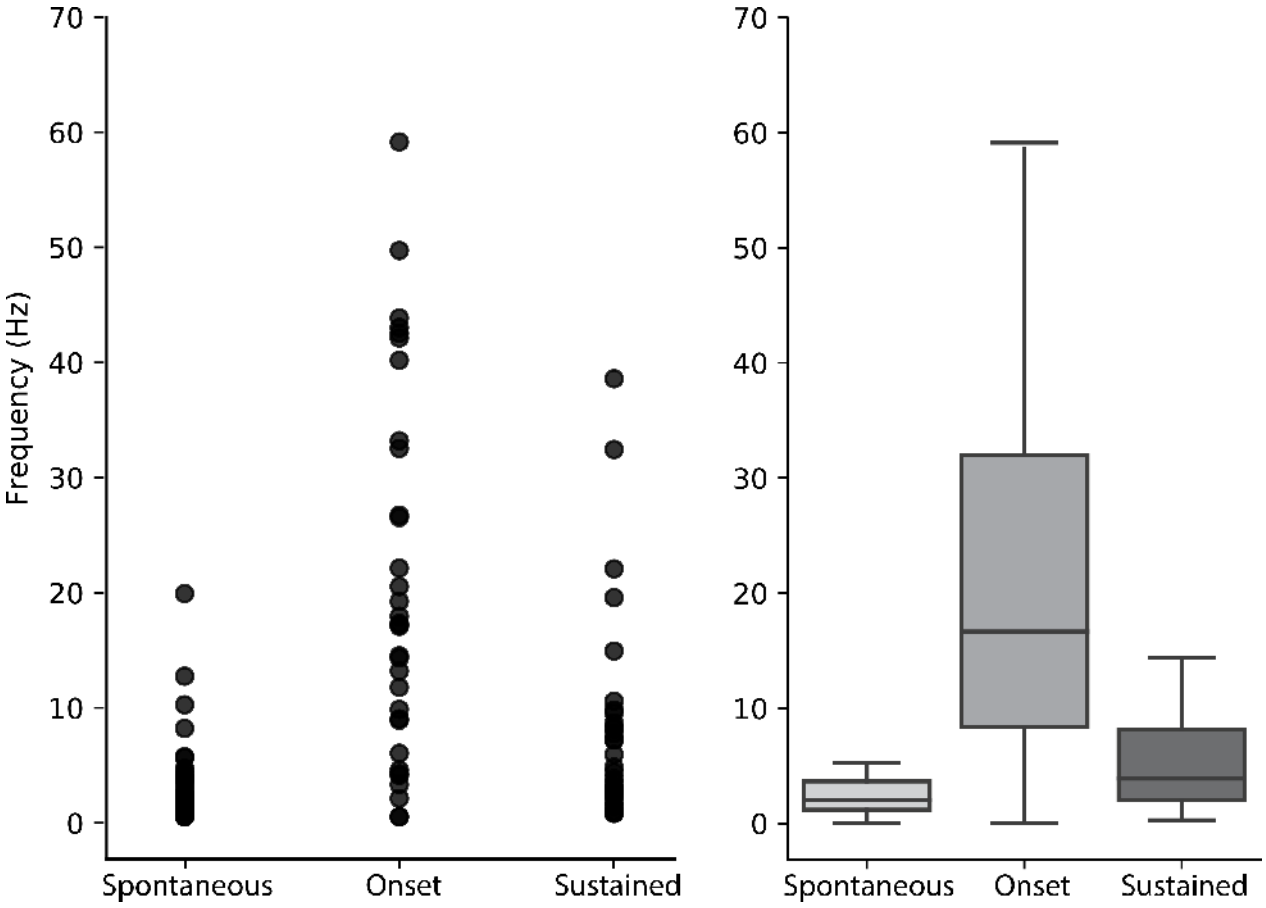


Fig 18: Spiking activity in Inhibitory interneurons

Comparison between the spiking frequency of all inhibitory neurons. The left panel shows each neuron's frequency during their spontaneous activity, their onset response at their first 50 ms after the stimulus presentation, and their sustained response for the whole duration of the 700ms multi-whisker stimulation. The right panel shows a boxplot with the median responses. The onset response is stronger than either their onset response or sustained, but in all cases, evoked activity shows an increase in their firing rate.

### 3.1.2 Response properties to photo-stimulated thalamocortical synapses

Right after the multi-whisker stimulation, the animal was left to rest for 10 minutes before starting the optogenetic manipulation. This consisted of direct stimulation of the thalamocortical synapses by 10 ms of pulsed light through an optical fiber positioned just above the cortical surface in close proximity to the recording site.

Three different photostimulation protocols were done: 10ms pulsed light with an inter-stimulus-interval of 2500ms (0.40Hz), same light stimulus with an inter-stimulus-interval of 500ms (2 Hz), and again with an inter-stimulus-interval of 100ms (10 Hz).

Similar to what was done for the airpuff stimulation, the stimulus time is adjusted with the first deflection of the local field potential (LFP) measured in the neocortex. In this case, there is on average a 1.96 ms delay between the stimulus initiation and the activation of the thalamus. In the case of optogenetic manipulation, only 25 of those 33 morphologically identified neurons could be activated by optogenetic stimulation of thalamocortical synapses.

Of all optogenetic protocols, the first one to be done was the 0.4 Hz. Similar to the analysis done for the multi-whisker stimulation, the sensory evoked action potential responses after the stimulus presentation showed an average frequency of 26.56 ± 22.76 Hz. In 22/25 (88%) cases, the overall evoked frequency increased, by an average of 86.69 ± 16.91% (figure 19). In the light stimulation, the evoked response was even sharper than before, most spikes focused on the first milliseconds of the response, what we had defined as the onset response. In the case of the sustained response, no activity could be found.

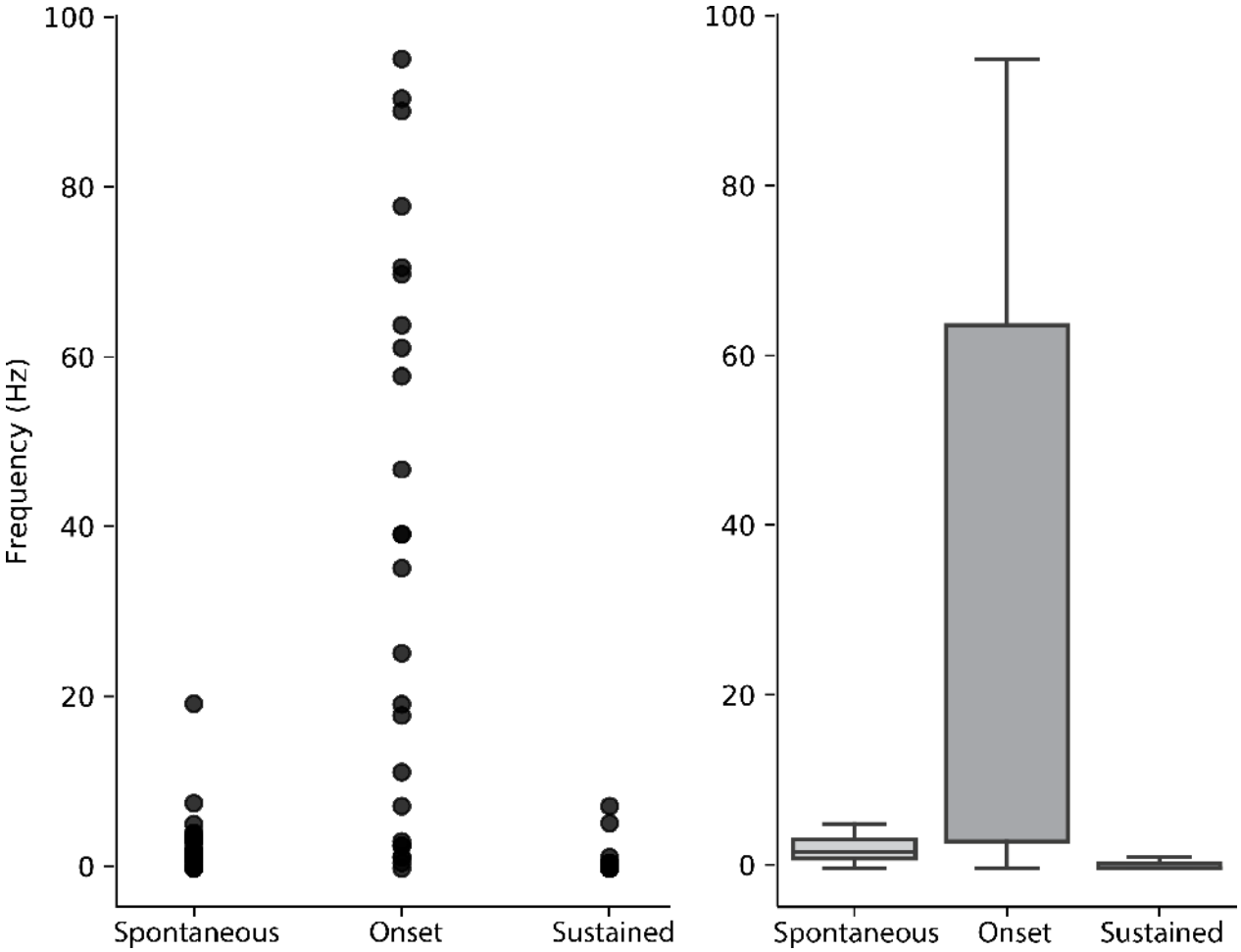


Fig 19: Spiking activity after optogenetic activation of TC synapses

Comparison between the spiking frequency of all inhibitory neurons for the optogenetic stimulation. As before, the left panel shows each neuron's frequency during their spontaneous activity, their onset response after the stimulus presentation, and their sustained response. The right panel shows a boxplot with the median responses. The onset response is considerably stronger than the rest, owing to the fact that a direct VPm stimulation shows a sharp fast response while the light stimulation is active (10 ms), but little to no response once the stimulus is finished.

### 3.1.3 Activation of inhibitory neurons can either precede or succeed those of excitatory cells.

In order to investigate the direct role of the thalamocortical input in the activation of the inhibitory neurons, I focus first on the latency to which these neurons respond to the stimulus. The latency of response is measured as the delay between the stimulus presentation and the evoked neuronal activity (Friedman & Priebe, 1998). In cortical circuits, the synaptic latency for a monosynaptic connection falls between 1 and 2 ms (Miles & Wong, 1986).

In the case of the multi-whisker stimulation, of the 33 neurons, only those that showed some response in the first 50 milliseconds after the LFP onset, were considered responding neurons, which in our dataset corresponded to 24/33 (72.7%).

I analyzed the latency of response of all the recovered neurons in our dataset (figure 20). The excitatory population had a median response of 4.69 ± 1.80 ms (n = 11). Meanwhile, the latency response of the inhibitory population had a shorter latency, with a median value of 3.66 ± 9.68 ms. I compared these two populations and showed that the inhibitory population responds faster than the excitatory one.

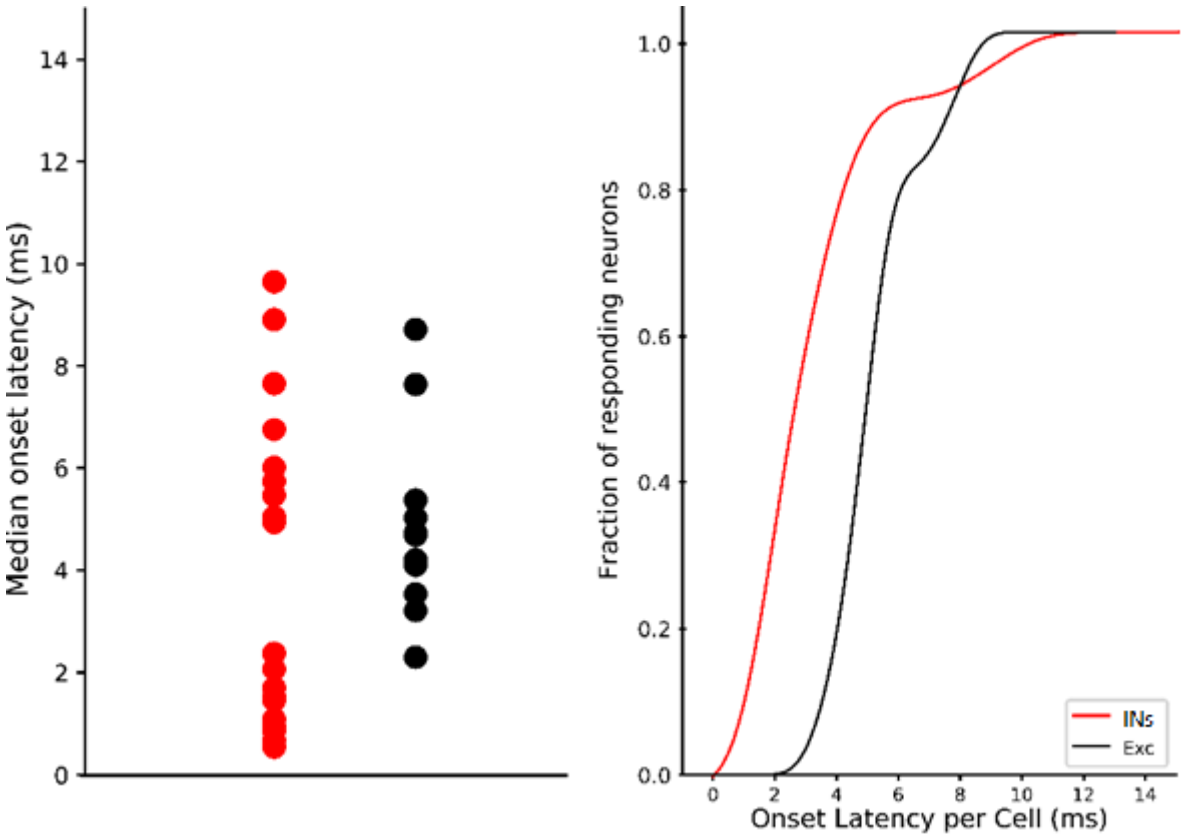


Fig 20: Latency responses in inhibitory and excitatory neurons

Median latency responses of all inhibitory and excitatory neurons to the multi-whisker stimulation. Left panel shows the distribution of responses for the excitatory and inhibitory neurons. Right panel shows the cumulative responses. As a population, inhibitory neurons have an earlier response.

Interestingly, when visualizing the individual responses of each of the recorded neurons, I see that the excitatory population has a continuous distribution of latencies. This is not the case for the inhibitory neurons, the inhibitory neurons show a bimodal distribution, with a particular lack of responses between 2.39 ms and 4.94 ms, exactly where the excitatory population responses are concentrated (figure 21).

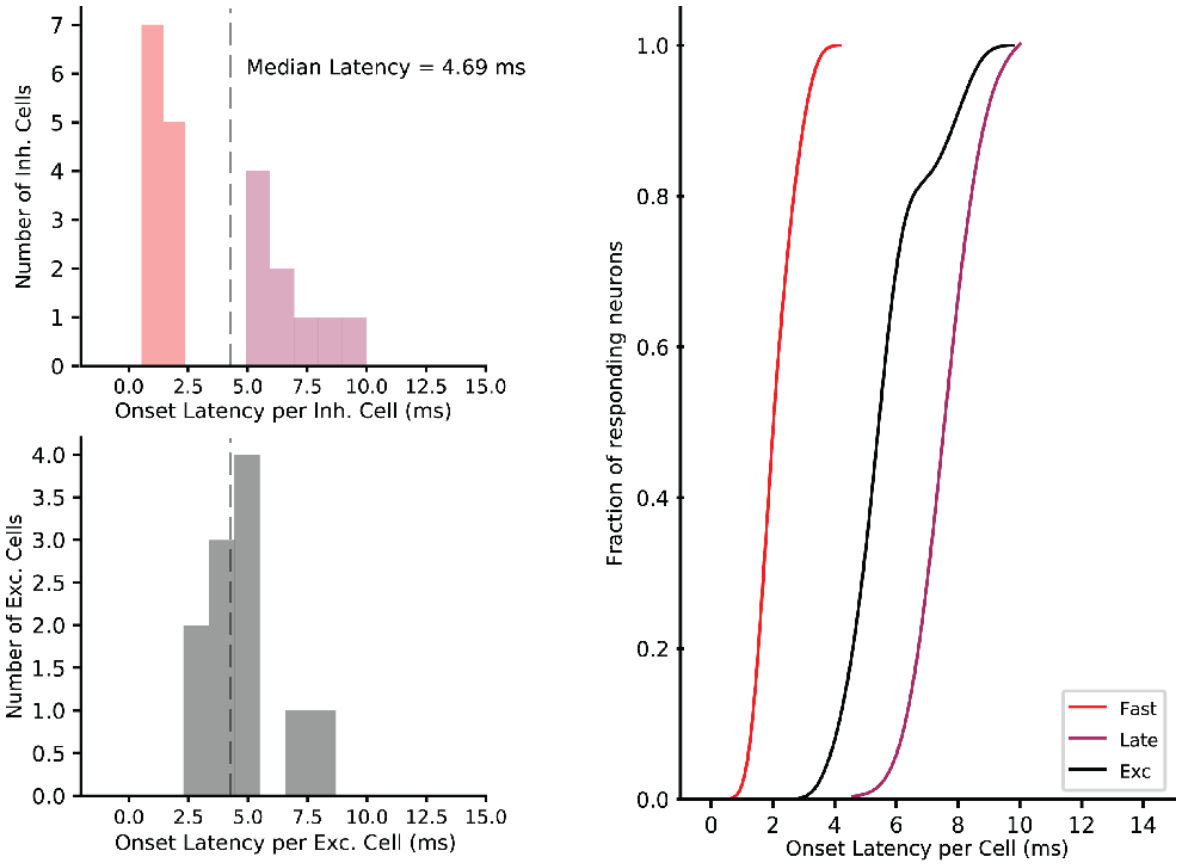


Fig 21: Bimodal distribution of INs responses to a multi-whisker stimulation

Distribution of median latency responses of INs (top) and excitatory neurons (bottom). The median latency of the excitatory population (4.69 ms) separates the bimodal distribution of INs responses into those that precede and those that succeed excitation. Right panel shows the cumulative fraction of responses of median latencies. The cumulative responses of these 3 populations show that they are separated by 2-3 ms, a time consistent with a monosynaptic jump.

The bimodal distribution and the excitatory population show a group of inhibitory neurons that respond faster to the multi-whisker stimulation, with a median response of 1.02 ± 0.60 ms (n = 12) and preceded the excitatory response by a time consistent with a monosynaptic latency (Doyle & Andresen, 2001; Miles & Wong, 1986). On the other hand, a set of inhibitory neurons succeeds the excitatory population, consistent again with a monosynaptic latency, with a latency response of 7.21 ± 11.71 ms (n = 12).

The populations preceding and succeeding the excitatory response show statistically significant differences ($p = 0.0035$, multi-sample comparison test with post hoc pairwise comparison using the Bonferroni correction) in their latency response.

I performed a Kolmogorov-Smirnov test (KS-test) to evaluate the probability that these two sets of inhibitory neurons were drawn from the same probability distribution. In the case of the KS test, the null hypothesis states that both populations can be drawn from the same distribution. A p-value smaller than 0.05 means that we can reject the null hypothesis that the distributions are identical. In my case, the comparison between the population that preceded the L5PTs excitation (fast responders) and the ones that succeeded the excitatory population (late responders) had a $p = 7.4 \times 10^{-7}$

I also evaluated the latency of response to the optogenetic activation. Similar to what was explained before, of the 25 neurons those that responded in the first 50 milliseconds after the LFP onset were considered “responding neurons” and in this case were 19/25 (76%). In the three stimulation protocols (0.4 Hz, 2 Hz, and 10 Hz), the median latency was 1.62 ± 6.95 ms, 2.85 ± 2.75 ms, and 2.93 ± 3.45 ms respectively. For all following analysis, I will focus only on the 0.4 Hz protocol, which has the same inter-stimulus interval as the multi-whisker stimulation.

Again, I analyzed the latency of response of all the recovered neurons in our dataset (figure 22). The excitatory population had a median response of 3.47± 2.51 ms (n = 11). The inhibitory neurons show the same bimodal distribution as before, with a lack of responses between 1.72 ms and 4.23 ms, again where most of the excitatory population responses are concentrated (figure 22). The bimodal distribution for the optogenetic manipulation shares the same overall shape as the one shown for the multi-whisker stimulation.

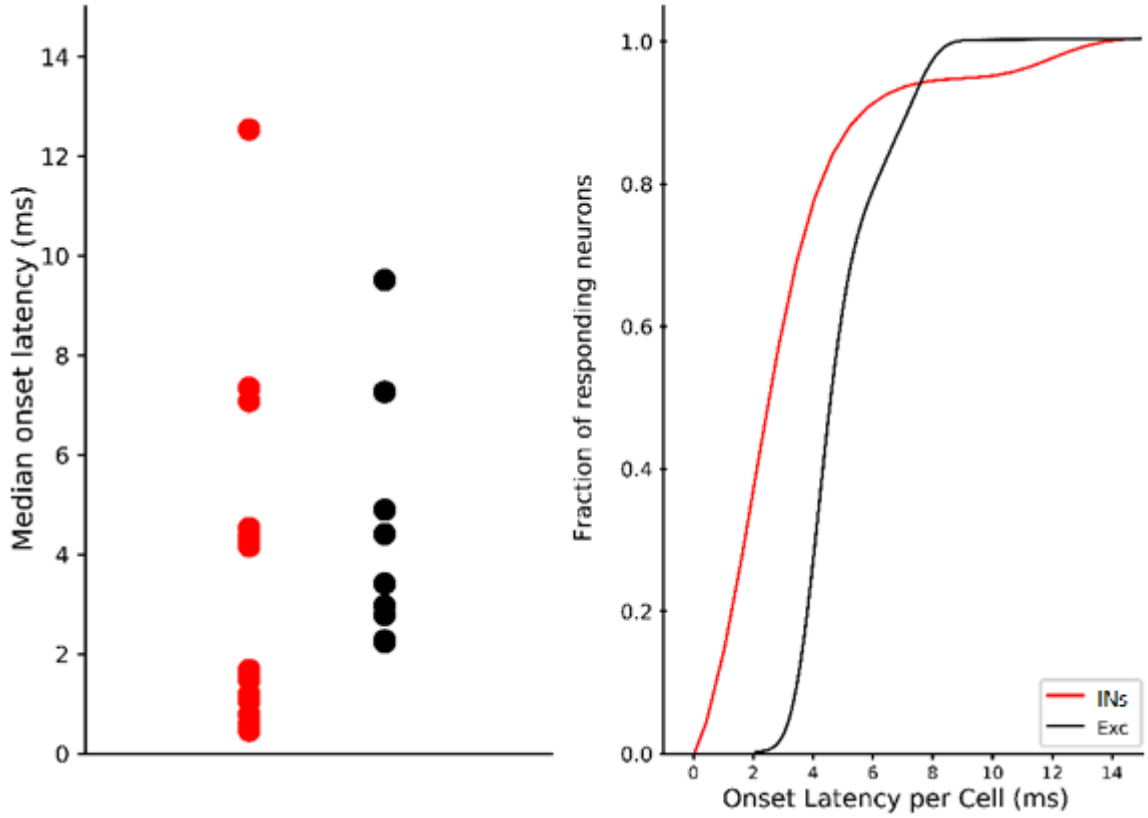


Fig 22: Latency of response after optogenetic activation

Median latency responses of all inhibitory and excitatory neurons to the optogenetic manipulation. The latencies shown in this figure correspond to the 0.4 Hz stimulation protocol. The left panel shows the distribution of responses for the excitatory and inhibitory neurons. The right shows a plot of the cumulative responses. As a population, inhibitory neurons have an earlier response, consistent with the results and with previous stimulation protocols.

The group of inhibitory neurons that preceded the excitatory population, did so with a median response of 1.08 ± 0.46 ms (n = 11). In turn, the inhibitory neurons that succeeded them showed a median response of 5.89±8.82 ms (n = 8) (figure 23). These populations are statistically significantly different (p = 0.0056, multi-sample comparison test with post hoc pairwise comparison using the Bonferroni correction). The Kolmogorov-Smirnov test (KS test) between the two inhibitory populations for the optogenetic manipulation had a $p = 2.65 \times 10^{-5}$.

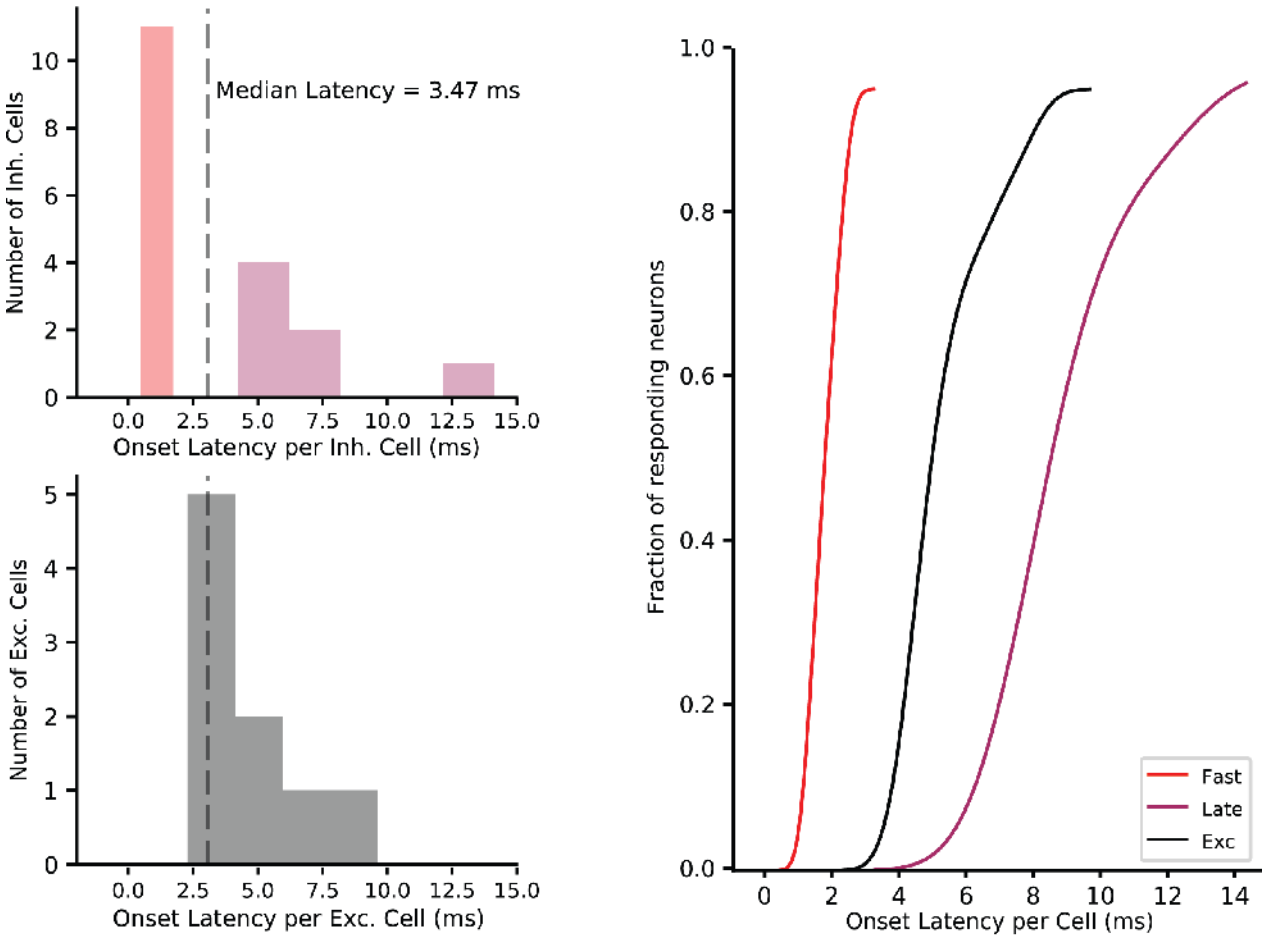


Fig 23: Bimodal distribution of INs responses to an optogenetic manipulation

Similar to what was shown for the multi-whisker stimulation. Distribution of latency responses of inhibitory (top) and excitatory neurons (bottom). The median latency of excitatory cells (3.47 ms) separates the bimodal distribution of INs responses into those that precede and those that succeed excitation. Right panel shows the cumulative fraction of responses of median latencies. The cumulative responses of these three populations show the same separation of 2-3 ms between each other, consistent with a monosynaptic jump.

Given that the results of the latency analysis are so similar for the multi-whisker stimulation and the optogenetic activation, I investigated the possibility that those neurons that precede the excitatory population in one case, do so in the other. A quick overview of the identities of these neurons showed that %100 (25/25) of the recording neurons have similar responses to both stimuli. To confirm this, I performed a KS test and compared these groups between stimuli. Those that respond fast to the multi-whisker and optogenetic activations, had a $p = 0.694$ after the KS-test. Those that succeeded the excitatory neurons had a $p = 0.150$ after the same test. This means that those neurons belong to the same population.

### 3.1.4 Electrophysiological properties of fast and late inhibitory neurons

The latency analysis showed two distinct populations of inhibitory neurons, a group that preceded all excitatory activation, and a set of inhibitory neurons that succeeded them. Given these differences in their response patterns, I explored which other electrophysiological properties could be different between these populations.

#### Firing frequency

First, I explored the spontaneous activity. When comparing fast and late responders, their spontaneous activity measured $2.01 \pm 1.94$ and $3.22 \pm 5.88$ respectively ($n = 33$) and there were no significant differences between these two groups (two-sided t-test, $p = 0.0965$). These results were reflected when comparing their onset and sustained responses. Neither their onset responses $32.0 \pm 14.26$ and $21.6 \pm 13.84$ ($n = 33$, two-sided t-test, $p = 0.146$), nor their sustained response $6.72 \pm 6.54$ and $4.31 \pm 12.9$ ($n = 33$, two-sided t-test, $p = 0.475$), showed significant differences.

Interestingly, when comparing the optogenetic manipulation I found that the onset response of those fast-responders was significantly higher than those late-responders, independent of the protocol used. At the 0.4 Hz stimulation, those that preceded the excitation had an evoked response frequency of 64.42± 24.87 Hz, compared to 26.02 ± 21.57 Hz of those that had a delayed response (n = 25, two-sided t-test, p = 0.0029) (figure 24).

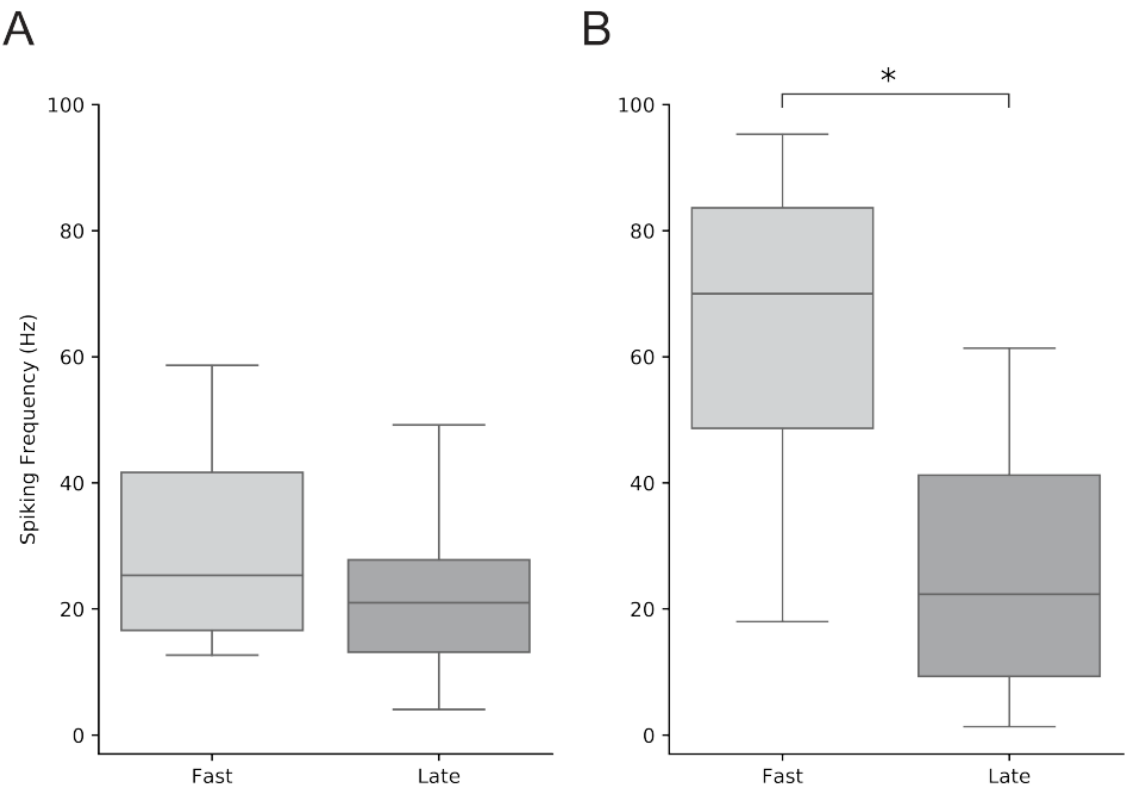


Fig 24: Spiking frequency comparison between fast and late responders

Comparison between evoked onset frequencies on fast and late responders. (A) Evoked frequencies during the first 50 ms after a multi-whisker stimulus presentation. There was no significant difference between those response groups. (B) Frequencies after optogenetic stimulation, the comparison shows significant differences between the two groups, pointing to the possibility that the strength of thalamocortical input can be responsible for these differences.

There was no difference in the evoked responses during the sustained window. While the reason for these differences is not clear, it seems that those that precede the excitatory population also have a strong sharp response to the direct activation of the thalamocortical synapses. This, combined with their latency results, denotes the possibility that the main difference between groups relies on their thalamocortical input.

### Adaptation

Stimulus adaptation can be defined as the change in activity in response to a repetition of the same stimulus. Usually, neuron activity adapts with a rapid change of the response pattern at the beginning, and then later stabilizes into a new value (Katz et al., 2006). Normally, neuronal adaptation will decrease in activity in response to excitatory stimuli. However, neurons can also adapt by increasing their spiking ability (Aizenman et al., 1999; Heiss et al., 2008).

Here, I investigated how the inhibitory neurons in our dataset modified their spiking activity after the repeated presentation of the same multi-whisker stimulus. I compare the number of action potentials across trials, during a determined time period. Neurons went from an average of 0.088 ± 0.081 spikes per 10 ms in the first trial to an average of 0.062 ± 0.060 spikes per 10 ms in the last, there was no significant difference between them (n = 33, two-sided t-test, p = 0.14) (figure 25).

Besides the spiking frequency, I compared the adaptation in terms of their latency of response. I wanted to evaluate if they would adapt to the stimulus by responding with a shorter latency. The latency of responses went from an average of 5.12 ± 9.41 ms in the first trial to an average of 10.71 ± 14.52 ms in the last, again with no significant differences (n = 33, two-sided t-test, p = 0.137). There was no consistent increase or decrease in the latency response across trials. The results obtained showed that there was no generalized adaptation in the inhibitory population.

I analyzed if there were any differences in the adaptation between the two groups. Those neurons that preceded the excitation showed a median latency of 0.77 ms in the first trial and a median of 1.21 ms in the last, and there was no significant difference between them (n = 12, two-sided t-test, p = 0.63).

Similarly, the neurons that succeeded the excitatory population had a latency of 4.21 ms in the first trial and a median of 10.25 ms in the last, there was no significant difference between them (n = 12, two-sided t-test, p = 0.94).

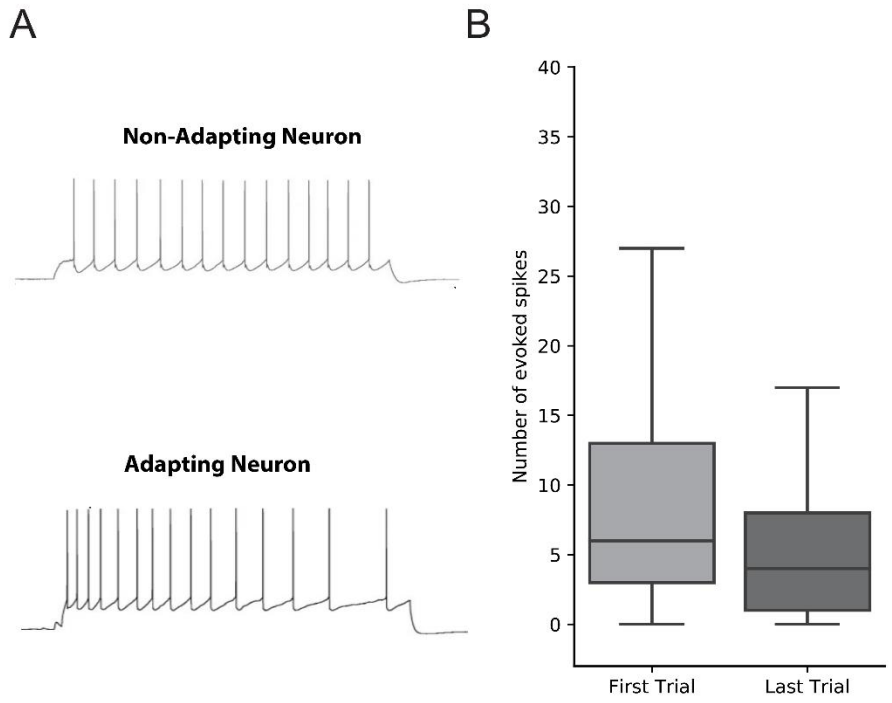


Fig 25: Firing rate adaptation in Inhibitory interneurons

Left panel shows an example of the adaptation measurements. Neurons can adapt to the stimulus by diminishing their firing rate after several stimulations (adapted from Popescu et al., 2017). Right panel shows the number of evoked APs on the first trial for each of the recorded neurons and the last. The average number per trial was smaller although not significant. In the individual cases, none of the neurons showed signs of adaptation.

In the case of the optogenetic activation, I compared the number of action potentials across trials. From an average of 6.12 ± 4.20 spikes per 10ms in the first trial to an average of 5.08 ± 3.19 spikes per 10 ms in the last, there was no significant difference between them (n = 25, two-sided t-test, p = 0.34). In the other two stimulation protocols, average spikes per 10 ms remained close to one another.

To see if the latency of responses has been affected by the continuous stimulation, I repeated the analysis I did for the multi-whisker stimulation, but for the optogenetic protocols. The latency of responses went from an average of 2.61±2.23 ms in the first trial to an average of 4.09 ± 6.65 ms in the last, again with no significant differences (n = 25, two-sided t-test, p = 0.35). Similar to what I saw for the multi-whisker stimulation, there was no consistent increase or decrease in the latency response across trials.

These results confirm that there was no generalized adaptation in the inhibitory population, independent of the type of stimulation that was provided. I couldn't find any evidence of either an increase or a decrease in the frequency, strength, or timing of their evoked responses.

### Bursting activity

Burst then can be defined as three or more action potentials that occur within 30 ms (Bast, Guest et al., 2023). It has been proposed that neurons may use intracellular calcium not only to regulate their membrane excitability but also to control the network bursting pattern (Kudela et al., 2009).

Bursting activity in the inhibitory population shows a high degree of variation. The average burst responses went from 5.36± 6.70 before the stimulation protocol began, to 5.15 ± 10.39 during the onset of response (figure 26). The multi-whisker stimulation had little effect on the bursting activity of these neurons. Nevertheless, compared to the multi-whisker stimulation, the bursting activity after the optogenetic manipulation seems to be completely different. The light-evoked response shows a higher number of bursts during the onset part of the response.

There were little to no spikes during the spontaneous nor sustained responses and a strong activity during the 10 ms light stimulation. Interestingly, doublets and triplet events corresponded to 60.93% of all action potentials in those responding neurons. Doublet events increase from an average of 0.16 ± 0.37 before the stimulus, to 6.04 ± 9.12 events during the onset response.

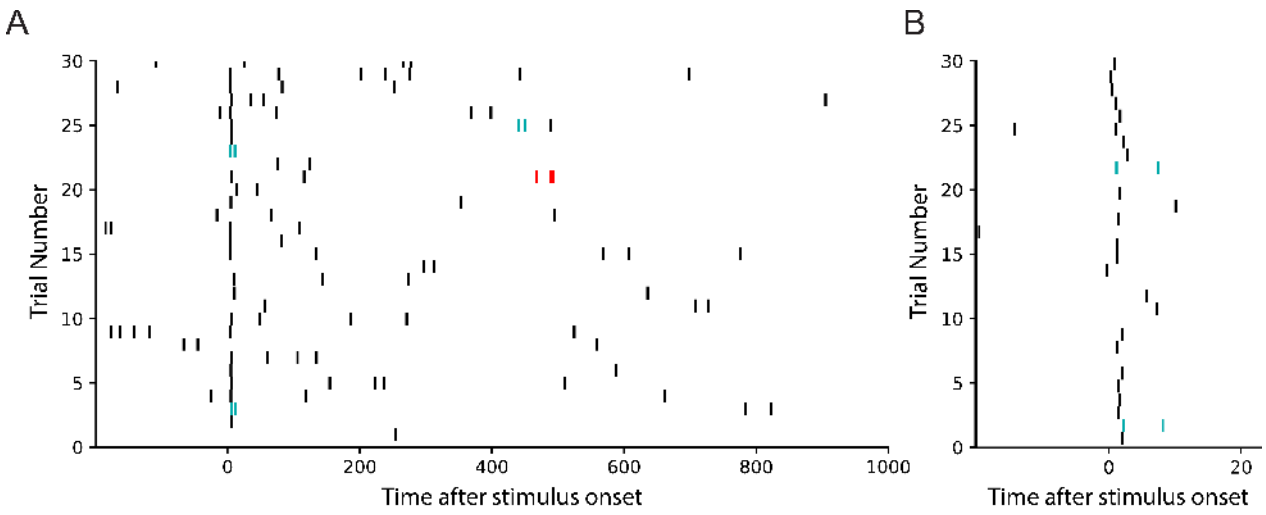


Fig 26: Bursting activity after stimulus presentation

(A) Example rasterplot of an inhibitory neuron response to a multi-whisker stimulation with the characteristic sharp response in the first milliseconds after stimulation. Color-coded are the bursting potentials, in light blue, doublets, which correspond to two spikes that occurred within 30 ms, and in red, triplets, which correspond to three spikes in that time window. (B) A zoom-in of the previous rasterplot shows the first milliseconds of response, not only showing variability in response time but also the inter-spike interval of the bursts, which is usually smaller than 10 ms.

This difference is six times the one encountered for the single events, which denotes the weight the bursting had in the overall increase of activity. This phenomenon is even clearer when investigating the triplet events. They show an increase from an average of 0.28 ± 1.02 before the stimulus, to 11.96 ± 16.70 events during the onset response.

Although there was a considerable increase in bursting activity in these neurons, there was no distinction in the bursting activity between those that preceded and those that succeeded the excitatory neurons, nor between their spontaneous generation and those evoked after stimulus presentation in any of the groups.

### 3.1.5 Fast and late responders differ in their thalamocortical synapse density.

Up to this point, I have analyzed the electrophysiological responses of the recorded neurons. Based on the obtained results, it seems that the main difference between those inhibitory neurons that precede the excitatory neurons and those that succeed them relies on their response to the thalamocortical activation.

To evaluate this further, I quantified the number of putative synapses between the boutons of the AAV-labeled axon and the swellings of the dendrites of the inhibitory neurons. While the overlap does not mean that there is a synapse in that particular area, it sets a maximum bound of possible synaptic contacts as seen in table 1. A more detailed account of all experiments can be found in the supplements (Table S5).

Table 1: Axon-dendrite overlap in both response groups.

| Identity | Response group | Average number of swellings | Overlap (%) |
|---|---|---|---|
| Cell 1 | Fast responder | 21.25 | 29.86 |
| Cell 2 | Late responder | 32.75 | 15.56 |
| Cell 3 | Fast responder | 26.75 | 29.81 |
| Cell 4 | Late responder | 23.5 | 18.79 |
| Cell 5 | Non-responder | 21.0 | 12.66 |
| Cell 6 | Non-responder | 16.0 | 12.80 |

Interestingly, the number of putative synapses showed that those neurons that preceded the excitation had on average 29.83 ± 3.34% of their dendritic swellings overlapped with VPm axons. In the meantime, those neurons that responded after the excitatory population had a 17.17 ± 3.83% overlap between their dendritic swellings and the VPm axonal boutons. In those cases where neurons did not respond at all to stimuli, an even lower number (12.74 ± 3.25%) of overlaps was found. These evaluations were found to be significant in all cases (figure 27).

I also explored the possibility that these putative synapses were more concentrated in some areas along the dendrite. To this end, I evaluated separately the number of swellings and overlaps along the dendrite according to their distance to the soma. I divided the dendrite every 50 µm starting from the soma. There was no significant difference between either the number of swellings or the percentage of overlap in those neurons, regardless of their response group. The corresponding quantification can be seen in a supplementary table (table S6).

The difference in the overlap of those that precede and those that, either succeed the excitatory response or show no response at all, can be seen as indicative of the amount of thalamocortical input these neurons receive.

The higher number and density of axonal projections reaching these neurons, combined with their short latency to both a sensory-evoked stimulus and a direct stimulation of the thalamocortical synapses, suggests that those neurons preceding excitation receive a strong feed-forward innervation from the thalamus. By comparison, the other groups can be seen as receiving either a weak or sparse thalamic stimulation, which in our case translates to a longer latency of response and a smaller number of possible synaptic points.

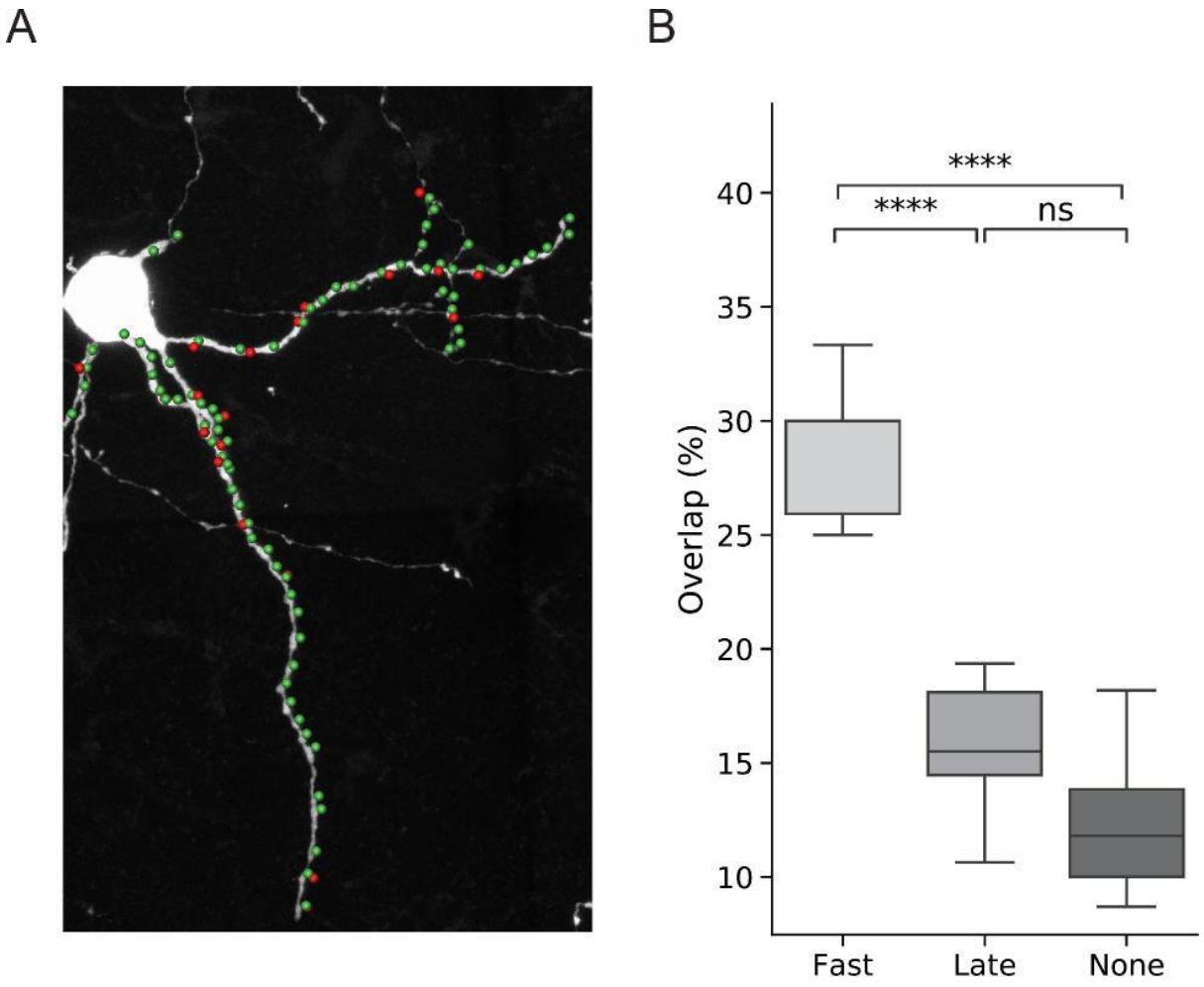


Fig 27: Comparison of putative synapse density

(A) Example image of the quantification of overlap between thalamocortical axon and inhibitory neuron's dendrite. The biocytin-filled neuron can be seen in a bright white signal and each swelling along the dendrite is labeled with a green marker. The overlap is labeled in red in the corresponding channel (AlexaFluor-647). In this example, a maximum z-projection is shown with both channels at the same time. (B) Comparison of percentage of overlap in inhibitory neurons according to their response to stimuli. Those that preceded the excitatory population show a significantly higher percentage of overlap indicating that they likely receive strong thalamocortical input from the thalamus.

### 3.1.6 Fast and late responders share similar morphologies.

Having established the two distinct populations, I explore which cellular properties could underlie these differences in response patterns. In this section, I will proceed to explain how I investigated the morphological differences of these neurons.

Having the neurons reconstructed and registered to our reference frame (Egger et al., 2012), I was able to compare between neurons from different areas of the barrel cortex. I explore all the morphological features that had been reported as key differences in the neurons involved in feedforward inhibitory circuits, such as dendrite length, axon length, and soma depth (Porter et al., 2011; Koelbl et al., 2015; Feldmeyer et al., 2017; Zhou et al., 2020). I first focus on the vertical and horizontal spans of both dendrite and axon projections from these neurons. The vertical and horizontal extensions were calculated by creating a surface area between the ending points of dendrites or axons respectively. The maximum distance between the points in the surface in the horizontal or vertical axes was measured.

The average vertical extension of the axons in the inhibitory neurons was 405.76 ± 152.15 µm (n = 21), ranging from small neurons with 230 µm in the smaller case, to 750 µm in length in the biggest neurons. Similarly, the horizontal extension had an average of 533.43 ± 190.03 µm (n = 21), ranging from 280 µm to 890 µm. Most of the inhibitory neuron's projections are restricted to their home barrel, which is something that can also be seen with the dendrite extensions, where the average vertical extension was 282.82 ± 102.93 µm (n = 23) and 320.0 ± 148.01 µm average horizontal extension.

Here, I segregated the data into those that preceded the excitatory population and those who succeeded it. I then compared the axon and dendrite extensions between those groups. The average axonal extension was 363.13 ± 164.29 µm vertical and 500.25 ± 140.78 µm horizontal for the fast responders, while for the late responders, the axonal extension was 397.63 ± 168.83 µm vertical and 498.13 ± 190.94 µm horizontal. In neither case, there was a significant difference between groups ($p = 0.98$ for the horizontal extension and $p = 0.685$ for the vertical extension comparison. Multi-sample comparison test with post hoc pairwise comparison using the Bonferroni correction).

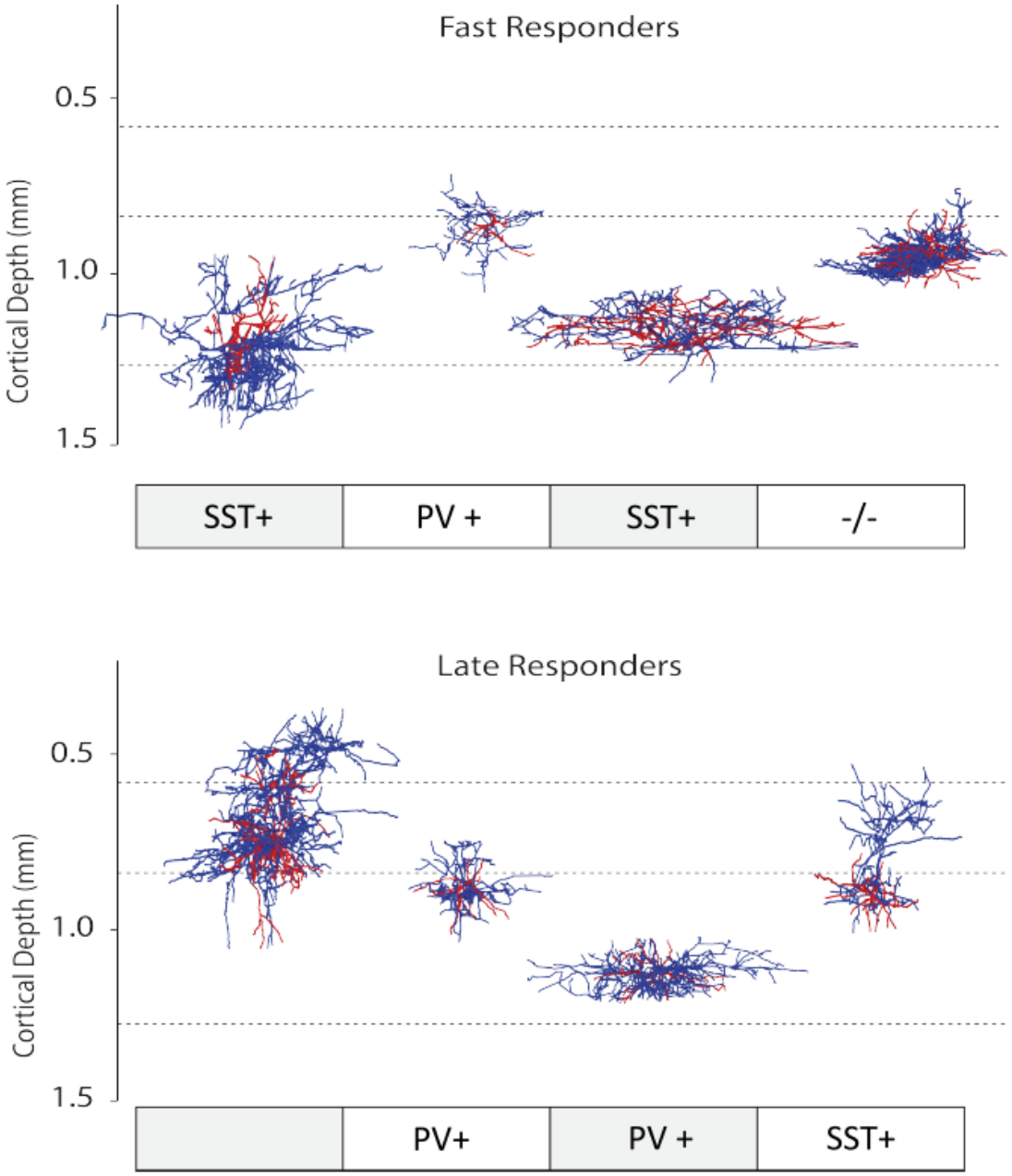


Fig 28: Example morphologies of fast and late responders

Example morphologies of (top) fast responders and (bottom) late responders. In both groups, there are examples of morphologies, whose projections are restricted to a particular layer or column, and examples of translaminar or transcolumnar morphologies, whose projections extend several layers and innervate neighboring columns.

A similar picture is seen when a comparison between the dendrite extensions is done, with an average of 249.44 ± 63.46 µm vertical and 322.77 ± 182.26 µm horizontal for the fast responders and 282.78 ± 128.92 µm vertical and 309.44 ± 121.36 µm horizontal for the late responders ($p = 0.857$ for the horizontal extension and $p = 0.496$ for vertical. Multi-sample comparison test with post hoc pairwise comparison using the Bonferroni correction). A gallery of morphologically reconstructed and registered neurons (figure 28) shows the overall shape and distribution of the neuron projections and position in the neocortex. The examples shown demonstrate that neither the depth nor shape of the neuron seems to be indicative of the differences in their latency response.

### 3.1.7 Relationship between latency responses and molecular identity

After the morphological reconstruction, I explored the relationship between inhibitory neuron responses and molecular identity. In the rat's barrel cortex, the inhibitory population can be sorted into three big families of non-overlapping molecular markers. The family of parvalbumin positive neurons, somatostatin positive neurons, and a big group of serotoninergic positive receptors (5-$HT_3$), out of which the vasointestinal peptide positive neurons are the majority (Meyer et al., 2013).

I used antibodies against parvalbumin and somatostatin to evaluate the identity of these populations. Neurons that were identified as inhibitory but were not stained by either of the aforementioned markers were considered "Double negatives" (-/-). 24 neurons were successfully labeled, the distribution can be seen in the following table (table 2)

Table 2: Molecular identity distribution in the in vivo sample of inhibitory neurons.

| Molecular Identity | Labeled neurons | Fraction |
|---|---|---|
| SST | 8 | 33.3% |
| PV | 9 | 37.5% |
| (-/-) | 7 | 29.2% |

I compared the distribution of those molecular identities in the response groups to see if there was any correlation between molecular identity and latency response. I found examples of parvalbumin positive, somatostatin positive, and double negatives distributed in both response groups. I compared the latencies across their molecular identities and found no significant difference between these populations. All comparisons of somatostatin and parvalbumin labeling (n = 15, two-sided t-test, p = 0.76), somatostatin and double negative (n = 14, two-sided t-test, p = 0.56), and parvalbumin and double negative (n = 13, two-sided t-test, p = 0.57) yielded no significant difference between the populations. I also compared if there was a correlation between those preceding the excitatory population and those succeeding it, with their molecular identity. A summary of those comparisons can be found in table 3.

Table 3: Molecular identity distribution in both response groups.

| Molecular Identity | Response group | Number of Neurons | Latency |
|---|---|---|---|
| SST | Fast Responder | 5 | 1.26 ms |
| PV | Fast Responder | 3 | 1.17 ms |
| (-/-) | Fast Responder | 4 | 1.21 ms |
| SST | Late Responder | 3 | 12.08 ms |
| PV | Late Responder | 4 | 6.71 ms |
| (-/-) | Late Responder | 2 | 7.35 ms |

The comparison shown in figure 29 using the data from table 2 shows no significant difference between the latency responses in the molecular marker's groups. It does show again a difference between those fast responders, and those late responders. Even when segregated into their molecular identities.

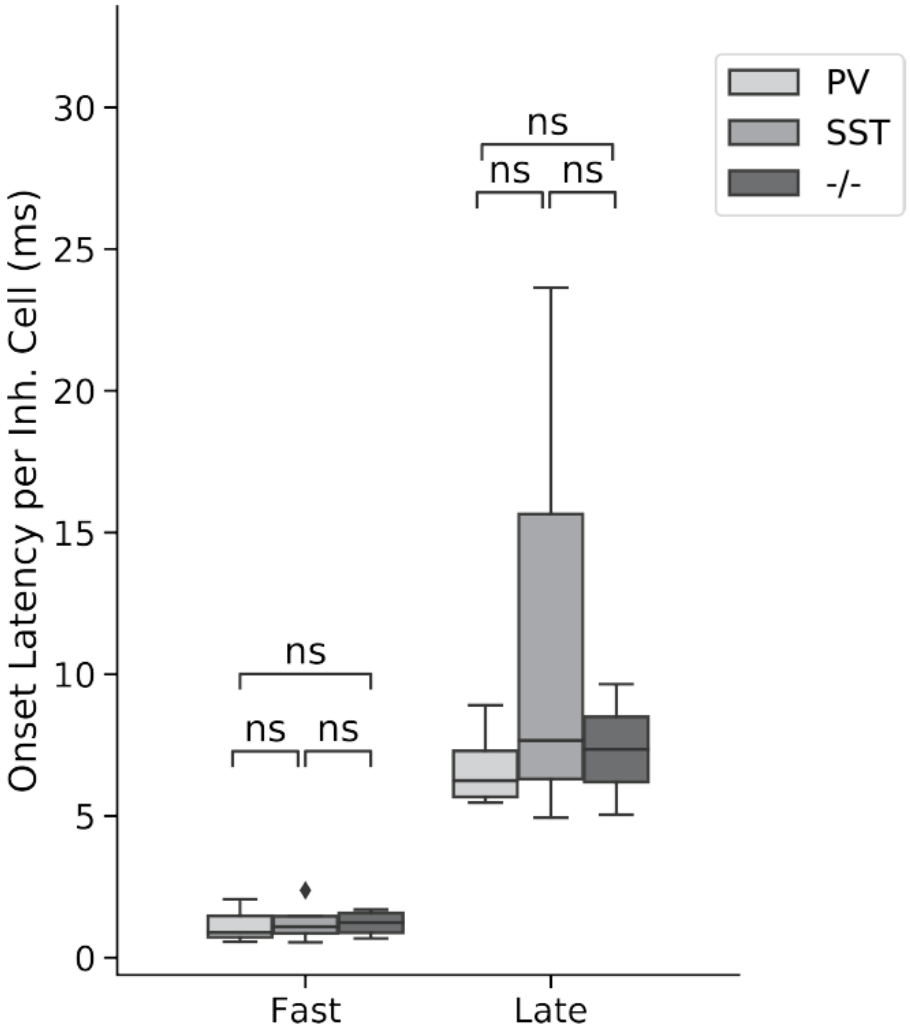


Fig 29: Molecular composition of response groups

Comparisons of median latencies between Inhibitory neurons. These groups were divided both by their molecular identity, and their latency response to the stimulus. There were no significant differences between the latency responses according to their molecular identity. Interestingly, there is a clear division between the groups that precede or succeed the excitation, even though they are themselves highly heterogeneous.

Before any conclusion from the analysis of molecular identity could be done, I had to be sure that the dataset had been unbiased sampled, to avoid over or under representation of a particular depth or identity. To this end, I quantified the labeling of inhibitory neurons from the three molecular groups, throughout the full depth of the barrel cortex.

To this end, I stained the tissue against GAD-67 and one of the major molecular markers for inhibitory neurons, either parvalbumin, somatostatin, or VIP. Once done, the region of interest, a 1 mm x 1 mm area centered in the D2 column, was obtained and the 3D volume of the whole column was acquired.

Inhibitory neurons were quantified in the region of interest by manual determination. An average of 2186.8 ± 417.0 GAD-67 positive neurons were found across the D2 column of the barrel cortex. The distribution of these neurons across layers was not homogeneous. The quantification of all the somata shows that there is an increased density in layer 4. This is consistent with what was previously described (Meyer et al., 2011, 2013) and these absolute numbers were used to explore the proportion of molecular identities of these Inhibitory interneurons.

I also analyzed the distribution across depth and localization inside the barrel structure and found there was no significant difference between the distribution of Inhibitory interneurons inside the barrel, or outside in the septa. A complete quantification of the number of labeled somata is shown in table 4.

The quantification of all the labeled somata shows that the parvalbumin positive neurons had an average of 1314.0 ± 608.0 positive neurons across the column. Out of those, 1293.0 ± 591 show double-labeling between the marker and GAD-67, which corresponds to a 98.54 ± 0.62%, a proportion comparable to what was previously reported by Meyer et al. (97.80%) (Meyer et al., 2013). This can also be seen for the other molecular markers. An average of 467.0 ± 170.0 SST positive neurons were found across the D2 column. Out of those, 458.0 ± 168.0 show double-labeling which corresponds to a 97.91 ± 0.31%, comparable to what was previously reported (97.40%). A similar case was found for the VIP positive neurons. An average of 670.0 ± 52.0 positive neurons were found across the barrel cortex, out of which 651.0 ± 66.0 show double-labeling, (97.14 ± 2.44%).

In all cases, more than 97% of all molecularly labeled neurons were positive for GAD-67. This indicates that these markers are specific for the inhibitory population, at least in these experimental conditions (Rudy et al., 2011). From these results, we can also extract that the total inhibitory population is not evenly divided between these non-overlapping groups. Parvalbumin encompasses 53.22 ± 10.94% of the total inhibitory population, while somatostatin and VIP represent 20.35 ± 1.4% and 33.05 ± 0.11% respectively.

In a similar manner to the distribution of GAD-67 neurons, the quantification of the distinct molecular identities showed not to be homogeneous across the depth of the cortex. In turn, the distribution of each molecular identity had a particular distribution profile. Quantification of the GAD-67 and molecular labeling per layer is summarized in table 4.

Table 4: Molecular marker distribution of Inhibitory neurons in vS1

| | GAD-67 Neurons | PV + neurons | SST + neurons | VIP + neurons |
|---|---|---|---|---|
| L1 | 80.20 | 20.00 | 8.50 | 17.50 |
| L2/3 | 434.67 | 228.50 | 116.00 | 100.50 |
| L4 | 414.00 | 299.00 | 25.00 | 145.00 |
| L5 | 779.20 | 592.50 | 104.00 | 245.00 |
| L6 | 477.50 | 154.50 | 203.00 | 143.00 |
| Total | 2185.50 | 1294.50 | 456.50 | 651.00 |

These profiles show that some areas of the cortex seem to prefer a particular population. For instance, The profile of PV-positive neurons shows an increase in the density of labeled somata in layers 2/3 and deep layer 5. This can reflect the substantial number of basket cells in deep layer 5, which are known for being the main family of PV-positive inhibitory neurons (Naka & Adesnik, 2016). In turn, SST-positive neurons have an initial peak in densities in layers 2/3 and then a slow but sustained increase in layers 5 and 6, likely driven by Martinotti and non-Martinotti SST-positive neurons (Nigro et al., 2018; Naka et al., 2019).

Lastly, VIP cells show the characteristic increase in Layer 1, a consequence of the concentration of neuroglial cells (Lee et al., 2015); and then a sustained increase up to layer 4. A representation of these can be seen in the following figure (figure 30).

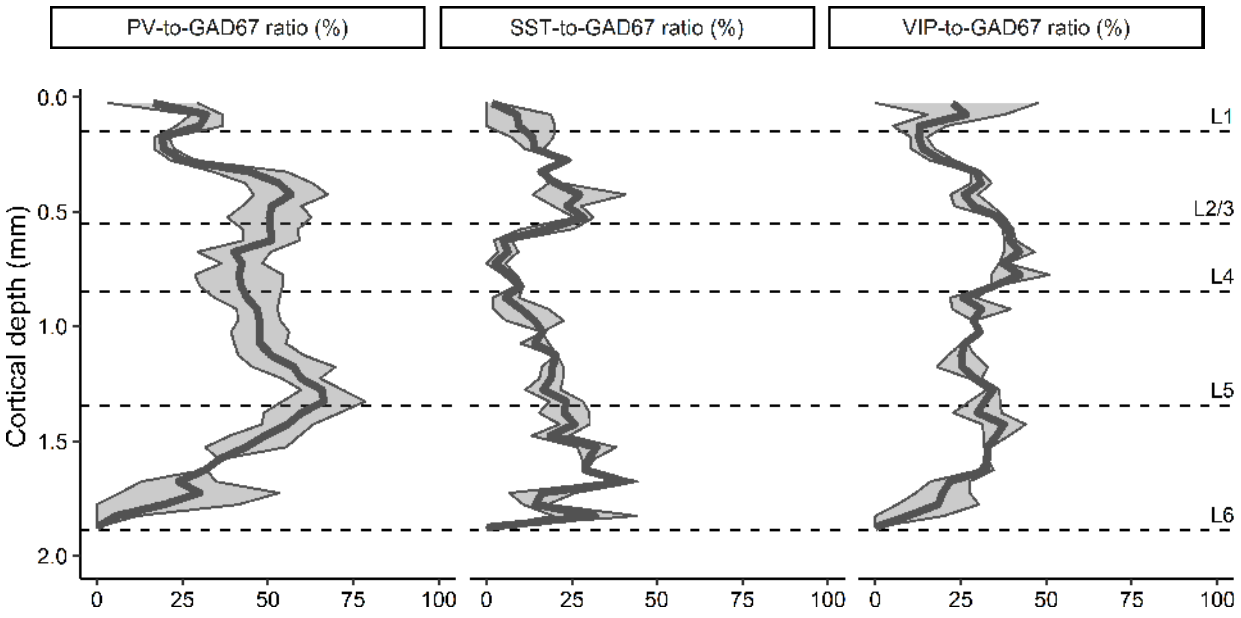


Fig 30. Depth distribution of molecular groups in the D2 column

Depth profile of all three major molecular groups of inhibitory neurons in the barrel cortex. Each panel shows the percentage of inhibitory neurons (GAD-67 positive neurons) double labeled with one of the molecular groups, either PV, SST, or VIP. Although the ratio varies throughout the depth of the cortex, PV-positive neurons consistently represent around 50% of all inhibitory interneurons.

I then compare these numbers and distributions with what was previously reported and the quantification of the molecular identities for the barrel cortex, and my sample to assess if the analyzed sample is representative of the whole population, and unbiased to a particular depth. As visualized in figure 31.

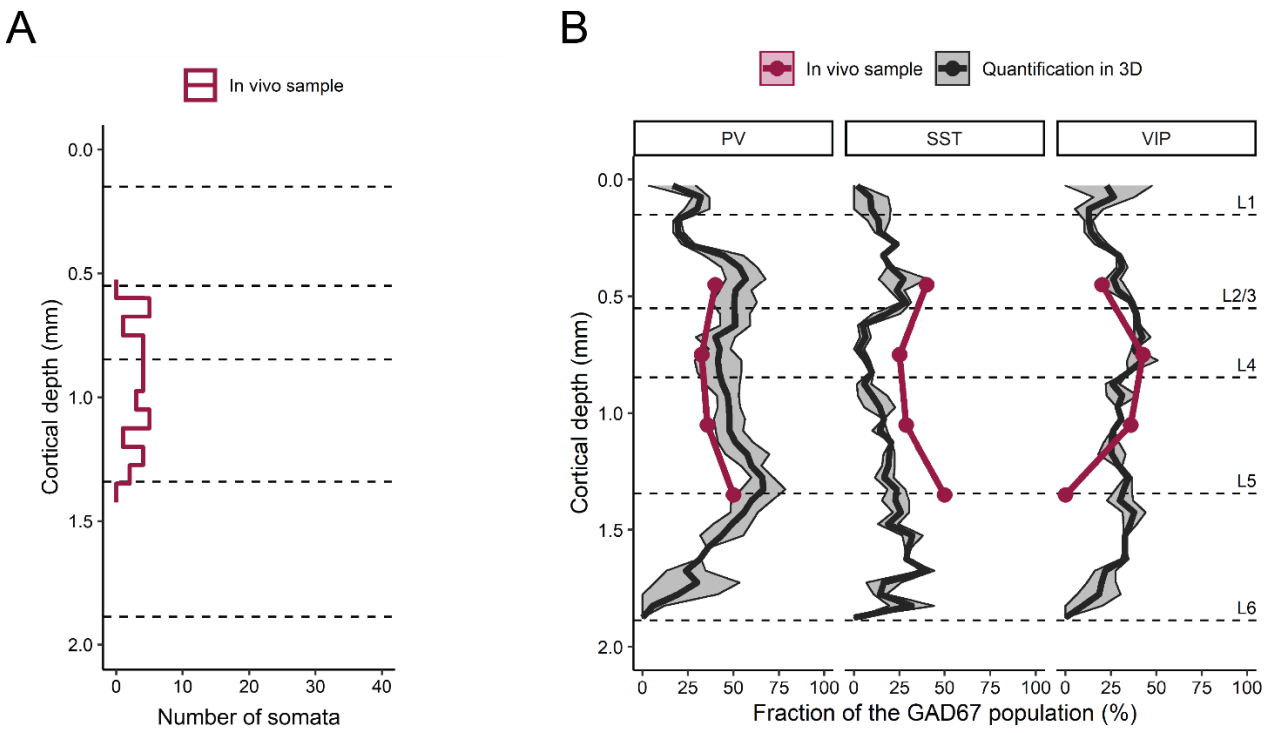


Fig 31: Representative sampling and molecular proportionality

(A) Number of somata per cortical depth. Inhibitory neurons were sampled from layers 4 and 5. The distribution of somata shows that the in vivo sampling was unbiased against a particular layer or depth. (B) Quantification of the fraction of each of the molecular markers. A representative sample would reproduce the fraction of molecular markers measured for the whole population.

These results combined, show that neither of the cellular properties that I have analyzed in this thesis, electrophysiological properties, axon-dendrite morphology nor molecular identity are sufficient to explain the differences in sensory evoked responses in this population. Only the number and density of synapses held any relationship with the latency of response seen for these neurons.

## 3.2 Quantification of direct thalamocortical input onto inhibitory neurons

So far, all the evidence I have gathered points to the importance of the density and distribution of thalamocortical synapses for the rapid activation of inhibitory neurons. Likely receiving feedforward innervation from the primary thalamus, these neurons respond with a monosynaptic latency to the VPm activation. These neurons share similar responses, regardless of their individual differences in morphology or molecular identity. Curiously, those neurons that do not respond, or do so after the activation of local excitatory neurons, are equally independent of the individual cellular properties.

To evaluate if this was the case, I explored the thalamocortical input distribution on the population of layer 4 and 5 inhibitory neurons in the barrel cortex. In order to have a clear assessment of the connections between the thalamus and the different populations of inhibitory neurons in the barrel cortex, I use trans-synaptic viral injections which label all the neurons that receive a monosynaptic innervation from the VPm.

In the barrel cortex, a NeuN staining conjugated with AlexaFluor-405 was used to establish the layer borders and determine the VPm innervation profile. The injection is combined with a reporter (eGFP) for visualization of the labeled somata. A similar profile to what was described for the cholera toxin injections, shown in figure 6, provides sufficient evidence that the injection and viral spread were successfully done. Of the 8 animals injected with this protocol, 6 showed a similar spread of VPm innervation in layers 4 and 6, together with neuronal labeling in the thalamic nucleus.

Quantification of the ratio between the eGFP-labeled neurons and the total number of neurons in the column area, provided by the NeuN staining was done to assess the efficacy of the injections and spread. First, a quantification of the distribution of these distinct populations in the layers of interest was done. As previously mentioned, the NeuN staining quantification was used to establish the layer borders (figure 32).

The NeuN staining had an average of 373 ± 50.08 neurons in layers 4 and 5 (n = 10), out of these, 182.5 ± 24.77 were located in layer 4 and 190.5 ± 30.06 in layer 5. The absolute number of neurons in L4 and L5 are relatively similar. It is known that the anatomical distinction between both layers is the increased density of somata in L4 compared to the other layers (Welker, 1976). The difference relies on the size of those layers. Layer 4 has an average size of 325 µm, while layer 5 average size is 511 µm. This means that while the absolute number of neurons is relatively similar, the density of somata in layer 4 is considerably higher, consistent with previous reports (Meyer et al., 2011, 2013).

Afterward, parvalbumin and somatostatin quantification were compared with previous studies to ensure the correct labeling of the inhibitory population. The numbers reported are comparable both in absolute numbers and in density and distribution to those previously reported (Meyer et al., 2013). A detailed quantification can be seen in table 5.

Table 5: Distribution of distinct populations in layers 4 and 5

| | Total Neurons | Layer 4 neurons | Layer 5 neurons | L4 neurons (%) | L5 neurons (%) |
|---|---|---|---|---|---|
| NeuN | 373.0 | 182.50 | 190.5 | 48.93 | 51.07 |
| SST | 37.55 | 13.00 | 24.55 | 34.62 | 65.38 |
| PV | 41.67 | 23.91 | 17.55 | 57.58 | 42.32 |

Once the distribution of somata was established, I proceeded to analyze which of those neurons had also been labeled by the viral injection, expressed by eGFP positive signal.

The number of neurons double-labeled by NeuN and eGFP was 120.3 ± 36.30 on average. Out of these, 55.8 ± 13.64 were located in layer 4, and 64.5 ± 23.90 in layer 5. In both layers, the percentage of double labeling was 30.6% and 33.6% respectively. These percentages represent the maximum possible labeling with this experimental procedure since it indicates that out of all neurons in the barrel cortex, around 30% can be labeled with this technique.

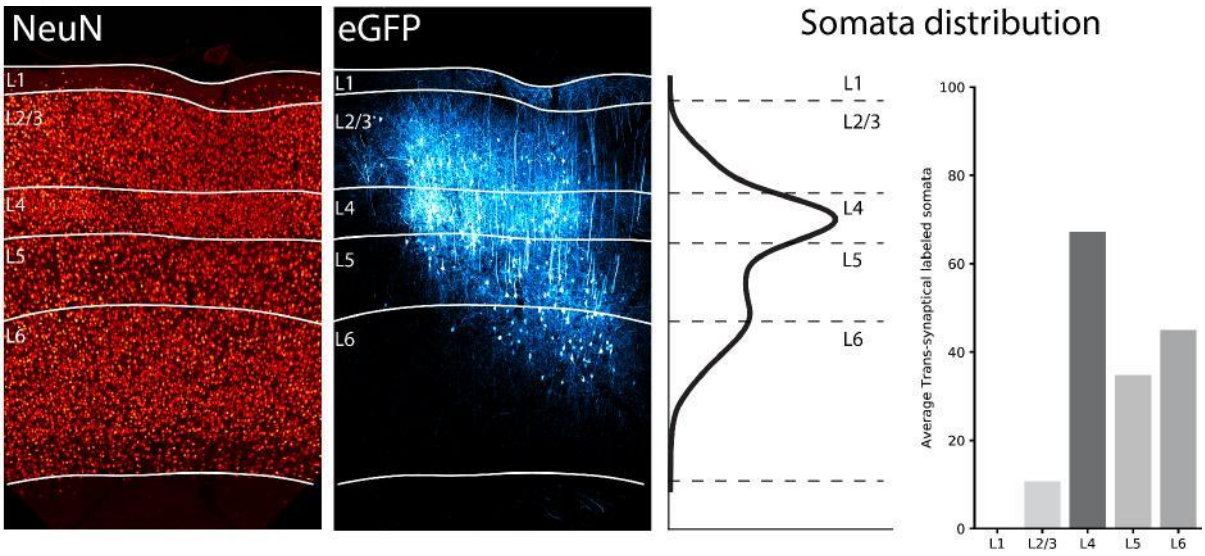


Fig 32: Distribution of synaptically connected somata in barrel cortex

Image of a section of the barrel cortex on an experiment where the trans-synaptic virus was injected into the VPm. On red, a NeuN staining done on the same section was used to set the layer borders. On cyan the trans-synaptic labeling of innervated neurons. In the consequent panels the somata distribution of labeled neurons. L1 is characterized by a low somata count. L2/3 increases the number of somata compared to L1, but a sharp increase in soma density marks the L4 border. The density of somata diminishes again in L5 until the L6 border where it increases again. A successful VPm injection of a trans-synaptic virus can be assessed by the concentration of barrel cortex labeling in layers 4 and 6.

In the same experiments, slices that were not stained against NeuN were used to evaluate either the somatostatin or parvalbumin fraction of those eGFP-positive neurons.

I repeated the same approach as for the NeuN staining, for each of the molecular markers. There was an average of 23.91 ± 3.73 neurons parvalbumin positive neurons in layer 4, and 17.55 ± 2.11 positive neurons in layer 5. At the same time, the somatostatin labeling showed an average of 13.0 ± 3.52 somatostatin positive neurons in layer 4, and 24.54 ± 4.37 positive neurons in layer 5. Both quantifications can be seen in table 5, along with the NeuN quantification.

The analysis of double-labeled somata, between each molecular marker and eGFP was done, and the complete detailed quantification is available in the supplementary section (table S7). Nevertheless, a summary of the corresponding double-labeling fraction is provided in the following table (table 6).

Table 6: Quantification of thalamic innervation in different populations.

| | L4 Neurons | L5 Neurons | eGFP neurons in L4(%) | eGFP neurons in L5(%) |
|---|---|---|---|---|
| NeuN | 182.50 | 190.5 | 30.65 | 33.56 |
| SST | 13.00 | 24.55 | 30.13 | 19.67 |
| PV | 23.91 | 17.55 | 32.90 | 22.75 |

When analyzing the distribution of double labeled neurons between eGFP and the respective molecular marker, I find that the results are similar to those found for the NeuN population in L4. The percentage of double-labeling in all cases is around 30-32%.

Surprisingly, the labeling in layer 5 was significantly different from what was found for the NeuN. In layer 5, the parvalbumin positive neurons double labeled with eGFP was 22.75 ± 4.89% (n = 12), while in the somatostatin positive neurons, the percentage was 19.67 ± 2.84% (n = 11). Both comparisons of NeuN double labeling vs parvalbumin double labeling (n = 22, two-sided t-test, p = 0.0052) and NeuN double labeling vs somatostatin double labeling (n = 21, two-sided t-test, p = 0.0003) are significantly different (figure 33).

This difference in labeling indicates that in layer 5, there is a subset of inhibitory neurons that are either not receiving monosynaptic innervation from the primary thalamus, or that it is sparse or weak enough, to show no labeling in this experimental protocol. On the other hand, there is a subpopulation that indeed receives direct monosynaptic input from the VPm. Interestingly, this property seems to be independent of the molecular identity of these neurons.

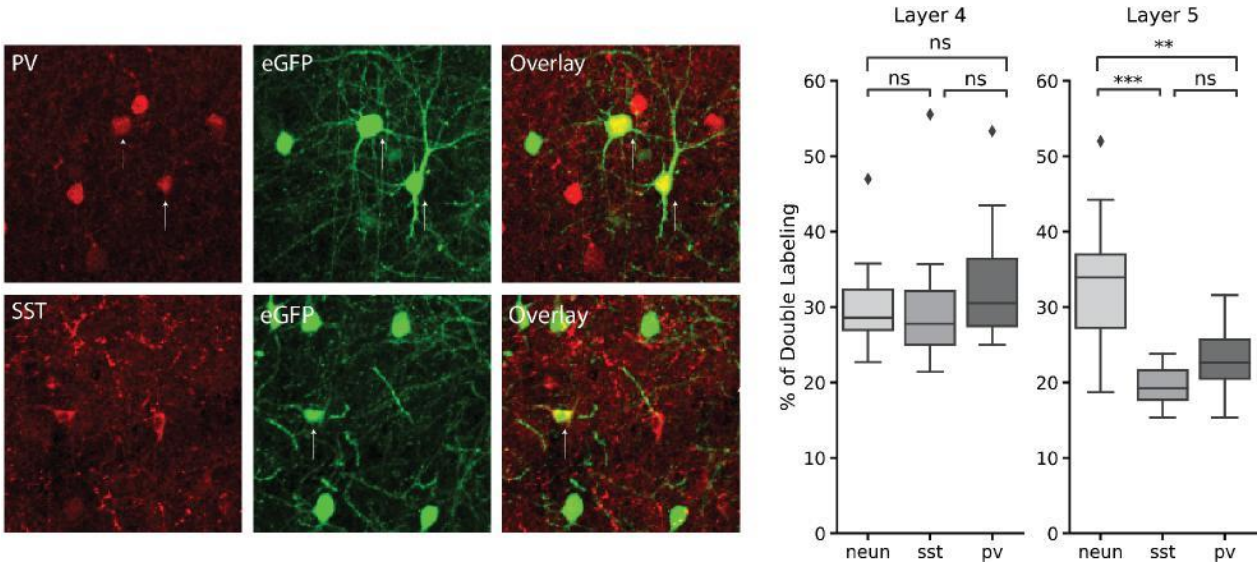


Fig 33: Laminar comparison of trans-synaptic labeling in barrel cortex

An example image of immunohistochemistry against classical molecular identities in trans-synaptic injected experiments. In red, are the selected molecular markers, parvalbumin, and somatostatin at the top and bottom respectively. In green the eGFP from synaptically connected neurons. The right panel shows the comparison between double-labeled neurons for the whole population (NeuN) and the inhibitory molecular markers. The percentages in layer 4 are not significantly different between the whole population and those somatostatin and parvalbumin inhibitory neurons. On the other hand, percentages in layer 5 for those molecular identities are significantly lower than those expected for the whole population.

# 4. Discussion

In this thesis, I systematically investigated how sensory input from primary thalamus is relayed to inhibitory neurons in the deep layers of the barrel cortex. For this purpose, I first recorded and labeled inhibitory neurons in the deep layers of the barrel cortex. Before the recording session, animals were injected with a modified rAAV conjugated with channelrhodopsin for optogenetic manipulation of thalamocortical synapses, and with mCherry as a fluorescent reporter. After an incubation period of 14 days, I recorded the spontaneous activity of these neurons, and their response to first, a multi-whisker deflection provided by a 700 ms airpuff, and second to a direct optogenetic activation of the thalamocortical synapses with an LED light.

Once all recordings were finalized, I labeled these neurons with biocytin and identified them as inhibitory neurons based on their morphological characteristics (Yen et al., 1985). These neurons were then reconstructed to evaluate their axo-dendritic arborization and registered to a standard model of the barrel cortex (Egger et al., 2012). The soma sections of these experiments were then stained against the non-overlapping molecular identities for this population, parvalbumin, somatostatin, and VIP. Afterwards, these same sections were used to quantify the number and density of putative synapses between dendrites of the inhibitory neurons, and boutons from the axons of VPm neurons (reported with m-Cherry).

Finally, I quantified the distribution and density of inhibitory neurons in the barrel cortex that receive monosynaptic input from the primary thalamus. I achieve this by the simultaneous injection of a trans-synaptic viral injection of pEEN-AAV1 in the VPm nucleus and AAV2-DIO-eGFP in the barrel cortex (Zingg et al., 2014, 2017). On top of that, I stained these sections against parvalbumin and somatostatin to evaluate the possible differences between thalamocortical input in these populations.

## 4.1 Electrophysiological responses

The analysis of the latencies after the multi-whisker deflection, shows a bimodal distribution, with an early peak at 1.02 ms after the onset of the thalamocortical evoked depolarization, measured as the first deflection of the LFP, and a secondary peak 7.21 ms after it. Interestingly, the time differences between these populations and the excitatory neurons in the same layer (4.69 ms) fall between 2-3 ms, which is the time described for a monosynaptic jump (Miles & Wong, 1986; Doyle & Andresen, 2001). These results were replicated after the optogenetic stimulation. After light stimulation, the same bimodal pattern of latency responses appeared. Again, separated with a time consistent with a monosynaptic jump.

I investigated which of these neurons would respond with short latencies to both stimuli. I found that the neurons that exhibit short latency responses and preceded the excitatory ones, did so for both types of stimuli. And similarly, for those that had a delayed response and succeeded the excitatory population.

Short latencies to both stimuli indicate that those neurons are receiving a direct, monosynaptic input from the primary thalamus and that this input is strong enough to elicit an electrophysiological response in them, therefore, these neurons can be thought as being involved in feedforward inhibition (Inoue et al., 2006; Bruno et al., 2006). This explanation is consistent with what was previously reported for inhibitory populations in L5 (Porter et al., 2001). Inhibitory neurons involved in feedforward inhibition have been described in the deep layers (Toyama et al., 1974; Buzsaki, 1984; Silberberg et al., 2008; Hu et al., 2014), as well as subpopulations of inhibitory neurons being involved in other circuit configurations (Kawaguchi et al., 1997; Ma et al., 2006; Adesnik et al., 2012). I used the latency responses to segregate the neurons into those that preceded the excitatory population and were likely involved in feedforward inhibition, and those that succeeded it.

When analyzing the rest of the electrophysiological properties, I found that these groups were equally heterogeneous in their response patterns. Both groups showed similar evoked spiking frequencies after the stimulus presentation. Neither the frequency of response, inter-spike-intervals, bursting activity nor adaptation to the stimulus were significantly different.

Previous studies have reported that neurons involved in feedforward inhibition are mostly comprised of fast spiking neurons (Lee et al., 2010; Fishell & Rudy, 2011), although some variability can be found (Woodruff et al., 2009). Similarly, it has been reported that the neurons that are not involved in FF inhibition consist mostly of non-fast spiking, adapting neurons (Fanselow et al., 2008; Xu & Callaway, 2009; Xu et al., 2013). Most of the aforementioned studies focus on the inhibitory circuits in layer 4, and that could be an explanation of why the results shown in this thesis are distinct from what is described in those studies. It is likely then, that the inhibitory circuits in the deep layers are more heterogeneous than those in layer 4.

## 4.2 Quantification of thalamocortical input

Continuing with the exploration of these two sets of inhibitory populations, I quantified the density and degree of thalamocortical input onto each of these inhibitory neurons. After labeling the recorded neuron with biocytin, I was able to measure the number and density of putative synapses. I defined those as the overlap in a 3D volume of the dendritic swellings of the inhibitory neurons and the axonal bouton from the VPm neurons (Qi et al., 2020). To assess the exact number of synaptic contacts one would need to perform a subsequent electron microscopic analysis (Markram et al., 1997a; Feldmeyer et al., 2002), but my approach allows me to determine an upper bound of possible synapses.

I found that those neurons that preceded the excitatory population showed a higher number and density of putative synapses. By comparison, the other groups receive either a weak or sparse thalamic innervation, evidenced by the significant decrease in synaptic density in those neurons that respond succeeding the excitatory ones, and even lower in those neurons that did not respond to the stimulus presentation.

This finding adds another layer of evidence to the idea that those neurons that precede the excitatory population are involved in feedforward inhibition. The combination of strong and fast response to the stimulus presentation, and the high density of putative synapses from the primary thalamus are indicative of a direct activation of these neurons by the VPm.

On the other hand, those that showed a delayed response to the stimulus had a significantly lower density of putative synapses originating from primary thalamus. This suggests that these neurons receive almost no direct input from the thalamocortical projections, or that their input is too weak or sparse to elicit an evoked response.

## 4.3 Molecular and morphological properties of inhibitory neurons

In most of the studies that focus on the inhibitory circuits in the cortex, two of the main cellular properties that differentiate the inhibitory neurons and their embedding in the local microcircuit are their morphology (Kawaguchi et al., 1997; Porter et al., 2001; Ma et al., 2006; Beierlein et al., 2003; Xu et al., 2013; Lee et al., 2020) and their molecular identity (Gonchar et al., 2008; Rudy et al., 2011; Buzsaki & Wang, 2012; Adesnik et al., 2012; Willems et al., 2018). Based on that, I analyzed these cellular properties in my inhibitory dataset and explored what was the relationship between the thalamocortical input and their morphologies and molecular identities.

I started by analyzing the morphology of the recovered inhibitory neurons. All those neurons were stained with biocytin and both axon and dendrite projections were reconstructed and identified based on their morphology (Sargent, 1989). Before any comparison could be drawn, I registered all reconstructed cells to a reference frame of the barrel cortex, standardized to the D2 column (Egger et al., 2012). Examples of those neurons can be found in figure 28. The comparison between those neurons that preceded and those that succeeded the excitatory response showed no significant differences between them.

Most neurons, regardless of their latency of response, had intralaminar and intracolumnar distributions of axons and dendrites. Moreover, when analyzing the distribution of these projections, and the overall shape of the neuron, I found that neurons with similar morphologies belong to different response groups, and neurons that differ in their shape, axon-dendrite arborizations, and soma depth, share the same responses to the stimulus presentation.

Generally, the comparison of inhibitory neuron morphologies is done in combination with the analysis of their molecular identity (Fishell & Rudy, 2011; Swanson et al., 2019; Gouwens et al., 2019; Gouwens et al., 2020). Therefore, those same neurons were stained against parvalbumin and somatostatin in order to be able to evaluate if the combination of properties could hold a relationship with their responses.

The staining against parvalbumin and somatostatin showed that there was no clear correlation between the molecular identity and their short latency response. I was able to find examples of parvalbumin positive neurons preceding and succeeding the excitatory population. The same can be said for the somatostatin positive neurons, and even those that were negative to both stainings, named “double negatives” in this project. I showed those results in figure 29, and they seem to be similar to what I described for the morphology.

Both results are surprisingly different from what is described in previous studies. Other reports, especially those focused on layer 4, tie the cellular morphology and molecular identity with their evoked response and circuit embedding (Kawaguchi et al., 1997; Gonchar et al., 2008; Rudy et al., 2011; Adesnik et al., 2012; Beierlein et al., 2003; Naka et al., 2016).

The evidence of this relationship is less clear for the deeper layers. Some reports mirror the conclusion found for layer 4, where PV positive neurons in layer 5 will be involved in feedforward inhibition (Hu et al., 2014), however, other studies find similar neurons with responses that do not fit with that kind of circuit configuration (Silberberg, 2008). A similar heterogeneity was described for somatostatin neurons (Ma et al., 2006; Xu et al., 2013). The results found in this thesis share the discrepancies found in those studies and add to the evidence of heterogeneity that the inhibitory circuits have in the deep layers.

## 4.4 Direct thalamocortical innervation of the inhibitory population

So far, I have provided evidence of the heterogeneity of the inhibitory neurons in layer 5 at the single-cell level. I have shown that neurons that respond with a sharp, early evoked activity after the stimulus presentation, receive significantly more thalamocortical input, and are likely involved in feedforward inhibitory circuits. Nevertheless, I have also shown that these neurons can have different morphologies, molecular identities, soma location, and electrophysiological responses.

I decided to confirm these findings by evaluating the direct thalamocortical input from the VPm onto the inhibitory population in layers 4 and 5 and compare them between layers and molecular identities. I used a trans-synaptic viral injection to recover the neurons in the barrel cortex, that have a monosynaptic connection with the neurons of primary thalamus (Zingg et al., 2014; 2017). Besides the stainings against parvalbumin and somatostatin, I used NeuN to first delineate the layer borders, and then to have an assessment of the efficacy of the viral procedures.

First, I evaluated the distribution of NeuN, PV, and SST neurons in layers 4 and 5. This serves as a control of the staining procedure. PV positive neurons show a slightly higher distribution in layer 4 than in layer 5. Instead, SST positive neurons are mostly clustered in the deep layers, with around 60% of them being in layer 5. Both results are consistent with previous reports (Tremblay et al., 2016), and therefore I considered it as a successful staining procedure.

When evaluating the direct thalamocortical input, I analyzed the double-staining between each molecular marker, and the viral reporter, in this case eGFP. Using NeuN as a marker for the overall population, I found that between 30-35% of those neurons showed eGFP labeling, and therefore had a monosynaptic thalamic innervation. Those percentages were the same in both layers 4 and 5, which I conclude then, as the maximum possible labeling obtained with this virus and injection protocol.

The inhibitory markers showed similar double-labeling with eGFP. Both PV and SST in layer 4 had around 30% of eGFP positive neurons, which was the same as the NeuN labeling. I can conclude there was no difference in labeling between those inhibitory groups and the general population. An interesting finding happened when analyzing the labeling in layer 5. Both PV and SST had significantly lower eGFP labeling, which indicates that there is a population of inhibitory neurons in layer 5 that does not receive direct thalamocortical input from the primary thalamus, or at least that this input is weak and sparse enough to not be labeled with this method. This finding was also not restricted to a particular population, and in fact, both molecular markers show similar decrease, which shares the same conclusion as the results I reported with the single cell analysis. It seems then that the thalamus recruits a highly heterogeneous population for feedforward inhibitory circuits, but also spares an equally heterogeneous population in the deep layers of the barrel cortex.

## 4.5 Outlook and future directions

Throughout this thesis, I have provided a unique dataset of the function, morphology, identity, and thalamic innervation of inhibitory neurons in the deep layers of the barrel cortex. I found that a subset of inhibitory neurons in these layers will have a significantly higher thalamocortical innervation than the rest, and that translates as a sharp, early, and strong response to thalamic activation.

Nevertheless, I could not find a clear relationship between the particular cellular properties of each neuron, and their response to the stimulus presentation. Moreover, I found that this heterogeneity is replicated in those neurons that did not receive a strong thalamocortical innervation and whose response succeeded the excitatory neurons in the same layers. These results are consistent with the variability previously reported for the deep layers (Kawaguchi et al., 1997; Ma et al., 2006; Silberberg, 2008; Fanselow et al., 2008; Xu et al., 2013; Hu et al., 2014). Furthermore, an assessment of the density and distribution of the inhibitory neurons directly innervated by primary thalamus, adds anatomical evidence for the existence of these two distinct inhibitory populations.

Overall, the evidence provided in this thesis provides a new insight into the inhibitory population of the deep layers of the barrel cortex. Together with the differences found in the activity, morphologies, and thalamic input of the layer 5/6 corticocortical neurons (L6CC) and the layer 4 excitatory neurons (Bast & Guest et al., 2023), show that the thalamocortical circuits in the deep layers are substantially different than those in layer 4. While I have reported the differences and a possible circuit configuration of the subpopulations of inhibitory neurons, further pair-recording experimentation of inhibitory and excitatory neurons in the local circuit would be useful to confirm or expand our hypothesis. Moreover, advancements in network analysis and the development of biologically realistic connectomes have expanded our knowledge of the circuit motifs of neurons in the cortex (Udvary et al., 2022). Because of the novelty of the data, I have provided in this thesis, a new generation of models could incorporate this data to have a better representation of the interplay of thalamocortical circuits and their effects on cortical output.

# 5 Supplementary material

Table S1: Feature selection for in vivo electrophysiological analysis

| Feature | Description |
|---|---|
| Soma depth | Cortical depth location with respect to the pia surface after registration to a reference frame |
| Spont. Frequency | Spontaneous spiking frequency taken in the Spontaneous window (90 seconds before the first stimulus) |
| Onset Frequency | Evoked response frequency taken in the onset response window (50 ms after the stimulus) |
| Sustained Frequency | Evoked response frequency taken in the sustained response window (From after 50 ms up to the end of the stimulus) |
| Latency | Time between the stimulus delivery and the occurrence of the first spike in the optogenetic stimulation |
| % Response | Percentage of trials in which there was at least one spike in the response window |
| Median ISI | Median value of the inter-spike-intervals in the response window |
| Doublet spikes | Number of doublets (spikes with less than 10 ms inter-spike interval) during the response window |
| Triplet spikes | Number of triplets (set of three spikes with less than 10 ms inter-spike-interval) during the response window |
| Adaptation | Slope value of a linear regression of the number of spikes in consecutive trials during the response window |

Table S2: Chemical reagents

| Reagent type | Designation | Source/Reference | Identifier |
|---|---|---|---|
| Inj. Analgesic | Buprenorphine | Bayer | 0052485-79-7 |
| Inh. Anesthetic | Isoflurane | Piramal | HDG9623 |
| Inj. Anesthetic | Urethane | Sigma Aldrich | 51796 |
| Chemical reagent | Sodium chloride | Sigma Aldrich | 746398 |
| Chemical reagent | Biocytin | Sigma Aldrich | 576-19-2 |
| Chemical reagent | Paraformaldehyde | Sigma Aldrich | 158127 |
| Chemical reagent | Sodium phosphate dibasic | Sigma Aldrich | 09745 |
| Chemical reagent | Sodium phosphate monobasic | Sigma Aldrich | 06621 |
| Chemical reagent | TritonX-100 | Sigma Aldrich | 9002-93-1 |
| Chemical reagent | Normal goat serum | Jackson ImmunoResearch | 005-000-121 |
| Chemical reagent | Immersion type G | Leica Microsystems | 56-81-5 |

Table S3: Neuronal tracers

| Reagent type | Designation | Source/Reference | Identifier |
|---|---|---|---|
| Anterograde Tracer | CTB - Alexa 488 | Molecular probes | AF-488-CTB |
| Anterograde tracer | CTB - Alexa 647 | Molecular probes | AF-647-CTB |
| Trans-synaptic virus | pEEN-AAV1-hSyn-Cre-WPRE-hGH | Addgene | 105553-AAV1 |
| Trans-synaptic virus | AAV2-hSyn-DIO-mCherry | Addgene | 50459-AAV2 |
| Trans-synaptic virus | AAV2-hSyn-DIO-EGFP | Addgene | 50457-AAV2 |
| Monosynaptic virus | rAAV-2/1-CAG-hChR2(H134R)-Syn-mCherry | Martin Schwarz (UniBonn) | |

Table S4: Antibodies

| Reagent type | Designation | Source/Reference | Identifier |
|---|---|---|---|
| Primary antibody | Streptavidin - Alexa 647 | Molecular Probes | S11223 |
| Primary antibody | Mouse IgG1 Anti-PV | Millipore | MABN1191 |
| Primary antibody | Mouse IgG2a Anti-GAD67 | Millipore | Mab5406 |
| Primary antibody | Rabbit IgG Anti-SST | Invitrogen | PA5-87185 |
| Primary antibody | Rabbit IgG Anti-PV | Invitrogen | PA1-933 |
| Primary antibody | Rabbit IgG Anti-VIP | Invitrogen | PA5-85616 |
| Secondary antibody | Goat IgG2a Anti-Mouse - Alexa 488 | Invitrogen | A21121 |
| Secondary antibody | Goat IgG1 Anti-Mouse - Alexa 647 | Invitrogen | A21240 |
| Secondary antibody | Goat IgG Anti-Rabbit - Alexa 405 | Invitrogen | A31556 |
| Secondary antibody | Goat IgG Anti-Rabbit - Alexa 647 | Invitrogen | A32733 |

Table S5: Axon-dendrite overlap

| Identity | Response group | Number of swellings | Number of overlaps | Overlap (%) |
|---|---|---|---|---|
| Cell1 - Dendrite 1 | Fast Responder | 20 | 7 | 35.00 |
| Cell1 - Dendrite 2 | Fast Responder | 27 | 7 | 25.93 |
| Cell1 - Dendrite 3 | Fast Responder | 16 | 5 | 31.25 |
| Cell1 - Dendrite 4 | Fast Responder | 22 | 6 | 27.27 |
| Cell2 - Dendrite 1 | Late Responder | 47 | 5 | 10.64 |
| Cell2 - Dendrite 2 | Late Responder | 16 | 3 | 18.75 |
| Cell2 - Dendrite 3 | Late Responder | 28 | 5 | 17.86 |
| Cell2 - Dendrite 4 | Late Responder | 40 | 6 | 15.00 |
| Cell3 - Dendrite 1 | Fast Responder | 30 | 9 | 30.00 |
| Cell3 - Dendrite 2 | Fast Responder | 30 | 10 | 33.33 |
| Cell3 - Dendrite 3 | Fast Responder | 27 | 7 | 25.93 |
| Cell3 - Dendrite 4 | Fast Responder | 20 | 6 | 30.00 |
| Cell4 - Dendrite 1 | Late Responder | 20 | 4 | 20.00 |
| Cell4 - Dendrite 2 | Late Responder | 32 | 5 | 15.63 |
| Cell4 - Dendrite 3 | Late Responder | 17 | 4 | 23.53 |
| Cell4 - Dendrite 4 | Late Responder | 25 | 4 | 16.00 |
| Cell5 - Dendrite 1 | Non-Responder | 22 | 4 | 18.18 |
| Cell5 - Dendrite 2 | Non-Responder | 23 | 2 | 8.70 |
| Cell5 - Dendrite 3 | Non-Responder | 18 | 2 | 11.11 |
| Cell6 - Dendrite 1 | Non-Responder | 13 | 2 | 15.38 |
| Cell6 - Dendrite 2 | Non-Responder | 16 | 2 | 12.50 |
| Cell6 - Dendrite 3 | Non-Responder | 20 | 2 | 10.00 |
| Cell6 - Dendrite 4 | Non-Responder | 15 | 2 | 13.33 |
| Average group | Fast Responder | 24.00 | 7.13 | 29.84 |
| | Late Responder | 28.139 | 4.50 | 17.17 |
| | Non-Responder | 18.14 | 2.29 | 12.74 |

Table S6: Axon-dendrite overlap distribution according to distance from soma.

| Identity | Total overlap | 0-50 µm | 50-100 µm | > 100 µm |
|---|---|---|---|---|
| Cell1 - Dendrite 1 | 7 | 5 | 2 | 0 |
| Cell1 - Dendrite 2 | 7 | 4 | 3 | 0 |
| Cell1 - Dendrite 3 | 5 | 4 | 1 | 0 |
| Cell1 - Dendrite 4 | 6 | 4 | 2 | 0 |
| Cell2 - Dendrite 1 | 5 | 0 | 0 | 5 |
| Cell2 - Dendrite 2 | 3 | 2 | 1 | 0 |
| Cell2 - Dendrite 3 | 5 | 2 | 2 | 1 |
| Cell2 - Dendrite 4 | 6 | 1 | 2 | 3 |
| Cell3 - Dendrite 1 | 9 | 3 | 3 | 3 |
| Cell3 - Dendrite 2 | 10 | 2 | 5 | 3 |
| Cell3 - Dendrite 3 | 7 | 7 | 0 | 0 |
| Cell3 - Dendrite 4 | 6 | 1 | 5 | 0 |
| Cell4 - Dendrite 1 | 4 | 0 | 3 | 1 |
| Cell4 - Dendrite 2 | 5 | 3 | 2 | 0 |
| Cell4 - Dendrite 3 | 4 | 4 | 0 | 0 |
| Cell4 - Dendrite 4 | 4 | 2 | 2 | 0 |
| Cell5 - Dendrite 1 | 4 | 1 | 3 | 0 |
| Cell5 - Dendrite 2 | 2 | 0 | 0 | 2 |
| Cell5 - Dendrite 3 | 2 | 0 | 0 | 2 |
| Cell6 - Dendrite 1 | 2 | 2 | 0 | 0 |
| Cell6 - Dendrite 2 | 2 | 1 | 1 | 0 |
| Cell6 - Dendrite 3 | 2 | 0 | 1 | 1 |
| Cell6 - Dendrite 4 | 2 | 2 | 0 | 0 |
| Average Fast Responders | 7.13 | 3.75 | 2.63 | 0.8 |
| Average Late Responders | 4.50 | 1.75 | 1.5 | 1.25 |
| Average Non-Responders | 2.29 | 0.86 | 0.71 | 0.71 |

Table S7: Complete quantification of TC input in different populations of the barrel cortex.

| | L4 Neurons | L5 Neurons | eGFP neurons in L4(%) | eGFP neurons in L4(%) |
|---|---|---|---|---|
| Exp1-Neun1 | 186 | 183 | 25.27 | 21.31 |
| Exp1-Neun2 | 185 | 177 | 22.70 | 35.02 |
| Exp2-Neun1 | 137 | 135 | 27.74 | 32.59 |
| Exp3-Neun1 | 181 | 161 | 27.07 | 25.47 |
| Exp3-Neun2 | 173 | 203 | 29.48 | 18.72 |
| Exp4-Neun1 | 166 | 208 | 49.99 | 44.23 |
| Exp5-Neun1 | 186 | 228 | 32.26 | 32.90 |
| Exp5-Neun2 | 218 | 200 | 35.78 | 52.00 |
| Exp6-Neun1 | 170 | 177 | 32.35 | 37.29 |
| Exp6-Neun2 | 223 | 233 | 26.91 | 36.05 |
| Exp1-SST1 | 14 | 26 | 28.57 | 19.23 |
| Exp2-SST1 | 14 | 16 | 21.43 | 18.75 |
| Exp2-SST2 | 13 | 24 | 23.08 | 16.67 |
| Exp3-SST1 | 8 | 31 | 25.00 | 22.58 |
| Exp3-SST2 | 18 | 26 | 27.80 | 15.38 |
| Exp4-SST1 | 14 | 25 | 35.71 | 20.00 |
| Exp4-SST2 | 16 | 21 | 25.00 | 23.81 |
| Exp5-SST1 | 9 | 29 | 55.56 | 20.69 |
| Exp5-SST2 | 16 | 21 | 25.00 | 23.81 |
| Exp6-SST1 | 7 | 22 | 28.57 | 18.18 |
| Exp6-SST2 | 14 | 29 | 35.72 | 17.24 |
| Exp1-PV1 | 26 | 18 | 38.46 | 27.78 |
| Exp1-PV2 | 30 | 37 | 53.33 | 24.32 |
| Exp2-PV1 | 15 | 9 | 26.67 | 22.22 |
| Exp2-PV2 | 24 | 14 | 25.00 | 21.43 |
| Exp3-PV1 | 33 | 17 | 30.30 | 17.65 |
| Exp3-PV2 | 34 | 26 | 35.29 | 23.08 |
| Exp4-PV1 | 35 | 13 | 28.57 | 15.38 |
| Exp4-PV2 | 24 | 14 | 25.00 | 21.43 |
| Exp5-PV1 | 14 | 8 | 35.71 | 25.00 |
| Exp5-PV2 | 23 | 13 | 43.48 | 30.77 |
| Exp6-PV1 | 18 | 23 | 27.78 | 17.39 |
| Exp6-PV2 | 13 | 19 | 30.77 | 31.58 |
| NeuN Average | 182.5 | 190.5 | 30.65 | 33.56 |
| SST+ Average | 13.0 | 24.55 | 30.12 | 19.67 |
| PV+ Average | 23.91 | 17.55 | 32.90 | 22.75 |

# 6 Abstract

Thalamus functions as the main route by which incoming sensory information reaches the cerebral cortex. Thalamic nuclei will receive input from the sensory receptors in the periphery and relay it to different areas in the cortex. (Boivie & Perl, 1975; Mountcastle, 1980; Brodal, 1981; Heimer, 1983). For this thesis, I use the vibrissal system as a model of thalamocortical input onto the cortex. In this system, the cortex will receive most of the thalamocortical (TC) projections from two thalamic nuclei, the ventral posteromedial nucleus (VPm) and the posteromedial complex (POm) (Landisman et al, 2007). A canonical pathway of information flow has been described for this system, in which thalamocortical projections will target neurons in layer 4, which in turn will synapse with neurons in layer 2/3, to finally end in pyramidal neurons in layer 5 (Gilbert et al., 1979).

Although the canonical pathway is able to explain the activation of layer 4 neurons after the thalamic activation, it has become increasingly clear that neuronal responses from layer 5 do not fit with the signal flow of the canonical pathway (Egger et al., 2020). Considering the new evidence of thalamic activation of excitatory neurons in the deep layers, an investigation of the role of thalamocortical input onto the inhibitory population in the deep layers is required, as also is the evaluation of the role of the deep layer inhibitory neurons in modulating the responses of L5PTs.

To this end, I systematically investigated how sensory input from primary thalamus is relayed to inhibitory neurons in the deep layers of the barrel cortex. I first recorded and labeled inhibitory neurons in the deep layers of the barrel cortex. Before the recording session, animals were injected with a modified rAAV conjugated with channelrhodopsin for optogenetic manipulation of thalamocortical synapses, and with m-Cherry as a fluorescent reporter. I recorded the spontaneous activity of these neurons, and their response to first, a multi-whisker deflection provided by a 700 ms airpuff, and second to a direct optogenetic activation of the thalamocortical synapses with an LED light. Once all recordings were finalized, I labeled these neurons with biocytin and identified them as inhibitory neurons based on their morphological characteristics (Yen et al., 1985).

These neurons were then reconstructed to evaluate their axo-dendritic arborization and registered to a standard model of the barrel cortex (Egger et al., 2012). The soma sections of these experiments were then stained against the non-overlapping molecular identities for this population, parvalbumin, somatostatin, and VIP (Meyer et al., 2013). Afterwards, these same sections were used to quantify the number and density of putative synapses between dendrites of the inhibitory neurons, and boutons from the axons of VPm neurons (reported with m-Cherry).

Finally, I quantified the distribution and density of inhibitory neurons in the barrel cortex that receive monosynaptic input from the primary thalamus. I achieve this by the simultaneous injection of a trans-synaptic viral injection of pEEN-AAV1 in the VPm nucleus and AAV2-DIO-eGFP in the barrel cortex (Zingg et al., 2014, 2017). On top of that, I stained these sections against parvalbumin and somatostatin to evaluate the possible differences between thalamocortical input in these populations.

I find that inhibitory neurons in the deep layers exhibit either a reliable fast evoked response that precedes the surrounding excitatory neurons or a delayed response that succeeds the excitatory activation by a time consistent with a monosynaptic jump (Miles & Wong, 1986; Doyle & Andresen, 2001). This fast-evoked response was accompanied by a significantly higher density of putative synaptic contacts between these neurons and the axons from the primary thalamus. Both these results indicate that this subpopulation of inhibitory neurons receives a direct, strong input from the thalamus and these neurons are likely involved in feedforward inhibitory circuits.

I report that the composition of these circuit configurations seems to be more heterogeneous than those described for layer 4. In support of that statement, I find that those neurons preceding the excitatory population can have distinct morphologies, molecular identities, response patterns, and cortical depth. The same heterogeneity can be found in those neurons that exhibit a delayed response to the stimulus presentation. I conclude that in the deep layers of the barrel cortex, the thalamus recruits a highly heterogeneous population for feedforward inhibitory circuits, but also spares an equally heterogeneous population.

## 7. List of figures

## 8. List of tables

## References

Arco Bast, Jason M. Guest, Rieke Fruengel, Rajeevan T. Narayanan, Christiaan P.J. deKock, Marcel Oberlaender.
bioRxiv 2021.10.21.465325; doi: https://doi.org/10.1101/2021.10.21.465325

Adesnik, H., Bruns, W., Taniguchi, H., Huang, Z. J., & Scanziani, M. (2012). A neural circuit for spatial summation in visual cortex. Nature, 490(7419), 226–231. https://doi.org/10.1038/nature11526

Aizenman, C. D., & Linden, D. J. (1999). Regulation of the Rebound Depolarization and Spontaneous Firing Patterns of Deep Nuclear Neurons in Slices of Rat Cerebellum. Journal of Neurophysiology, 82, 1697–1709.

Alonso, J. M., & Swadlow, H. A. (2005). Thalamocortical specificity and the synthesis of sensory cortical receptive fields. Journal of neurophysiology, 94(1), 26–32. https://doi.org/10.1152/jn.01281.200

Audette, N. J., Urban-Ciecko, J., Matsushita, M., & Barth, A. L. (2018). POm Thalamocortical Input Drives Layer-Specific Microcircuits in Somatosensory Cortex. Cerebral cortex (New York, N.Y.: 1991), 28(4), 1312–1328. https://doi.org/10.1093/cercor/bhx044

Beierlein, M., Gibson, J. R., & Connors, B. W. (2003). Two Dynamically Distinct Inhibitory Networks in Layer 4 of the Neocortex. Journal of Neurophysiology, 90(5), 2987–3000. doi: doi:10.1152/jn.00283.2003

Bernardo, K.L. and Woolsey, T.A. (1987), Axonal trajectories between mouse somatosensory thalamus and cortex. J. Comp. Neurol., 258: 542-564. https://doi.org/10.1002/cne.902580406

Bortone, D. S., Olsen, S. R., & Scanziani, M. (2014). Translaminar inhibitory cells recruited by layer 6 corticothalamic neurons suppress visual cortex. Neuron, 82(2), 474–485. https://doi.org/10.1016/j.neuron.2014.02.021

Boivie, J. J. G., & Perl, E. R. (1975). Neural substrates of somatic sensation. MTP International review of science, Physiology series one, 3, 303-411.

Brodal, A. 1981. Neurological Anatomy in Relation to Clinical Medicine, p. 120. Oxford Univ. Press, New York

Bruno, R. M., & Sakmann, B.(2006). Cortex is driven by weak but synchronously active thalamocortical synapses. Science, 312(5780), 1622–1627. doi: doi:10.1126/science.1124593

Buzsáki, G. (1984). Feed-forward inhibition in the hippocampal formation. Progress in neurobiology, 22(2), 131-153.

Buzsáki, G., & Wang, X. J. (2012). Mechanisms of gamma oscillations. Annual review of neuroscience, 35, 203–225. https://doi.org/10.1146/annurev-neuro-062111-150444

Chmielowska, J., Carvell, G.E. and Simons, D.J. (1989), Spatial organization of thalamocortical and corticothalamic projection systems in the rat SmI barrel cortex. J. Comp. Neurol., 285: 325-338. https://doi.org/10.1002/cne.902850304

Christine M. Constantinople Randy M. Bruno. (2013). Deep Cortical Layers Are Activated Directly by Thalamus. Science 340,1591- 4. DOI:10.1126/science.1236425

De Kock, C. P., Bruno, R. M., Spors, H., & Sakmann, B. (2007). Layer- and cell-type-specific suprathreshold stimulus representation in rat primary somatosensory cortex. The Journal of physiology, 581(Pt 1), 139–154. https://doi.org/10.1113/jphysiol.2006.124321

Dercksen, V. J., Hege, H. C., & Oberlaender, M. (2014). The filament editor: An inter-active software environment for visualization, proof-editing and analysis of 3D neuron morphology. Neuroinformatics, 12(2), 325–339. doi: doi:10.1007/s12021-013-9213-2

Deschênes, M., Timofeeva, E., Lavallée, P., & Dufresne, C. (2005). The vibrissal system as a model of thalamic operations. Progress in brain research, 149, 31–40. https://doi.org/10.1016/S0079-6123(05)49003-2

Diamond, M. E., Von Heimendahl, M., Knutsen, P. M., Kleinfeld, D., & Ahissar, E. (2008). 'Where' and 'what' in the whisker sensorimotor system. Nature Reviews Neuroscience, 9(8), 601–612. doi: doi:10.1038/nrn2411

Douglas, R. J., & Martin, K. A. (2004). Neuronal circuits of the neocortex. Annual review of neuroscience, 27, 419–451. https://doi.org/10.1146/annurev.neuro.27.070203.144152

Doyle, M. W., & Andresen, M. C. (2001). Reliability of monosynaptic sensory transmission in brain stem neurons in vitro. Journal of Neurophysiology, 85(5), 2213–2223. doi: doi:10.1152/jn.2001.85.5.2213

Egger, R., Narayanan, R. T., Guest, J. M., Bast, A., Udvary, D., Messore, L. F., ... Oberlaender, M. (2020). Cortical Output Is Gated by Horizontally Projecting Neurons in the Deep Layers. Neuron, 105(1), 122–137.e8. Retrieved from https://doi.org/10.1016/j.neuron.2019.10.011 doi: doi:10.1016/j.neuron.2019.10.011

Egger, R., Narayanan, R. T., Helmstaedter, M., de Kock, C. P., & Oberlaender, M. (2012). 3D Reconstruction and Standardization of the Rat Vibrissal Cortex for Precise Registration of Single Neuron Morphology. PLoS Computational Biology, 8(12). doi: doi:10.1371/journal.pcbi.1002837

Fanselow, E. E., Richardson, K. A., & Connors, B. W. (2008). Selective, state-dependent activation of somatostatin-expressing inhibitory interneurons in mouse neocortex. Journal of neurophysiology, 100(5), 2640–2652. https://doi.org/10.1152/jn.90691.2008

Feldmeyer, D., Lübke, J., Silver, R. A., & Sakmann, B. (2002). Synaptic connections between layer 4 spiny neurone-layer 2/3 pyramidal cell pairs in juvenile rat barrel cortex: physiology and anatomy of interlaminar signalling within a cortical column. The Journal of physiology, 538(3), 803-822.

Feldmeyer, D. (2012). Excitatory neuronal connectivity in the barrel cortex. Frontiers in Neuroanatomy, 6 (JUNE 2012), 1–22. doi: doi:10.3389/fnana.2012.00024

Feldmeyer, D., Qi, G., Emmenegger, V., & Staiger, J. F. (2018). Inhibitory interneurons and their circuit motifs in the many layers of the barrel cortex. Neuroscience, 368, 132-151.

Fino, E., & Yuste, R. (2011). Dense inhibitory connectivity in neocortex. Neuron, 69(6), 1188–1203. https://doi.org/10.1016/j.neuron.2011.02.025

Finnerty, G. T., Roberts, L. S., & Connors, B. W. (1999). Sensory experience modifies the short-term dynamics of neocortical synapses. Nature, 400(6742), 367–371. https://doi.org/10.1038/22553

Fishell, G., & Rudy, B. (2011). Mechanisms of inhibition within the telencephalon: “where the wild things are”. Annual review of neuroscience, 34, 535-567.

Fong, A. Y., Stornetta, R. L., Foley, C. M., & Potts, J. T. (2005). Immunohistochemical localization of GAD67-expressing neurons and processes in the rat brainstem: Subregional distribution in the nucleus tractus solitarius. Journal of Comparative Neurology, 493(2), 274–290. doi: doi:10.1002/cne.20758

Fox, K. K. D. (2008). Barrel cortex. Cambridge University Press.

Frangeul, L., Porrero, C., Garcia-Amado, M., Maimone, B., Maniglier, M., Clascá, F. and Jabaudon, D. (2014), Specific activation of the paralemniscal pathway during nociception. Eur J Neurosci, 39: 1455-1464. https://doi.org/10.1111/ejn.12524

Friedman, H. S., & Priebe, C. E. (1998). Estimating stimulus response latency. Journal of Neuroscience Methods, 83(2), 185–194. doi: doi:10.1016/S0165-0270(98)00075-2

Gabernet, L., Jadhav, S. P., Feldman, D. E., Carandini, M., & Scanziani, M. (2005). Somatosensory integration controlled by dynamic thalamocortical feed-forward inhibition. Neuron, 48(2), 315-327.

Gage, G. J., Kipke, D. R., & Shain, W. (2012). Whole animal perfusion fixation for rodents. Journal of visualized experiments : JoVE, (65), 3564. https://doi.org/10.3791/3564

Gilbert, C., Wiesel, T. Morphology and intracortical projections of functionally characterised neurones in the cat visual cortex. Nature 280, 120–125 (1979). https://doi.org/10.1038/280120a0

Gonchar, Y., Wang, Q., & Burkhalter, A. (2008). Multiple distinct subtypes of GABAergic neurons in mouse visual cortex identified by triple immunostaining. Frontiers in neuroanatomy, 1, 3. https://doi.org/10.3389/neuro.05.003.2007

Gouwens, N. W., Sorensen, S. A., Baftizadeh, F., Budzillo, A., Lee, B. R., Jarsky, T., Zeng, H. (2020). Integrated Morphoelectric and Transcriptomic Classification of Cortical GABAergic Cells. Cell, 183(4), 935–953.e19. doi: doi:10.1016/j.cell.2020.09.057

Gouwens, N. W., Sorensen, S. A., Berg, J., Lee, C., Jarsky, T., Ting, J., ... Koch, C. (2019). Classification of electrophysiological and morphological neuron types in the mouse visual cortex. Nature Neuroscience, 22(7), 1182–1195. doi: doi:10.1038/s41593-019-0417-0

Heimer, L. (1983). Ascending Sensory Pathways. In: The Human Brain and Spinal Cord. Springer, New York, NY. https://doi.org/10.1007/978-1-4684-0150-9_13.

Heiss, J. E., Katz, Y., Ganmor, E., & Lampl, I. (2008). Shift in the Balance between Excitation and Inhibition during Sensory Adaptation of S1 Neurons. The journal of Neuroscience, 28(49), 13320–13330. doi: doi:10.1523/JNEUROSCI.2646-08.2008

Hu, H., Gan, J., & Jonas, P. (2014). Interneurons. Fast-spiking, parvalbumin$^{+}$ GABAergic interneurons: from cellular design to microcircuit function. Science (New York, N.Y.), 345(6196), 1255263. https://doi.org/10.1126/science.1255263

Inoue, T., & Imoto, K. (2006). Feedforward inhibitory connections from multiple thalamic cells to multiple regular-spiking cells in layer 4 of the somatosensory cortex. Journal of neurophysiology, 96(4), 1746-1754.

Katz, Y., Heiss, J. E., & Lampl, I. (2006). Cross-Whisker Adaptation of Neurons in the Rat Barrel Cortex. Journal of Neuroscience, 26(51), 13363–13372. doi: doi:10.1523/JNEUROSCI.4056-06.2006

Kawaguchi, Y., & Kubota, Y. (1997). GABAergic cell subtypes and their synaptic connections in rat frontal cortex. Cerebral cortex (New York, N.Y.: 1991), 7(6), 476–486. https://doi.org/10.1093/cercor/7.6.476

Koelbl, C., Helmstaedter, M., Lübke, J., & Feldmeyer, D. (2015). A barrel-related interneuron in layer 4 of rat somatosensory cortex with a high intrabarrel connectivity. Cerebral Cortex, 25(3), 713-725.

Kudela, P., Bergey, G. K., & Franaszczuk, P. J. (2009). Calcium Involvement in Regulation of Neuronal Bursting in Disinhibited Neuronal Networks: Insights from Calcium Studies in a Spherical Cell Model. Biophysj, 97(12), 3065–3074. Retrieved from http:// dx.doi.org/10.1016/j.bpj.2009.09.027 doi: doi:10.1016/j.bpj.2009.09.027

Landisman, C. E., & Connors, B. W. (2007). VPM and POm nuclei of the rat somatosensory thalamus: Intrinsic neuronal properties and corticothalamic feedback. Cerebral Cortex, 17(12), 2853–2865. doi: doi:10.1093/cercor/bhm025

Lee, A. J., Wang, G., Jiang, X., Johnson, S. M., Hoang, E. T., Lanté, F., ... Julius Zhu, J. (2015). Canonical Organization of Layer 1 Neuron-Led Cortical Inhibitory and Disinhibitory Interneuronal Circuits. Cerebral Cortex, 25(8), 2114–2126. doi: doi:10.1093/cercor/bhu020

Lee, C., Lavoie, A., Liu, J., Chen, S. X., & Liu, B. H. (2020). Light up the brain: the application of optogenetics in cell-type specific dissection of mouse brain circuits. Frontiers in neural circuits, 14, 18.

Lee, S., Hjerling-Leffler, J., Zagha, E., Fishell, G., & Rudy, B. (2010). The largest group of superficial neocortical GABAergic interneurons expresses ionotropic serotonin receptors. Journal of Neuroscience, 30(50), 16796-16808.

Ma, Y., Hu, H., Berrebi, A. S., Mathers, P. H., & Agmon, A. (2006). Distinct subtypes of somatostatin-containing neocortical interneurons revealed in transgenic mice. The Journal of neuroscience : the official journal of the Society for Neuroscience, 26(19), 5069–5082. https://doi.org/10.1523/JNEUROSCI.0661-06.2006

Markram, H., Lübke, J., Frotscher, M., Roth, A., & Sakmann, B. (1997). Physiology and anatomy of synaptic connections between thick tufted pyramidal neurones in the developing rat neocortex. The Journal of physiology, 500(2), 409-440.

McGuire, B. A., Hornung, J. P., Gilbert, C. D., & Wiesel, T. N. (1984). Patterns of synaptic input to layer 4 of cat striate cortex. Journal of Neuroscience, 4(12), 3021-3033.

Meyer, H. S., Egger, R., Guest, J. M., Foerster, R., Reissl, S., & Oberlaender, M. (2013). Cellular organization of cortical barrel columns is whisker-specific. Proceedings of the National Academy of Sciences of the United States of America, 110(47), 19113–19118. doi: doi:10.1073/pnas.1312691110

Meyer, H. S., Schwarz, D., Wimmer, V. C., Schmitt, A. C., Kerr, J. N., Sakmann, B., & Helmstaedter, M. (2011). Inhibitory interneurons in a cortical column form hot zones of inhibition in layers 2 and 5A. Proceedings of the National Academy of Sciences of the United States of America, 108(40), 16807–16812. doi: doi:10.1073/pnas.1113648108

Miles, B. Y. R., & Wong, R. K. S. (1986). From the Department of Physiology and Biophysics, University of Texas Medical. Journal of Physiology, 397–418.

Miller, K. D., Pinto, D. J., & Simons, D. J. (2001). Processing in layer 4 of the neocortical circuit: new insights from visual and somatosensory cortex. Current opinion in neurobiology, 11(4), 488–497. https://doi.org/10.1016/s0959-4388(00)00239-7

Mountcastle, V. B. (1980). Central nervous mechanisms in sensation. Medical physiology, 14, 327-427.

Naka, A., & Adesnik, H. (2016). Inhibitory Circuits in Cortical Layer 5. Frontiers in Neural Circuits, 10(May), 1–16. Retrieved from http://journal.frontiersin.org/Article/10.3389/fncir.2016.00035/abstract doi: doi:10.3389/fncir.2016.00035

Naka, A., Veit, J., Shababo, B., Chance, R. K., Risso, D., Stafford, D., ... & Adesnik, H. (2019). Complementary networks of cortical somatostatin interneurons enforce layer specific control. Elife, 8, e43696.

Narayanan, R. T., Egger, R., Johnson, A. S., Mansvelder, H. D., Sakmann, B., De Kock, C. P., & Oberlaender, M. (2015). Beyond columnar organization: Cell type and

target layer-specific principles of horizontal axon projection patterns in rat vibrissal cortex. Cerebral Cortex, 25(11), 4450–4468. doi: doi:10.1093/cercor/bhv053

Narayanan, R. T., Mohan, H., Broersen, R., de Haan, R., Pieneman, A. W., & de Kock, C. P. (2014). Juxtasomal biocytin labeling to study the structure-function relationship of individual cortical neurons. Journal of Visualized Experiments (84), 1–9. doi: doi:10.3791/51359

Nigro, M. J., Hashikawa-Yamasaki, Y., & Rudy, B. (2018). Diversity and Connectivity of Layer 5 Somatostatin-Expressing Interneurons in the Mouse Barrel Cortex. The Journal of neuroscience : the official journal of the Society for Neuroscience, 38(7), 1622–1633. https://doi.org/10.1523/JNEUROSCI.2415-17.2017

Nishiyama, M., Matsui, T., Murakami, T., Hagihara, K. M., & Ohki, K. (2019). Cell-Type-Specific Thalamocortical Inputs Constrain Direction Map Formation in Visual Cortex. Cell Reports, 26(5), 1082–1088.e3. Retrieved from https://doi.org/10.1016/ j.celrep.2019.01.008 doi: doi:10.1016/j.celrep.2019.01.008

Oberlaender, M. (2007). Transmitted light brightfield mosaic microscopy for three-dimensional tracing of single neuron morphology. Journal of Biomedical Optics, 12(6), 064029. doi: doi:10.1117/1.2815693

Oberlaender, M., Dercksen, V. J., Egger, R., Gensel, M., Sakmann, B., & Hege, H. C. (2009). Automated three-dimensional detection and counting of neuron somata. Journal of Neuroscience Methods, 180(1), 147–160. Retrieved from http://dx.doi.org/10 .1016/j.jneumeth.2009.03.008 doi: doi:10.1016/j.jneumeth.2009.03.008

Oberlaender, M., de Kock, C. P. J., Bruno, R. M., Ramirez, A., Meyer, H. S., Dercksen, V. J., Helmstaedter, M., and Sakmann, B. (2011b). Cell type-specific three-dimensional structure of thalamocortical circuits in a column of rat vibrissal cortex. Cereb. Cortex. doi: 10.1093/cercor/bhr317.

Oberlaender, M., Ramirez, A., & Bruno, R. M. (2012). Sensory Experience Restructures Thalamocortical Axons during Adulthood. Neuron, 74(4), 648– 655. Retrieved from http://dx.doi.org/10.1016/j.neuron.2012.03.022. doi: doi:10.1016/j.neuron.2012.03.022

Okamoto, M., Baba, H., Goldstein, P. A., Higashi, H., Shimoji, K., & Yoshimura, M. (2001). Functional reorganization of sensory pathways in the rat spinal dorsal horn following peripheral nerve injury. The Journal of physiology, 532(Pt 1), 241–250. https://doi.org/10.1111/j.1469-7793.2001.0241g.x

Paxinos, George; Watson, Charles. (2007). The Rat Brain in Stereotaxic Coordinates. London: Academic Press.

Pierret, T., Lavallée, P., & Deschênes, M. (2000). Parallel streams for the relay of vibrissal information through thalamic barreloids. The Journal of neuroscience: the official journal of the Society for Neuroscience, 20(19), 7455–7462. https://doi.org/10.1523/JNEUROSCI.20-19-07455.2000

Pinault, D. (1996). A novel single-cell staining procedure performed in vivo under electro-physiological control: Morpho-functional features of juxtacellularly labeled thalamic cells and other central neurons with biocytin or Neurobiotin. Journal of Neuroscience Methods, 65(2), 113–136. doi: doi:10.1016/0165-0270(95)00144-1

Pinto, D. J., Hartings, J. A., Brumberg, J. C., & Simons, D. J. (2003). Cortical damping: Analysis of thalamocortical response transformations in rodent barrel cortex. Cerebral Cortex, 13(1), 33–44. doi: doi:10.1093/cercor/13.1.33

Popescu, I. R., Le, K. Q., Palenzuela, R., Voglewede, R., & Mostany, R. (2017). Marked bias towards spontaneous synaptic inhibition distinguishes non-adapting from adapting layer 5 pyramidal neurons in the barrel cortex. Scientific reports, 7(1), 14959. https://doi.org/10.1038/s41598-017-14971-z

Porter, J. T., Johnson, C. K., & Agmon, A. (2001). Diverse types of interneurons generate thalamus-evoked feedforward inhibition in the mouse barrel cortex. Journal of Neuroscience, 21(8), 2699-2710.

Qi, G., Yang, D., Ding, C., & Feldmeyer, D. (2020). Unveiling the synaptic function and structure using paired recordings from synaptically coupled neurons. Frontiers in synaptic neuroscience, 12, 5.

Rothermel, M., Brunert, D., Zabawa, C., Díaz-Quesada, M., & Wachowiak, M. (2013). Transgene expression in target-defined neuron populations mediated by retrograde infection with adeno-associated viral vectors. The Journal of neuroscience : the official journal of the Society for Neuroscience, 33(38), 15195–15206. https://doi.org/10.1523/JNEUROSCI.1618-13.2013

Rudy, B., Fishell, G., Lee, S., & Hjerling-Leffler, J. (2011). Three groups of interneurons account for nearly 100% of neocortical GABAergic neurons. Developmental neurobiology, 71(1), 45–61. https://doi.org/10.1002/dneu.20853

Sargent, P. B. (1989). What distinguishes axons from dendrites? Neurons know more than we do. Trends in neurosciences, 12(6), 203-205.

Senft, S. L., & Woolsey, T. A. (1991). Mouse barrel cortex viewed as Dirichlet domains. Cerebral cortex (New York, N.Y. : 1991), 1(4), 348–363. https://doi.org/10.1093/cercor/1.4.348

Sermet, B. S., Truschow, P., Feyerabend, M., Mayrhofer, J. M., Oram, T. B., Yizhar, O, Petersen, C. C. (2019). Pathway-, layer-and cell-type-specific thalamic input to mouse barrel cortex. eLife, 8, 1–28. doi: doi:10.7554/eLife.52665

Silberberg G. (2008). Polysynaptic subcircuits in the neocortex: spatial and temporal diversity. Current opinion in neurobiology, 18(3), 332–337. https://doi.org/10.1016/j.conb.2008.08.009

Simons, D. J., & Carvell, G. E. (1989). Thalamocortical response transformation in the rat vibrissa/barrel system. Journal of neurophysiology, 61(2), 311–330. https://doi.org/10.1152/jn.1989.61.2.311

Swanson, O. K., & Maffei, A. (2019). From hiring to firing: Activation of inhibitory neurons and their recruitment in behavior. Frontiers in Molecular Neuroscience, 12(July), 1–9. doi: doi:10.3389/fnmol.2019.00168

Tremblay, R., Lee, S., & Rudy, B. (2016). Properties To Circuits. Neuron, 91(2), 260–292. doi: doi:10.1016/j.neuron.2016.06.033.GABAergic

Towle, V. L., Harter, M. R., & Previc, F. H. (1980). Binocular interaction of orientation and spatial frequency channels: Evoked potentials and observer sensitivity. Perception & Psychophysics, 27(4), 351–360. https://doi.org/10.3758/BF03206124

Toyama, K., Matsunami, K., Ohno, T., & Tokashiki, S. (1974). An intracellular study of neuronal organization in the visual cortex. Experimental brain research, 21, 45-66.

Udvary, D., Harth, P., Macke, J. H., Hege, H. C., de Kock, C. P., Sakmann, B., & Oberlaender, M. (2022). The impact of neuron morphology on cortical network architecture. Cell Reports, 39(2), 110677. doi: doi:10.1016/j.celrep.2022.110677

Viaene, A. N., Petrof, I., & Sherman, S. M. (2011). Properties of the thalamic projection from the posterior medial nucleus to primary and secondary somatosensory cortices in the mouse. Proceedings of the National Academy of Sciences of the United States of America, 108(44), 18156–18161. https://doi.org/10.1073/pnas.1114828108

Vijayan, S., Hale, G. J., Moore, C. I., Brown, E. N., & Wilson, M. (2010). Activity in the barrel cortex during active behavior and sleep. Journal of Neurophysiology, 103(4), 2074–2084. doi: doi:10.1152/jn.00474.2009

Wehr, M., & Zador, A. M. (2003). Balanced inhibition underlies tuning and sharpens spike timing in auditory cortex. Nature, 426(6965), 442–446. https://doi.org/10.1038/nature02116

Welker, C. (1976). Receptive fields of barrels in the somatosensory neocortex of the rat. Journal of Comparative Neurology, 166(2), 173-189.

Wilent, W., Contreras, D. Dynamics of excitation and inhibition underlying stimulus selectivity in rat somatosensory cortex. Nat Neurosci 8, 1364–1370 (2005). https://doi.org/10.1038/nn1545

Willems, J. G. P., Wadman, W. J., & Cappaert, N. L. M. (2018). Parvalbumin interneuron mediated feedforward inhibition controls signal output in the deep layers of the perirhinal-entorhinal cortex. Hippocampus, 28(4), 281–296. https://doi.org/10.1002/hipo.22830

Willems, J. G. P., Wadman, W. J., & Cappaert, N. L. M. (2019). Interaction of Cortical and Amygdalar Synaptic Input Modulates the Window of Opportunity for Information Processing in the Rhinal Cortices. eNeuro, 6(4), ENEURO.0020-19.2019. https://doi.org/10.1523/ENEURO.0020-19.2019

Willis, W. D. Jr.[a,*]; Zhang, X.[b]; Honda, C. N.[b]; Giesler, G. J. Jr.[b]. Projections from the marginal zone and deep dorsal horn to the ventrobasal nuclei of the primate thalamus. Pain 92(1):p 267-276, May 2001. | DOI: 10.1016/S0304-3959(01)00268-8

Wimmer, V. C., Bruno, R. M., De Kock, C. P., Kuner, T., & Sakmann, B. (2010). Dimensions of a projection column and architecture of VPM and POm axons in rat vibrissal cortex. Cerebral Cortex, 20(10), 2265–2276. doi: doi:10.1093/cercor/bhq068

Woodruff, A., Xu, Q., Anderson, S. A., & Yuste, R. (2009). Depolarizing effect of neocortical chandelier neurons. Frontiers in neural circuits, 3, 922.

Xu, X., & Callaway, E. M. (2009). Laminar specificity of functional input to distinct types of inhibitory cortical neurons. Journal of Neuroscience, 29(1), 70-85.

Xu, X., Roby, K. D., & Callaway, E. M. (2010). Immunochemical characterization of inhibitory mouse cortical neurons: Three chemically distinct classes of inhibitory cells. Journal of Comparative Neurology, 518(3), 389–404. doi: doi:10.1002/cne.22229

Xu, H., Jeong, H. Y., Tremblay, R., & Rudy, B. (2013). Neocortical somatostatin-expressing GABAergic interneurons disinhibit the thalamorecipient layer 4. Neuron, 77(1), 155–167. https://doi.org/10.1016/j.neuron.2012.11.004

Yen, C. T., Conley, M., Hendry, S. H., & Jones, E. G. (1985). The morphology of physiologically identified GABAergic neurons in the somatic sensory part of the thalamic reticular nucleus in the cat. Journal of Neuroscience, 5(8), 2254-2268.

Zhou, X., Mansori, I., Fischer, T., Witte, M., & Staiger, J. F. (2020). Characterizing the morphology of somatostatin-expressing interneurons and their synaptic innervation pattern in the barrel cortex of the GFP-expressing inhibitory neurons mouse. Journal of Comparative Neurology, 528(2), 244-260.

Zingg, B., Chou, X.-l., Zhang, Z.-g., Mesik, L., Liang, F., Tao, H. W., ... Angeles, L. (2017). HHS Public Access. Neuron, 93(1), 33–47. doi: doi:10.1016/j.neuron.2016.11.045.AAV-mediated

Zingg, B., Hintiryan, H., Gou, L., Song, M. Y., Bay, M., Bienkowski, M. S., ... Dong, H.-w. (2014). Resource Neural Networks of the Mouse Neocortex. Cell, 156(5), 1096–1111. Retrieved from http://dx.doi.org/10.1016/j.cell.2014.02.023 doi: doi:10.1016/j.cell.2014.02.023

## Acknowledgments

I would first like to thank my supervisor, Dr. Marcel Oberlaender, for his guidance and support throughout these years and for giving me the opportunity to pursue my doctoral studies in his group.

I would like to thank my advisory committee, Prof. Dr. Heinz Beck, Dr. Martin Schwarz, and Dr. Stefan Remy for their helpful comments and counsel.

I would also like to thank all my collaborators (In alphabetical order), Arco Bast, Dr. Robert Egger, Prof. Dirk Feldmeyer, Dr. Jason Guest, Dr. Guanxiao Qi, Dr. Daniel Udvary for their outstanding work; I would also like to extend my gratitude to all former and current members from Marcel Oberlaender's group; and special thanks to Dr. Rajeevan Narayanan, Felipe Yañez, Fiorella Gomez, Aman Maharjan, Andres Flores, and Ezgi Bulca for their friendship and companionship, it was a pleasure working with you over these years.

I would like to extend my most profound gratitude to my family back in Argentina, in particular to my mother and my sister, whose support and affection overcame any distance.

And finally, I would like to thank my beloved family here. To my wife Sandra and my dog Tomillo. Thank you for providing me with unwavering love, support, and continuous encouragement. You have made my life better than I could ever imagine, this accomplishment wouldn't be possible without you by my side.